

2

TECHNICAL REPORT BRL-TR-3138

BRL

DTIC FILE COPY

AD-A226 435

**MODELING OF COMPACTION WAVE BEHAVIOR
IN CONFINED GRANULAR ENERGETIC MATERIAL**

DOUGLAS E. KOOKER

AUGUST 1990

**DTIC
ELECTE
SEP 11 1990
S E D**

APPROVED FOR PUBLIC RELEASE; DISTRIBUTION UNLIMITED.

U.S. ARMY LABORATORY COMMAND

**BALLISTIC RESEARCH LABORATORY
ABERDEEN PROVING GROUND, MARYLAND**

90 09 10 211

NOTICES

Destroy this report when it is no longer needed. DO NOT return it to the originator.

Additional copies of this report may be obtained from the National Technical Information Service, U.S. Department of Commerce, 5285 Port Royal Road, Springfield, VA 22161.

The findings of this report are not to be construed as an official Department of the Army position, unless so designated by other authorized documents.

The use of trade names or manufacturers' names in this report does not constitute indorsement of any commercial product.

UNCLASSIFIED

DD-A226 435

REPORT DOCUMENTATION PAGE			Form Approved OMB No. 0704-0188
<small>Public reporting burden for this collection of information is estimated to average 1 hour per response, including the time for reviewing instructions, searching existing data sources, gathering and maintaining the data needed, and completing and reviewing the collection of information. Send comments regarding this burden estimate or any other aspect of this collection of information, including suggestions for reducing this burden, to Washington Headquarters Services, Directorate for Information Operations and Reports, 1215 Jefferson Davis Highway, Suite 1204, Arlington, VA 22202-4302, and to the Office of Management and Budget, Paperwork Reduction Project (0704-0188), Washington, DC 20503.</small>			
1. AGENCY USE ONLY (Leave blank)	2. REPORT DATE August 1990	3. REPORT TYPE AND DATES COVERED Final Report / Sept 84 - Jan 90	
4. TITLE AND SUBTITLE MODELING OF COMPACTION WAVE BEHAVIOR IN CONFINED GRANULAR ENERGETIC MATERIAL		5. FUNDING NUMBERS 1L162618A1FL	
6. AUTHOR(S) Douglas E. Kooker			
7. PERFORMING ORGANIZATION NAME(S) AND ADDRESS(ES) US Army Ballistic Research Laboratory ATTN: SLCBR-DD-T Aberdeen Proving Ground, MD 21005-5066		8. PERFORMING ORGANIZATION REPORT NUMBER BRL-TR-3138	
9. SPONSORING / MONITORING AGENCY NAME(S) AND ADDRESS(ES) Naval Surface Warfare Center White Oak Laboratory 10901 New Hampshire Avenue Silver Spring, MD 20903-5000		10. SPONSORING / MONITORING AGENCY REPORT NUMBER R-10F	
11. SUPPLEMENTARY NOTES			
12a. DISTRIBUTION / AVAILABILITY STATEMENT Approved for Public Release; Distribution Unlimited		12b. DISTRIBUTION CODE	
13. ABSTRACT (Maximum 200 words) The successful transition to detonation in confined granular energetic material requires formation and maintenance of a strong compressive wave system which ignites unburned material in its path. The present investigation is directed toward an interpretation of this wave, before a full detonation wave has been established. For several years, the Naval Surface Warfare Center / White Oak has been investigating the effects of impact on confined quiescent granular material with an apparatus known as the piston-driven-compaction (PDC) experiment. This report summarizes four modeling efforts developed by the author to understand the behavior of impact-generated compaction waves as observed by NSWC in the PDC experiment. Each of the four models attempts to address some aspect of the PDC experiment, often within the simplest possible framework. These include (a) inert compaction waves governed by rate-dependent porosity adjustments, (b) quasi-steady compaction waves which account for wave-induced reaction and assume instantaneous adjustment to the equilibrium stress state, (c) collision of reactive compaction/shock waves, and (d) a transient reactive shock wave model which accounts for wave-induced reaction, gas-phase combustion of a reactive intermediate species, and transient combustion of the granular solid.			
14. SUBJECT TERMS Granular Propellants/Explosives, Impact, Compaction Waves Modeling, Combustion, Deflagration, Transition-to-Detonation		15. NUMBER OF PAGES 100	
		16. PRICE CODE	
17. SECURITY CLASSIFICATION OF REPORT Unclassified	18. SECURITY CLASSIFICATION OF THIS PAGE Unclassified	19. SECURITY CLASSIFICATION OF ABSTRACT Unclassified	20. LIMITATION OF ABSTRACT UL

UNCLASSIFIED

INTENTIONALLY LEFT BLANK.

TABLE OF CONTENTS

	<u>Page</u>
LIST OF FIGURES.....	v
LIST OF TABLES.....	xi
ACKNOWLEDGEMENTS.....	xiii
I. INTRODUCTION AND BACKGROUND.....	1
II. DESCRIPTION OF THE GRANULAR AGGREGATE.....	4
A. Implications of Constitutive Assumptions.....	4
B. Compressibility of the TMD Solid.....	5
C. Equilibrium Stress State of the Mixture.....	7
D. Rate-Dependent Porosity Change.....	12
E. Gas-Phase Equation of State.....	12
F. Phase Interaction Effects.....	12
III. COMPACTION WAVE MODEL WITH FINITE-RATE POROSITY CHANGE [33].....	14
IV. EQUILIBRIUM SHOCK WAVE THEORY [34].....	17
A. #20 Sieve Cut from Class D HMX.....	20
B. WC-231 Propellant.....	20
C. TS-3659 Ball Propellant.....	24
V. COLLISION OF REACTIVE COMPACTION/SHOCK WAVES [35].....	24
A. Model Development.....	25
B. Results.....	29
PDC-80 / 60.2% TMD TS-3659 Ball Propellant.....	29
PDC-73 / 49.4% TMD WC-231 Propellant.....	31
PDC-27 / 73% TMD Class D HMX.....	32
DDT Shot A266 / 59.8% TMD TS-3659.....	38

TABLE OF CONTENTS (continued)

	<u>Page</u>
VI. TRANSIENT REACTIVE SHOCK WAVE MODEL [36].....	41
A. Influence of Projectile Path / PDC Experiment.....	47
B. Simulation of PDC-M34 / 65% TMD Melamine (Inert Material).....	54
C. Influence of Energy Release / PDC Experiment.....	62
VII. SUMMARY COMMENTS AND CONCLUSIONS.....	71
REFERENCES.....	75
LIST OF SYMBOLS.....	81
DISTRIBUTION LIST.....	85

Accession For	
NTIS CRA&I	<input checked="" type="checkbox"/>
DTIC TAB	<input type="checkbox"/>
Unannounced	<input type="checkbox"/>
Justification	
By	
Distribution/	
Availability Codes	
Dist	Avail and/or Special
A-1	



LIST OF FIGURES

Figure	Page
1 Schematic of the NSWC piston-driven-compaction (PDC) experiment [12-15] and present modeling problem.....	3
2 Pressure vs. density for an isothermal compression of HMX at theoretical maximum density (TMD). Data for β -HMX are from Olinger et. al. [41]. Solid line (P_s) from Eq. (2). Dashed line (P_{bn}) is from theory of Baer & Nunziato [19].....	6
3 Ratio of σ_r/σ_s for double-base ball propellant TS-3659 initially at 60% TMD. Solid line is function $\xi(\epsilon_s)$. Experimental data are values of σ_{mr}/σ_{mx} from Run #8 in Ref. 42.....	8
4 Axial component of mixture stress as a function of mixture density for an isothermal compression of 60% TMD TS-3659 propellant. Solid line represents σ_{mx} from Eq. (3), dashed line is P_m , and chain-dot line is TMD from Eq. (2). Data from Run #8 in Sandusky et. al. [42]	10
5 Radial component of mixture stress as a function of mixture density for an isothermal compression of 60% TMD TS-3659 propellant. Solid line represents σ_{mr} from Eq. (3), dashed line is P_m , and chain-dot line is TMD from Eq. (2). Data from Run #8 in Sandusky et. al. [42]	11
6 Constant-velocity piston impact at 100 m/s on 73% TMD Class D HMX. Plot shows distribution of mixture pressure versus distance at a time of 20.5 μ s after impact. Compaction viscosity is 1000 poise. Numerical solution obtained with the method-of-characteristics.....	15
7 Schematic of computational problem used to simulate the NSWC piston-driven-compaction experiment [12-15]. Compaction wave in two-phase mixture is reactive equilibrium shock wave.....	19
8 Predicted compaction wave speed versus interface speed for 60% TMD #20 sieve cut HMX. Solid line represents inert compaction wave. PDC data from Sandusky [13].....	21
9 Predicted compaction/shock wave speed versus interface speed (particle velocity) for 50% TMD WC-231 propellant. Solid line is inert compaction wave, dashed and chain-dot lines involve wave-induced reaction. Data from PDC and CGC experiments [13,14]. Noted on figure are Sandusky's comments for PDC-12 and PDC-60 concerning the nature of the reaction and the interval of time before appearance of visible flame.....	22
10 Predicted compaction wave speed vs interface speed (particle velocity) for 60% TMD TS-3659 ball propellant. Data from the NSWC PDC experiment [15]. Solid line is inert compaction wave, dashed and chain-dot lines involve wave-induced reaction.....	23

LIST OF FIGURES (continued)

Figure		Page
11	Distance-time plot of constant-velocity-piston impact on a quiescent inert rate-independent medium. Note analogy with steady two-dimensional supersonic flow over a wedge.....	26
12	Distance-time plot of double impact of piston (two abrupt changes to constant velocity) on a quiescent inert rate-independent medium. Note analogy with steady supersonic flow over a double wedge.....	27
13	Possible distance-time plot of double piston impact on quiescent rate-independent <u>reactive</u> medium.....	28
14	Distance-time data for PDC-80; 160 m/s impact on 60.2% TMD TS-3659 propellant. Data from Ref. 15. Tabular values are model predictions downstream of indicated wave.....	30
15	Distance-time data for PDC-73; 220 m/s impact on 49.4% TMD WC-231 propellant. Data from Ref. 15. Tabular values are model predictions downstream of indicated wave.....	32
16	Distance-time data for PDC-27; 267 m/s impact on 73% TMD Class D HMX. Data from Ref. 14. Tabular values are model predictions downstream of indicated wave.....	34
17	Simulated radiograph triggered at 35 μ s in PDC-27. Numerical values from model predictions listed in Figure 16.....	35
18	Simulated radiograph triggered at 35 μ s in ALTERED PDC-27. Numerical values from model predictions listed in Figure 16.....	36
19	Data from LANL combustion-driven-piston experiment with 64% TMD Class A HMX. Figures courtesy of McAfee et. al. [10,11]:	
	(a) Distance-time data / Run B-9153.....	37
	(b) Radiograph #2 / Run B-9153.....	37
20	Relative distance-time data from Bernecker's [8] DDT Shot A266 using 59.8% TMD TS-3659 ball propellant (circles = probe response, squares = transducer excursion; velocity in mm/ μ s).....	39
21	Schematic of combustion process in model.....	42
22	Schematic representation of method-of-characteristics solution procedure.....	46

LIST OF FIGURES (continued)

Figure	Page
23 Comparison of model predictions and NSW data [15] from PDC-81: 237 m/s impact of Lexan projectile on 60.1% TMD TS-3659 ball propellant. Model computation assumes projectile interface speed = 192 m/s (constant), and no gas-phase reaction or propellant ignition.	
(a) Compaction wave locus and projectile locus for PDC-81. Computation assumes projectile locus follows from constant velocity.....	48
(b) Wall-mounted pressure transducer records from PDC-81.....	49
24 Comparison of model predictions and NSW data [15] from PDC-81: 237 m/s impact of Lexan projectile on 60.1% TMD TS-3659 ball propellant. Model computation based on "dual-linear" projectile path; projectile interface speed = 192 m/s up to 40 μ s, then = 173 m/s. Computation assumes no gas-phase reaction or propellant ignition.	
(a) Compaction wave locus and projectile locus for PDC-81. Computation assumes "dual-linear" projectile path; numbers represent velocity in mm/ μ s.....	50
(b) Wall-mounted pressure transducer records from PDC-81.....	51
25 Comparison of model predictions and NSW data [15] from PDC-81: 237 m/s impact of Lexan projectile on 60.1% TMD TS-3659 ball propellant. Model computation based on "quadratic" projectile path; projectile interface speed is a quadratic function of time. Computation assumes no gas-phase reaction or propellant ignition.	
(a) Compaction wave locus and projectile locus for PDC-81. Computation assumes "quadratic" projectile path; numbers represent velocity in mm/ μ s.....	52
(b) Wall-mounted pressure transducer records from PDC-81.....	53
26 Schematic of NSW piston-driven-compaction shot PDC-M34 [53].....	55
27 Quasi-static stress state for isothermal compaction of melamine initially at 65% TMD. Data from Elban et. al. [52]. Solid line represents approximation for axial component of mixture stress, σ_{mx} ; dashed line represents mixture pressure, P_m ; chain-dot line represents TMD.	
(a) "Regular" melamine (defined by $\tau_1=1.0$ kpsi, $p_1=0.$, $B_2=4.0$, $p_2=.7$ in Eq. 9).....	56
(b) "Soft" melamine (defined by $\tau_1=1.0$ kpsi, $p_1=0.$, $B_2=1.75$, $p_2=.7$ in Eq. 9).....	57

LIST OF FIGURES (continued)

Figure		Page
28	Using analysis of Ref. 34, predicted compaction wave speed vs. interface speed (particle velocity) for melamine initially at 65% TMD. PDC data (41A and 41B) from Sandusky and Liddiard [13]; dashed line is prediction based on "regular" melamine. PDC data (M34) from Sandusky and Glancy [53]; solid line is prediction based on "soft" melamine.....	58
29	Using analysis of Ref. 34, predicted compaction wave speed vs. interface speed (particle velocity) for melamine initially at 85% TMD. PDC data (74) from Sandusky and Glancy [53]; solid line is prediction based on "soft" melamine.....	59
30	Comparison of model predictions with NSW data [53] from PDC-M34: 206 m/s impact of aluminum projectile on 65% TMD melamine. Simulation ignores wall friction and assumes melamine is inert.	
(a)	Comparison of NSW data [53] for compaction wave locus and projectile face locus with model predictions. NSW projectile locus is used as boundary condition. Solid line is predicted compaction wave locus based on "soft" melamine; dotted line is based on "regular" melamine.....	60
(b)	Comparison of NSW data [53] from wall-mounted pressure transducers with model simulation based on "soft" melamine initially at 65% TMD.....	61
31	Comparison of model predictions and NSW data [15] from PDC-80: 160 m/s impact of Lexan projectile on 60.2% TMD TS-3659 ball propellant.	
(a)	Comparison of model predictions and NSW data [42] from wall-mounted pressure transducers in PDC-80 (gage #1 is located at 38.1 mm, and gage #2 is at 76.2mm). Model computation assumes wave-induced reaction releases 404 cal/g creating initial gas temperature of 1450 K; no further gas-phase reaction. Solid propellant does not ignite.....	64
(b)	Comparison of assumed paths and NSW data for projectile interface locus from PDC-80. Dashed line results from constant speed = 127 m/s. Solid line is curve-fit to experimental data.....	65
32	Comparison of model predictions and NSW data [42] from wall-mounted pressure transducer at 38.1 mm (gage #1) for PDC-80: 160 m/s impact of Lexan projectile on 60.2% TMD TS-3659 ball propellant.	

LIST OF FIGURES (continued)

Figure	Page
32(a) Model computation assumes effective transition pressure, $P_{tr} = 0$. Solid curve based on combustion of exposed surface area of grains in deformed aggregate. Chain-dash curve based on combustion of full surface area of grains.....	66
(b) Model computation assumes transition pressure, $P_{tr} = 70$ MPa. Solid curve based on combustion of full surface area of grains in deformed aggregate, when $P_g > P_{tr}$. Dashed curve based on combustion of exposed surface area of grains, when $P_g > P_{tr}$	67
33 Influence of transition pressure. Comparison of model predictions and NSWC data [42] from wall-mounted pressure transducer at 38.1 mm (gage #1) for PDC-80: 160 m/s impact of Lexan projectile on 60.2% TMD TS-3659 ball propellant. Model computations assume transition pressure, P_{tr} , is 10 MPa (dashed curved), 70 MPa (solid curve), and 300 MPa (chain-dash curve).....	68
34 Comparison of model predictions and NSWC data [42] from wall-mounted pressure transducers from PDC-81: 237 m/s impact of Lexan projectile on 60.1% TMD TS-3659 ball propellant. Model computations based on "dual-linear" (192m/s, and 173 m/s) projectile path shown in Fig. 24a. Transition pressure is 70 MPa. Chain-dash curve assumes combustion of full surface area when $P_g > P_{tr}$; other curves assume combustion of exposed surface area when $P_g > P_{tr}$	69

Intentionally Left Blank

LIST OF TABLES

<u>Table</u>	<u>Page</u>
I Input Parameters for PDC-80.....	63

Intentionally Left Blank

ACKNOWLEDGEMENTS

The author is extremely grateful to Dr. Richard R. Bernecker of the Naval Surface Warfare Center / White Oak Laboratory (NSWC/WO) and to the Strategic Systems Program Office, Department of the Navy, for their encouragement and financial support during the last five years. It was a distinct privilege to be a part of a talented group of individuals assembled by Dr. Bernecker under the HARP Program (Hazard Assessment of Rocket Propellants). Whatever modest success these studies have achieved is due primarily to the technical interaction within this group. The author gained immeasurable knowledge and insight from discussions with Dr. Bernecker, Dr. Harold W. Sandusky (NSWC/WO), Dr. Melvin R. Baer (Sandia National Laboratory / Albuquerque), Prof. Wayne L. Elban (Loyola College, Baltimore, formerly with NSWC/WO), Dr. Edward L. Lee (Lawrence Livermore National Laboratory), Dr. John M. McAfee (Los Alamos National Laboratory), Dr. Sigmund J. Jacobs (ATR, formerly with NSWC/WO), and Dr. Donna Price (ATR, formerly with NSWC/WO).

Intentionally Left Blank

I. INTRODUCTION AND BACKGROUND

The transition to detonation in confined granular energetic material involves a complicated sequence of events which are influenced by strength of confinement, particle size, permeability, shock sensitivity, and energy release rate during combustion. The response of the granular bed to compressive stress waves appears to play a dominant role in both modes of deflagration-to-detonation (DDT) transition outlined by Bernecker, Sandusky & Clairmont [1] and Bernecker [2]. In Mode I, convective combustion near the ignitor end of the confined column creates a rapidly increasing pressure field which propagates into the unburned material as a compressive wave system. This stress wave system can compact the granular aggregate, altering the propagation rate of the convective flame. If the pressure rise from combustion is sufficiently rapid to drive the compaction front to shock wave strength, then unburned material may be ignited by mechanical compression and a pathway to detonation is available. In Mode II, combustion leads to a mild rate of pressurization of the bed, although compaction of the aggregate may be extensive. Suddenly at some point within the bed, a violent reaction drives a rapid pressure build-up (which may propagate in both directions) and this leads to shock wave formation and provides the pathway to detonation. In these scenarios, the flow of gaseous combustion products and the propagation of stress waves are intimately coupled. However, an initial convective flow of hot gases from an ignitor system or as the result of a deflagration is not a prerequisite for transition to detonation. Impact experiments on a quiescent granular bed show that high strain-rate mechanical compression can also lead to a transition to detonation.

Special laboratory experiments on a number of different materials have provided many important observations about the complex transition process. The DDT studies of Bernecker & Price [3-5], Price & Bernecker [6], Bernecker et. al. [1,7,8], the combustion-driven piston experiments of Campbell [9], McAfee & Campbell [10], MacAfee et. al. [11], and the shock-to-detonation transition (SDT) or impact studies of Sandusky et. al. [12-15], Green et. al. [16], and Dick [17,18] have all contributed to our understanding of the behavior. The data seem to suggest that the latter stages of the transition are essentially independent of the initial stimulus, whether from impact or from hot gas ignition. Even when an ignitor system begins a convective flame, the combustion process plays the role of a piston and drives a system of compression waves into the aggregate. Thus, successful transition to detonation appears to require formation and maintenance of a strong compressive wave which ignites unburned material in its path. The present theoretical studies are directed toward an interpretation of this wave, before a full detonation wave has been established.

Theoretical predictions of the transition to detonation in confined granular energetic material have been underway for a number of years. Models developed by Baer & Nunziato [19,20], Weston & Lee [21], Aldis et. al. [22], Price et. al. [23-24], Kim [25], Hsieh & Kim [26], Butler & Krier [27], Krier & Kezerle [28], Akhatov & Vainshtein [29,30], and Ermolaev et. al. [31] originally focused on DDT, but most now have the ability to simulate impact-generated compaction waves also. These analyses employ a variety of constitutive assumptions, governing equations, ignition and combustion models, and numerical solution techniques. These differences can lead to different predictions for the same problem as illustrated, for example, in Ref. 32. However, a detailed review of all the models is well beyond the scope of this discussion. Instead, the objective of this report is to summarize the content and major results from four modeling efforts [33-36] developed recently by the present author in an attempt to understand the behavior of impact-

generated compaction waves. Two of these models share similar features with the work of Baer & Nunziato [19,20].

The ultimate goal for any model is predictive capability, although few ever achieve it. A less spectacular but worthwhile goal is the simulation of an experiment, where "simulation" may involve the calibration of certain model parameters at some stage in the comparison or calibration to data from similar runs. Even with this compromise, the model simulation can sometimes offer an explanation for observed behavior. However, before attempting any simulation, an absolute necessity is the ability to uniquely specify the boundary conditions and/or source terms which drive the experiment. If the simulation problem is posed such that various combinations of boundary values and source terms could be chosen as reasonable, then comparison of model predictions with experimental data will be meaningless. A major problem in simulating a DDT experiment is the difficulty in providing a unique mathematical description of the ignitor stimulus, i.e., specifying the spatial distribution and time-history of mass flux and energy content of the ignitor system. Impact experiments can circumvent this problem by providing a unique time-dependent boundary condition from experimental observations of the velocity or position of the projectile face as a function of time. The present modeling studies were designed to exploit this advantage.

For several years now, the Naval Surface Warfare Center has been investigating the effects of impact on confined granular material with an apparatus known as the piston-driven-compaction (PDC) experiment. The PDC experiment [12-15], shown schematically in Fig. 1, is essentially a powder gun which drives a flat-faced cylindrical Lexan projectile into a confined column of granular material. Strength of confinement can be varied from a thick-wall Lexan tube to a heavy-wall steel tube, each allowing different diagnostics. Experimental data for the location of the projectile as a function of time after impact provide a unique boundary condition for a model. Varying the initial speed of projectile impact produces results from a benign compaction wave all the way to a transition sequence ending with high order detonation. The ability to predict this behavior would enhance the credibility of any theoretical analysis.

The modeling studies summarized here are focused on the PDC experiment. The objectives of this effort are to interpret and understand

- (a) the properties of the initial impact-generated compaction wave,
- (b) the compressive ignition behavior, and
- (c) the acceleration of the compaction wave to a strong reactive shock wave.

Each of the four models to be discussed will attempt to address one or more of the objectives by simulating some aspect of the PDC experiment, often within the simplest possible framework. Each analysis depends in some way on a constitutive model of the granular aggregate (two-phase mixture) which is denoted the "equilibrium stress state" and described in detail in Section II. Sections III-VI summarize the formulation of and important results from each model:

Section III - Compaction wave behavior with no reaction or combustion, but porosity adjustments in the granular aggregate are governed by a rate-dependent mechanism.

Piston-Driven-Compaction Experiment

Sandusky et. al. [12-15] / NSWC

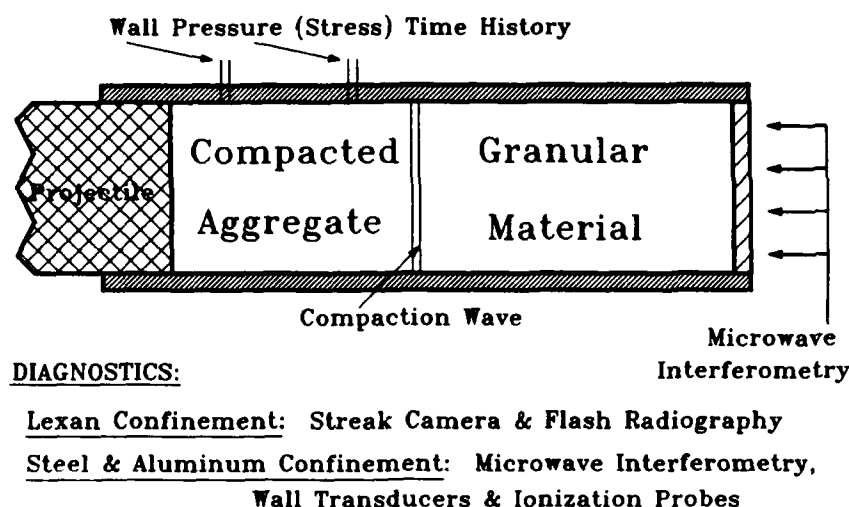


Figure 1 - Schematic of the NSWC piston-driven-compaction (PDC) experiment [12-15] and present modeling problem.

Section IV - Quasi-steady compaction wave behavior with instantaneous adjustment to the equilibrium stress state, but compaction/shock wave can induce some reaction of energetic material within the wave front.

Section V - Simulation of collision of two reactive compaction/shock waves (model of Section IV) along with predictions for the resultant flow field if the collision induces an increase in reactivity.

Section VI - Simulation of the PDC experiment with a transient reactive shock wave theory which accounts for wave-induced reaction, gas-phase combustion of a reactive intermediate species, and ignition and transient combustion of the granular solid.

It may be appropriate here to review just what constitutes a "model" in the present context. Although the four analyses are different, each must contain

(a) a system of conservation laws or balance equations based on a consistent set of assumptions,

(b) a set of constitutive submodels for the gas phase, the solid phase, the two-phase mixture, all phase interaction effects (drag, heat transfer, etc.) which are physical processes occurring on a smaller scale than will be resolved by the numerical solution to conservation laws, prescriptions for ignition and combustion of both phases, and

(c) a numerical integration technique which will minimize artificial distortion of the solution being sought.

Much of this information is outlined in the discussion to follow, but the reader is urged to consult the given references for more detail on each model.

II. DESCRIPTION OF THE GRANULAR AGGREGATE

Predicting the behavior of compacted granular energetic material with an analysis which resolves micro-mechanics at the grain level is virtually an intractable problem. Clearly, some compromise is required. To the author's knowledge, all current theoretical analyses used to predict the transition to detonation assume that each elemental volume contains a binary mixture, i.e., that portion of the volume not occupied by the solid is assumed to be gas. This introduces a porosity variable to define the fraction of the volume occupied by the solid, and its counterpart for the gas:

$$\epsilon_s = \text{solid volume fraction} = \text{solid volume} / \text{total volume}$$

$$\epsilon_g = 1 - \epsilon_s = \text{gas porosity} = \text{gas volume} / \text{total volume}$$

A value of solid volume fraction, however, cannot differentiate among particle sizes or shapes; it is simply a state property associated with an aggregate of ill-defined granular material. One consequence of this simplification is the necessity for a phenomenological sub-model which can link porosity of the aggregate to its stress state. Of course, it should be anticipated that the value of certain parameters will be determined by matching the model response to experimental data for the material in question. In a similar vein, other phenomenological sub-models will be required to describe the drag force and heat transfer between phases. These must also be externally calibrated on the basis of experimental data.

A. Implications of Constitutive Assumptions

The particular choice of a sub-model to describe the dependence of the aggregate stress state on porosity has a significant influence on the solution to the equation system. For situations of interest here, the constitutive behavior of the pure gas phase can be assumed strain-rate independent. Similarly, the constitutive behavior of the solid at theoretical maximum density (TMD) can also be assumed rate independent, although this is not universally true. However, since compression of an aggregate of granular solids involves simultaneous sliding, deformation, and possibly fracture (depending upon the type of material), it is highly likely that rate-dependent resistance forces will be encountered. These unknown forces are sometimes modeled with a global parameter called compaction viscosity [see Refs. 19, 20, 33 and Section III] in a rate-dependent equation which relates a differential force field to the time derivative of a porosity variable. If the governing equation system for the mixture neglects diffusive effects such as Fourier heat conduction (not interphase heat transfer) and viscous stresses (not interphase drag), but includes the rate-dependent description of porosity change, the solution will predict compaction waves with finite thickness. This can be traced to the dispersive effect created by the rate-dependent porosity equation. For most compaction waves, the PDC experiments [12-15] indicate an upper bound for wave thickness which is slightly greater than 6 mm. If an analysis employs the assumption that compaction viscosity is vanishingly small, then porosity instantaneously adjusts to its new equilibrium value and the rate-dependent equation is replaced by an algebraic constraint equation. Under this assumption, the solution to the reduced system of governing equations predicts that compaction waves are infinitesimally-thin shock waves. If the numerical solution predicts otherwise, the finite thickness is due to artificial diffusion added by the numerical integration technique. The modeling choice between rate-dependent and rate-independent porosity adjustment creates much the same situation as in gas dynamics: the inviscid assumption leads to

shock waves as discrete discontinuities while retaining diffusive transport leads to shock waves with finite thickness. The model discussed in Section III employs a rate-dependent porosity adjustment (similar to one used quite successfully by Baer and Nunziato [19,20]), while the models discussed in Sections IV-VI employ an instantaneous (rate-independent) porosity adjustment to the equilibrium stress state and track compaction waves as moving discontinuities.

Another important consideration is the treatment of the solid phase material. Compaction of a granular aggregate can involve changes in density of the solid particles as well as rearrangement and deformation of the particles. Quasi-static compaction experiments such as those conducted by Elban [37,38] and Campbell, Elban & Coyne [37] monitor various stresses as a function of mixture volume. To deduce the associated values of porosity (or solid volume fraction) requires a theoretical model of the mixture. If solid-phase density is assumed constant (incompressible), then porosity values are determined directly by the observed volume change. For materials of interest in this study, the incompressibility assumption can easily lead to predictions of mixture density which have exceeded the value of TMD at atmospheric pressure (recall that TMD is a function of pressure and internal energy). Furthermore, predictions of wave propagation speed in the mixture will be in error. The present study will avoid these problems by accounting for compressibility of the solid-phase material.

B. Compressibility of the TMD Solid

Compressibility of the solid phase at TMD is predicted on the basis of an assumed linear path in the shock velocity (V_s) / particle velocity (u) plane as outlined in [40]. If the Hugoniot of the TMD solid is represented as

$$V_s = a_{sh} + A_{sh} u \quad (1)$$

then the solid-phase equation of state can be written as

$$P_s(\rho_s, e_s) = \rho_{s_0} \Gamma_0 \left[(e_s - e_{s_0}) / (R + 1) \right] + P_{s_0} \left[1 + \Gamma_0 R / (R + 1) \right] - \left(\rho_{s_0} a_{sh}^2 / 2 \right) \left[2 + \Gamma_0 R / (R + 1) \right] R / (1 + A_{sh} R)^2 \quad (2)$$

$$\text{where } R \equiv (\rho_{s_0} / \rho_s) - 1$$

Prediction of pressure versus density (Eq. 2 with $a_{sh} = 2.74$ km/s, $A_{sh} = 2.65$ and $\Gamma_0 = 1.1$) for an isothermal compression of TMD HMX is shown in Fig. 2 below along with a comparison to the prediction from the Helmholtz Free Energy function used by Baer & Nunziato [19], and data from Olinger et. al. [41]. The two theories give almost identical results which compare quite favorably to Olinger's data.

ISOTHERMAL COMPRESSION * LINEAR SHOCK HUGONIOT VRS. BAER/NUNZIATO * B-HMX *

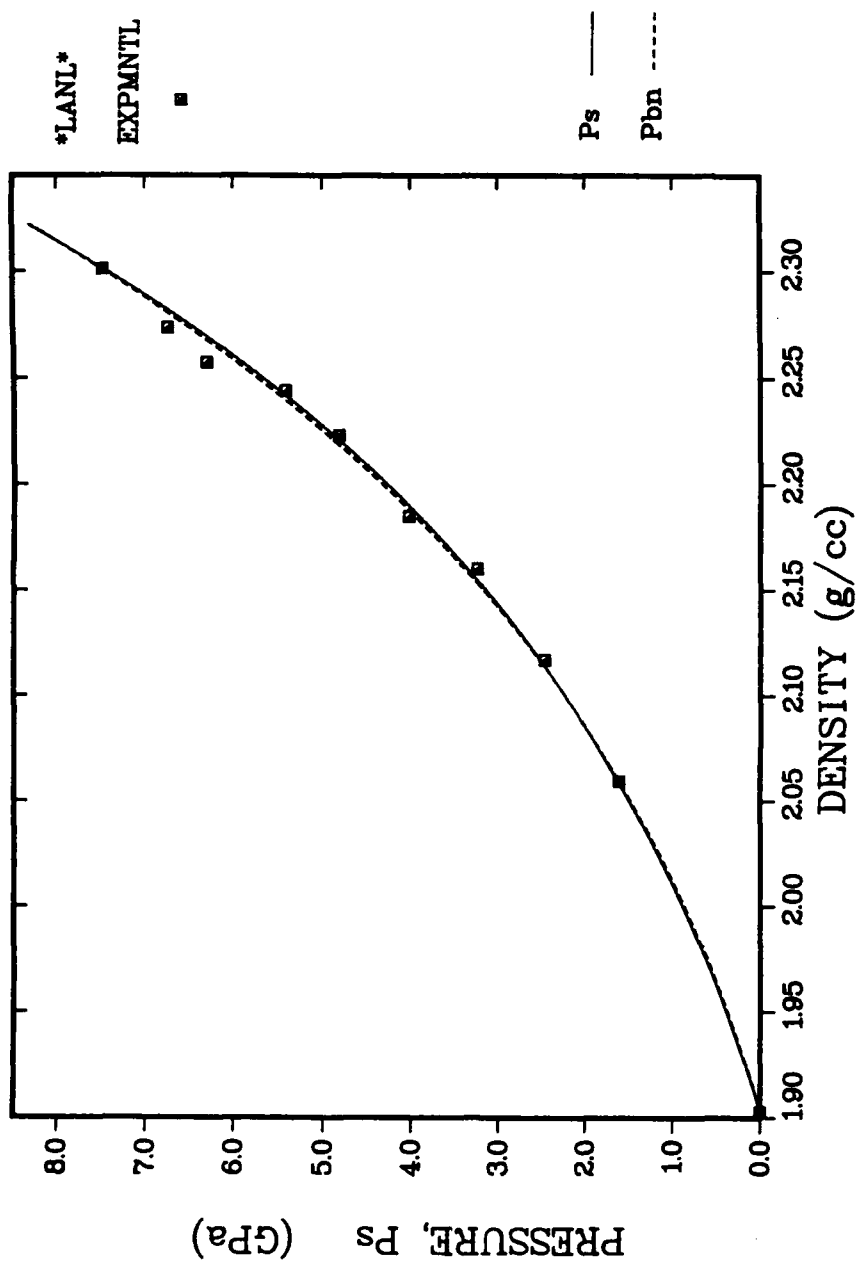


Figure 2 - Pressure vs. density for an isothermal compression of HMX at theoretical maximum density (TMD). Data for β -HMX are from Olinger et. al. [41]. Solid line (P_s) from Eq. (2). Dashed line (P_{bn}) is from theory of Baer & Nunziato [19].

C. Equilibrium Stress State of the Mixture

The solid phase material exhibits strength, and unlike the gas phase, can support deviator stress components. Anticipating a uniaxial strain calculation, the two principal stresses in the solid phase will be labelled,

$$\sigma_s = \text{axial component of solid-phase stress}$$

$$\sigma_r = \text{radial component of solid-phase stress}$$

with a sign convention that positive values are in compression. Two major assumptions will be employed here. The first assumption is that the mixture stress tensor can be represented as,

$$\sigma_{mx} = \epsilon_s \sigma_s + \epsilon_g P_g = \text{axial component of mixture stress tensor} \quad (3)$$

$$\sigma_{mr} = \epsilon_s \sigma_r + \epsilon_g P_g = \text{radial component of mixture stress tensor}$$

The second assumption concerns a unique relationship between σ_r and σ_s which is borne out by the experimental compaction data [39,42,43] for several materials of interest here. This is

$$\sigma_r = \xi(\epsilon_s) \sigma_s \quad \text{where} \quad \xi(\epsilon_s) \equiv \left(\frac{\sigma_{mr}}{\sigma_{mx}} \right)_{\text{experimental}} \quad (4)$$

which is illustrated in Fig. 3 below for the double-base ball propellant denoted TS-3659. Note that under conditions of the quasi-static compaction experiment [37-39], the contribution of gas-phase pressure is negligible and hence the definition of $\xi(\epsilon_s)$ closely approximates the ratio of σ_r/σ_s . The values of solid volume fraction ϵ_s associated with the data points in Fig. 3 were computed from experimental values of mixture density and theoretical estimates of solid-phase density based on Eq. (2). The solid line shown in Fig. 3 represents the function assigned to $\xi(\epsilon_s)$; note that the aggregate begins deforming as a fluid medium ($\xi = 1$) at ϵ_{s0} .

When the mixture deforms in uniaxial strain, the spherical stress component, P_m , follows directly from

$$P_m = (\sigma_{mx} + 2\sigma_{mr})/3 = \epsilon_s(\sigma_s + 2\sigma_r)/3 + \epsilon_g P_g \quad (5)$$

Invoking the relationship in Eq. (4) produces

$$(\sigma_s + 2\sigma_r) / 3 = \sigma_s \psi(\epsilon_s) \quad \text{where} \quad \psi(\epsilon_s) = [1 + 2\xi(\epsilon_s)] / 3 \quad (6)$$

which uniquely defines the function $\psi(\epsilon_s)$. If the spherical component of the solid phase, P_s , is defined as

$$P_s = (\sigma_s + 2\sigma_r) / 3 = \sigma_s \psi(\epsilon_s),$$

then the mixture pressure, P_m , can be written as

$$P_m = \epsilon_s P_s(\rho_s, \epsilon_s) + \epsilon_g P_g(\rho_g, \epsilon_g) \quad (7)$$

* QUASI-STATIC STRESS STATE * 60% TMD TS-3659 * 59% Data: Elban, Coyne, Campbell

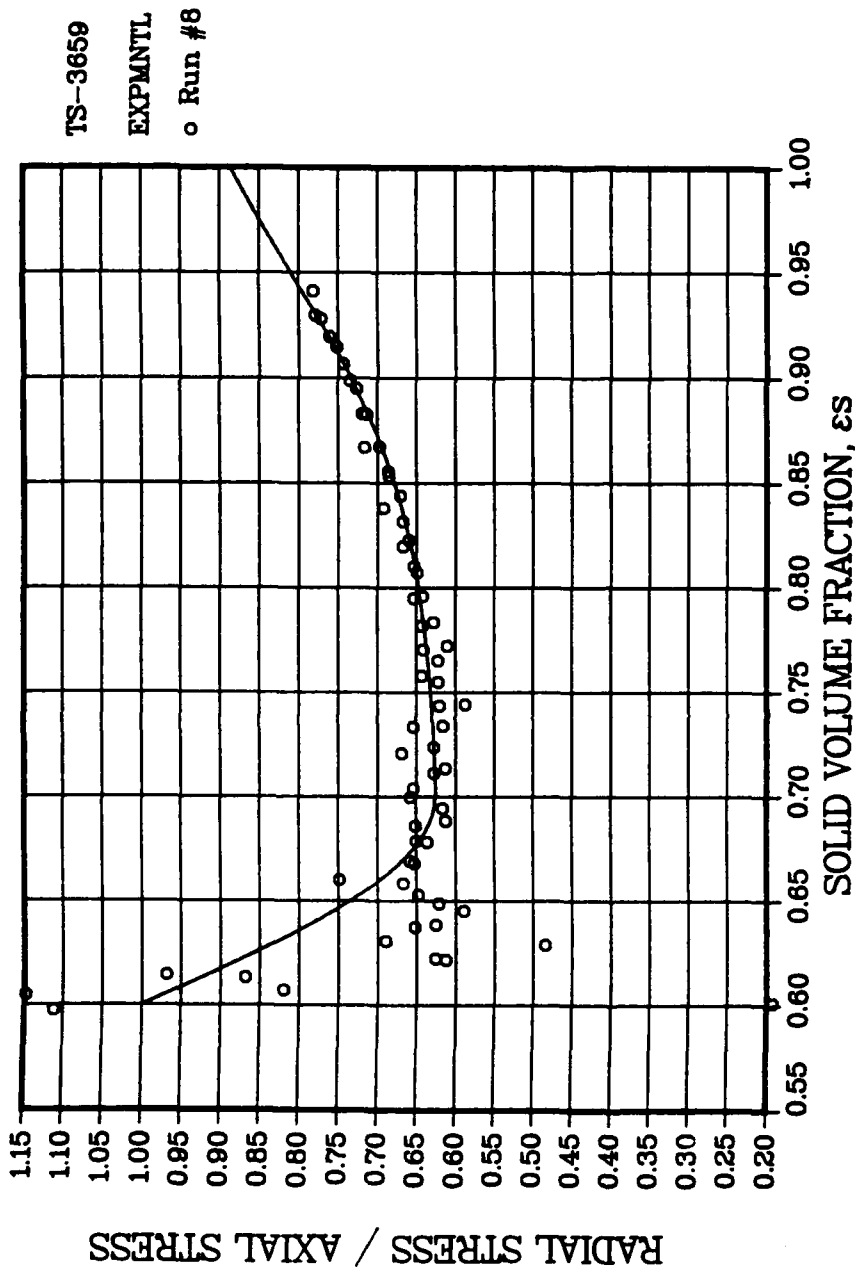


Figure 3 - Ratio of σ_r/σ_s for double-base ball propellant TS-3659 initially at 60% TMD. Solid line is function $\xi(\epsilon_s)$. Experimental data are values of σ_{mr}/σ_{mx} from Run #8 in Ref. 42.

Constitutive theory must supply prescriptions for P_s , P_g , and a method to compute ϵ_s . The phenomenological model of porosity change in the aggregate is a modified version of the concept originally presented by Carroll & Holt [44]. Under quasi-static conditions, the equilibrium constraint on solid volume fraction is a force balance in the axial direction given by

$$\sigma_s(\rho_s, e_s, \epsilon_s) - P_g(\rho_g, e_g) = \frac{P_s(\rho_s, e_s)}{\psi(\epsilon_s)} - P_g(\rho_g, e_g) = \beta_s(\epsilon_s) \quad (8)$$

The quasi-static compaction behavior of a given granular mixture is built into the term, β_s , which represents the "strength" of the aggregate in the axial direction which must be exceeded to further increase the solid volume fraction. It is represented as

$$\beta_s(\epsilon_s) = \tau_1 \left[1 - \zeta^{p_1} + B_2 \left(\zeta^{-p_2} - 1 \right) \right] \ln(1 / \epsilon_g) \quad (9)$$

where $\zeta \equiv (\epsilon_g / \epsilon_{g_0})$

and τ_1 , p_1 , B_2 , and p_2 are constants to be determined by comparison to experimental data. τ_1 has units of stress, but the others are nondimensional.

The equilibrium stress state is determined by the root of the force balance in Eq. (8). Calibration of the parameters in the expression for $\beta(\epsilon_s)$ [Eq. 9] is an iterative process to produce the best comparison of σ_{mx} to the experimental quasi-static compaction data as a function of mixture density. The results for an isothermal compression of TS-3659 ($\tau_1 = 2.6$ Kpsi, $p_1 = 5.5$, $B_2 = 3.2$ and $p_2 = 0.08$) are shown in Fig. 4. The dashed line represents theoretical values of mixture pressure, P_m , and follows from Eq. (7). The chain-dot line shows the variation in TMD predicted by Eq. (2). The results in Fig. 5 for the radial component of mixture stress verify the utility of $\xi(\epsilon_s)$ represented with the solid line in Fig. 3. Reference 34a contains an appendix which lists the values of the four constants in Eq. (9) for a number of different propellants and two inert materials. Note, however, that the values determined in Ref. 34 follow from the early analysis which implicitly assumes that the mixture stress tensor is a pressure ($\xi = 1$).

Two important points about the equilibrium stress state deserve emphasis. First, the two phases in the mixture have different stress states, except under conditions of a fluidized bed. The label "equilibrium" does NOT mean that both phases are forced to coexist at the same stress level. Instead, equilibrium implies the final relaxed state if the process were time-dependent. And secondly, the equilibrium stress state is calibrated with data from the quasi-static compaction experiment [37-39] under conditions where the contribution from gas-phase pressure is negligible. However, the equilibrium stress state follows directly from the root of Eq. (8) which is indeed sensitive to the value of P_g . Combustion-generated gas pressure can lead to an equilibrium stress state different than the quasi-static state for equivalent values of mixture density. Under conditions of vigorous reaction when P_g attempts to exceed P_s , tension is disallowed by setting $\beta_s = 0$ and the mixture "unloads" to a fluidized bed.

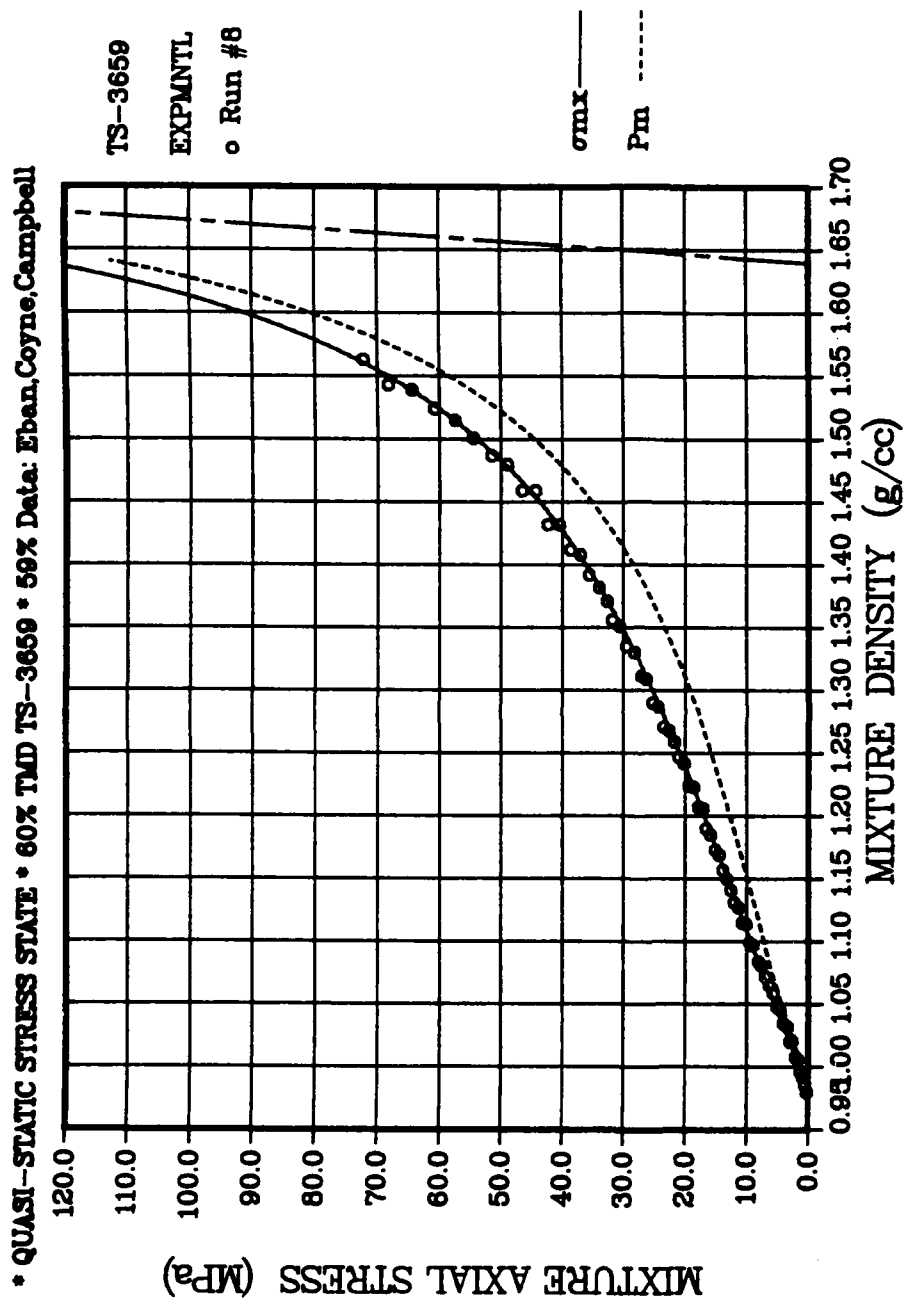


Figure 4 - Axial component of mixture stress as a function of mixture density for an isothermal compression of 60% TMD TS-3659 propellant. Solid line represents σ_{mx} from Eq. (3), dashed line is P_m' and chain-dot line is TMD from Eq. (2). Data from Run #8 in Sandusky et al. [42].

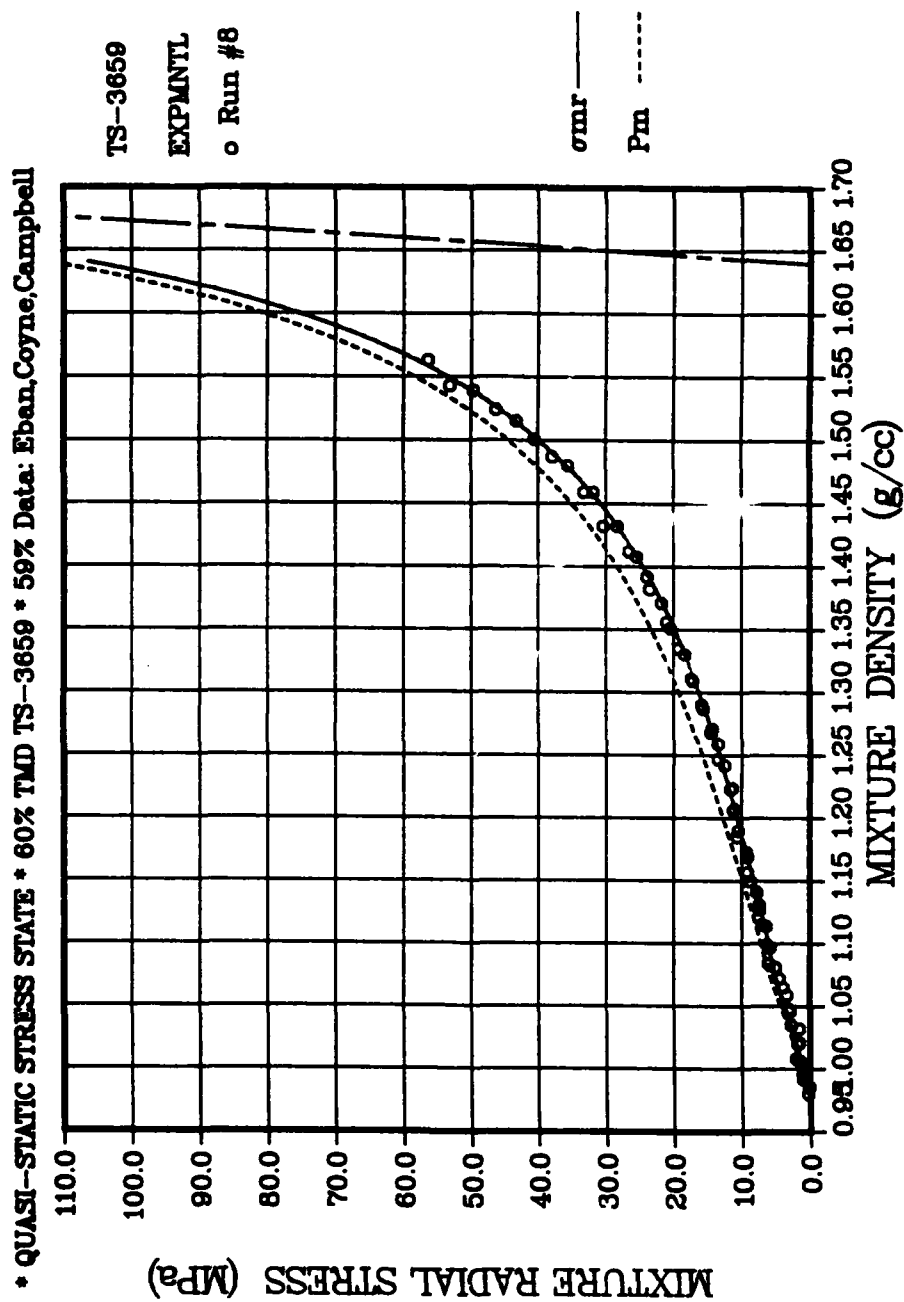


Figure 5 - Radial component of mixture stress as a function of mixture density for an isothermal compression of 60% TMD TS-3659 propellant. Solid line represents σ_{mr} from Eq. (3), dashed line is P_m , and chain-dot line is TMD from Eq. (2). Data from Run #8 in Sandusky et. al. [42].

D. Rate-dependent Porosity Change

As mentioned in Section IIA, compression of a granular aggregate involves simultaneous grain sliding, deformation and possibly fracture (if the material is brittle), and hence it is likely that strain-rate dependent resistance forces will be encountered. To assess the importance of this effect, one of the modeling studies (Section III) provided for rate-dependent porosity change of the aggregate. In a manner similar to the work of Baer & Nunziato [19,20], these unknown resistance forces are modeled with a global parameter called compaction viscosity, μ_c , which linearly relates the time derivative of solid volume fraction along the solid-phase streamline to the differential force field describing the equilibrium stress state. Thus, for the case when $\xi = 1$,

$$D(\epsilon_s)/Dt_s = (\epsilon_g/\mu_c) [P_s - P_g - \beta(\epsilon_s)] \quad (10)$$

The influence of this mechanism on compaction wave behavior will be discussed in Section IIIA.

E. Gas-phase Equation of State

A reactive gas-phase mixture is modeled with an elementary description which envisions two gas-phase species:

Y_1 = mass fraction of reactive intermediate species R_1 at energy level Δe_{gr}^0 ,
and
 Y_2 = mass fraction of final combustion product R_2 at energy level e_g^0 .

Mass conservation implies $Y_1 + Y_2 = 1$. Section VI discusses the finite rate of conversion from R_1 to R_2 which has the major effect of simulating the release of energy as intermediate "reactants" form final combustion products. The gas-phase mixture is described with a simple constant co-volume equation of state given by,

$$P_g (1 / \rho_g - b) = (R_o / M) T_g \quad (11)$$
$$\text{and } e_g = c_v (T_g - T^0) + (Y_1 \Delta e_{gr}^0 + Y_2 e_g^0)$$

where γ (c_p/c_v), M (molecular weight), and b (co-volume) are constants whose values are selected as reasonable averages from BLAKE Code [45] runs for each propellant composition. This representation only approximates the real gas behavior of the mixture, but it is adequate for the present investigation except near conditions of detonation.

F. Phase Interaction Effects

The flow of gases through the aggregate creates a drag force per unit volume, f_d , which is modeled with the Jones-Krier correlation [46],

$$f_d = \rho_g \left(\frac{\varepsilon_s}{d_p} \right) (u_g - u_s) |u_g - u_s| \left(3.89 \tilde{R}_e^{-.13} + 150 / \tilde{R}_e \right) \quad (12)$$

$$\text{where } R_e \equiv \rho_g d_p |u_g - u_s| / \mu_g \quad \tilde{R}_e \equiv \left(\frac{\varepsilon_g}{\varepsilon_s} \right) R_e$$

modified by the tortuosity factor used by Gough [47] in the NOVA interior ballistics code. Before grain burning commences, convective heat transfer rates from hot gas to cold solid are computed from the convective heat transfer coefficient,

$$h_g = 2 k_g \left(1.0 + 0.2 \text{Pr}^{1/3} R_e^{2/3} \right) / d_p \quad (13)$$

Ignition of the solid is assumed to occur when the solid-phase surface temperature exceeds an arbitrary constant value (e.g., 473°K for TS-3659 ball propellant). The time-dependent calculation of surface temperature is done with Baer's [48] method which approximates the solid-phase thermal profile with a polynomial and creates an ordinary differential equation in time. Heat transfer and combustion enter the two-phase mixture equations as "m" and "q" which are per unit total volume. Because several of the materials of interest here are spherical ball propellants, the present analysis has extended the work of Jacobs & Sandusky [49] and derived an expression for S_{tv} , the exposed surface area per unit total volume associated with the deformed lattice,

$$S_{tv} = \frac{6 \varepsilon_s}{a_p} \left[\frac{g(R_p / a_p)}{f(R_p / a_p)} \right] \quad (14)$$

where $a_p \equiv$ distance between deformed particle centers

$R_p \equiv$ radius of deformed particle

$$f(R_p / a_p) \equiv (2 R_p / a_p)^3 - n_c [(R_p / a_p) - 1 / 2]^2 [(4 R_p / a_p) - 1 / 2]$$

$$g(R_p / a_p) \equiv (2 R_p / a_p) \{ (2 R_p / a_p) - n_c [(R_p / a_p) - 1 / 2] \}$$

Both "m" and "q" are computed on the basis of S_{tv} .

The wall boundary friction force can be computed from data provided by the quasi-static compaction experiment [37,38] as,

$$\text{friction force} = (\text{applied force} - \text{transmitted force}) / (\pi \times \text{diameter} \times \text{length})$$

Then,

$$\text{coefficient of boundary friction} = \text{friction force} / \sigma_{mr}$$

This coefficient for TS-3659 ball propellant is plotted in Fig. 5 of Ref. 36, and is shown to increase as the aggregate is compressed. The computations for TS-3659 presented here have assumed the worst case and taken the maximum value of 0.20 as a constant. Thus, $f_w = 0.20 \sigma_{mr}$.

III. COMPACTION WAVE MODEL WITH FINITE-RATE POROSITY CHANGE [33]

This model was the initial effort. The objective was to understand the early stages of the PDC experiment by simulating the propagation of an inert impact-generated compaction wave in confined granular material. Hence, all combustion and/or reaction events are deliberately ignored. As in all the models, deformation of the aggregate (two-phase mixture of compressible solid grains and gas) occurs in uniaxial strain. In this model, traction forces (friction) between the sliding aggregate and the lateral confining boundary are assumed negligible. Since the quasi-static compaction experiment was not yet measuring a radial stress component when this model was under development, the mixture stress tensor is represented with the spherical component, i.e., a pressure only ($\xi = 1$).

The central focus here is the behavior of the granular aggregate. As mentioned in Section II, compression of a granular mixture involves simultaneous grain sliding, local grain deformation and possibly fracture if the solid material is brittle. It is quite probable that these events will give rise to strain-rate dependent resistance forces. An assessment of this influence is important. Because the micro-mechanics at the grain level present an intractable computational problem, the combined effect of these unknown forces is modeled with a global parameter called compaction viscosity, μ_c . Since this is not a fundamental material property, its magnitude will have to be determined by calibration of the final solution. Similar to the formulation used by Baer & Nunziato [19-20], compaction viscosity linearly relates the time rate-of-change of solid volume fraction along the solid-phase streamline to the differential force field describing the equilibrium stress state. This relationship is given by Eq. (10), which shows that the equilibrium stress state is recovered as the volume strain-rate vanishes. The remaining six balance equations (conservation of mass, momentum and energy for each phase) are given in Ref. 33, and are quite similar to those listed in Section VI. The total system of seven equations was re-written in characteristic form (no small feat in itself) and the numerical solution was obtained by the method-of-characteristics.

The rate-dependent porosity adjustment creates a dispersive effect on the compaction wave, i.e., wave thickness will tend to increase with distance propagated. However, nonlinear convection attempts to steepen the wave profile, counterbalancing the dispersive effect. For the case of constant velocity impact on the granular bed, the prediction shows a compaction wave which rapidly approaches a constant thickness and steady propagation velocity, in accord with the results of Baer & Nunziato [19]. The original calculations in Ref. 33 which indicated a continuously spreading wave were the result of an interpolation error in the method-of-characteristics solution. Consider an example case of constant velocity (100 m/s) piston impact on a quiescent bed of 73% TMD Class D HMX. The (corrected) prediction for compaction wave structure is shown in Fig. 6 as a plot of mixture pressure versus distance at 20.5 μ s after impact. In this example, the compaction viscosity, μ_c , is 1000 poise and the wave thickness is approximately 5 mm. The predicted steady propagation speed is 450 m/s, while Sandusky observed 438 m/s [PDC-22, Ref. 14]; the difference between the two values is well within the variation attributable to the particle size distribution of Class D HMX.

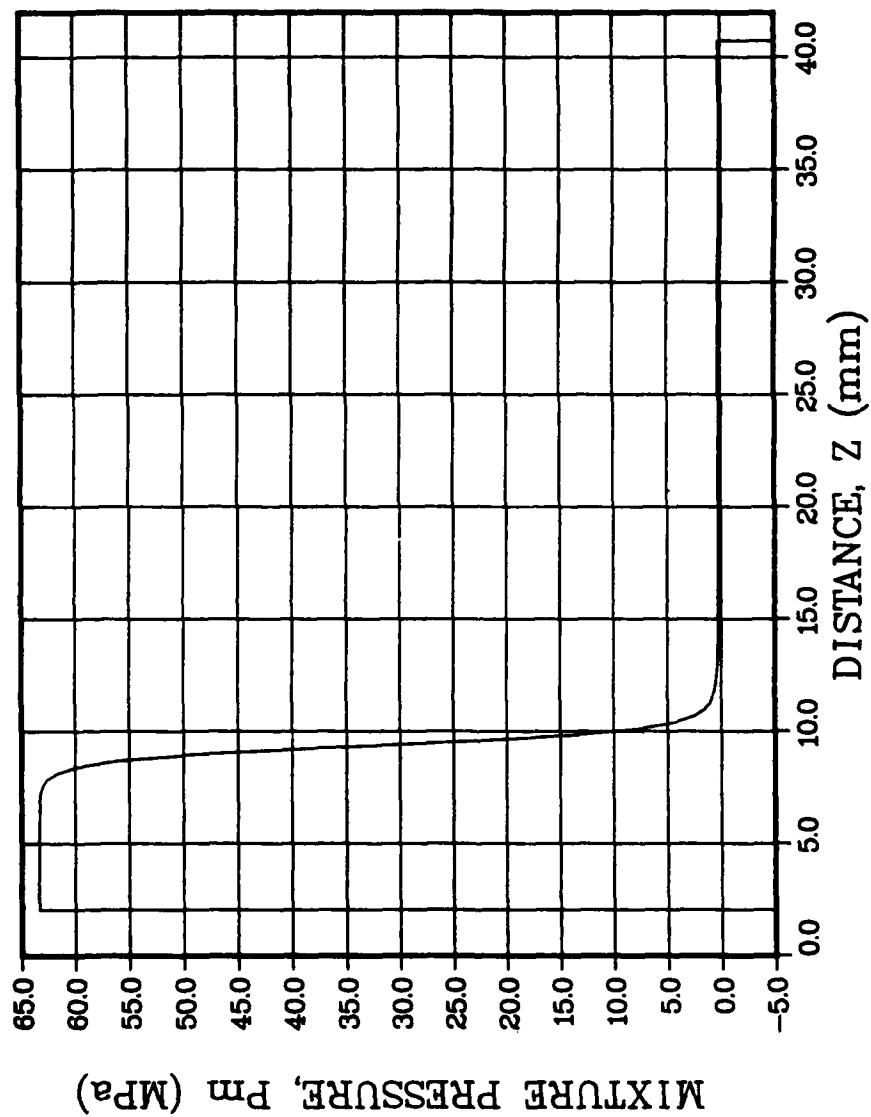


Figure 6 - Constant-velocity piston impact at 100 m/s on 73% TMD Class D HMX. Plot shows distribution of mixture pressure versus distance at a time of 20.5 μ s after impact. Compaction viscosity is 1000 poise. Numerical solution obtained with the method-of-characteristics.

There are several important observations here. The first is that the assumed value of compaction viscosity influences only compaction wave thickness. As intuition might suggest, increasing the value of compaction viscosity creates a "thicker" compaction wave. In the PDC experiment, Sandusky [13,14] estimates an upper bound on wave thickness in HMX and several other materials as the distance between tracer wires, 6.35 mm, which were seeded into the bed. The model simulations show that predicted compaction wave thickness will exceed this upper bound if the value of compaction viscosity is much larger than 1000 poise. Furthermore, the simulation in Fig. 6 demonstrates that the region behind the compaction wave (outside the finite thickness) remains at the steady value dictated by the equilibrium stress state. Secondly, the computed value of steady propagation speed is independent of the value of compaction viscosity. Both observations taken together imply:

(a) The fundamental properties of the compaction wave (propagation speed, and downstream values of pressure, density, and porosity) are apparently functions of the equilibrium stress state. Hence, a complicated time-dependent numerical solution should not be required to predict these properties.

(b) At least for quasi-steady propagation of these compaction waves (with μ_c near 1000 poise), the influence of strain-rate is confined to the region within the wave thickness.

An additional observation is the "dual" structure of the wave, similar in nature to that seen in an "elastic/plastic" material. In the present case, impact on a medium with a rate-dependent equation of state leads to a rapidly decaying transient structure. The major adjustment forced by the abrupt change in particle velocity becomes the slow moving "plastic" wave which is recognizable in Fig. 6 as the compaction front near 10 mm. However, the decaying transient structure also leaves behind a fast moving component which becomes the precursor wave. This precursor is visible in Fig. 6 near 40 mm and propagates with decreasing (and almost negligible) amplitude at a speed slightly less than 2 mm/ μ s. The PDC experiment [12-15] found no evidence for a precursor wave in either the microwave interferometry data or the movement of the tracer wires. If this wave is present, its influence is apparently small. Further discussion on the evolution of the decaying transient structure caused by the initial impact can be found in Ref. 33, along with a reference to the early work of B. T. Chu as reported in Ref. 50. One final result from the model predictions for the transient structure is that the material adjacent to the projectile face undergoes a larger value of volume strain rate than does material which traverses the fully-formed compaction wave. The implication is that if the compressive ignition phenomenon is rate sensitive, then material adjacent to the projectile face should ignite first. This is consistent with most of Sandusky's observations from the PDC experiment [12-15].

IV. EQUILIBRIUM SHOCK WAVE THEORY [34]

This modeling study was an effort to exploit an important result from the rate-dependent model (Section III): the fundamental properties of the compaction wave are apparently functions of the equilibrium stress state. This suggests the interesting limiting case when compaction viscosity is equal to zero, and hence rate-dependent porosity change is replaced by an instantaneous adjustment to the new equilibrium stress state. In this limit, a finite-thickness compaction wave becomes an infinitesimally-thin shock wave, and the details of the wave structure vanish into a mathematical discontinuity. Although a description of the wave structure is lost, the simplified equation system is easier (and faster) to solve. This is rather analogous to the inviscid assumption in gas dynamics which approximates a shock wave as a discontinuity. An additional objective here is to deliberately pose the simplest possible model which might help identify controlling mechanisms in the behavior of compaction waves in granular energetic material. Such an attempt is always haunted with the prospect of neglecting an important part of the physics and thus fatally distorting the predictions. Although the results should be interpreted with due caution, simplicity can sometimes provide insight.

Some interesting questions arise if we relinquish the idea that compaction waves are inert. What changes in behavior would be expected if the compaction wave itself caused a portion of the solid phase material to react? As a compaction wave propagates through granular energetic material, the solid volume fraction is forced to increase abruptly (over a time interval proportional to wave thickness divided by speed). If the strength of the compaction wave increases, the granular aggregate must absorb this work of compaction at increasing strain rate. It is quite improbable that this energy can be deposited uniformly throughout the aggregate. It is more likely that the energy is concentrated in thin zones near grain boundaries or in other regions of material weakness. Hence, above some strain-rate threshold, the temperature of a small amount of solid material may exceed the value to begin reaction. Even if the reaction fails (e.g., quenching by heat loss to surrounding cold solid), a small amount of solid has been converted to high temperature gaseous combustion products. These hot gases will be trapped in the available pores and voids of the collapsing aggregate. Thus the reactive compaction wave leaves behind a compressed aggregate whose available porosity is filled with combustion gases at elevated temperature. Note the important distinction that the combustion gases are created locally by the wave front, as opposed to being driven into the aggregate by a convective flow. This concept provides a mechanism which can transfer the compressive work done at high strain rate in a thin compaction wave into a potential source of ignition distributed throughout the volume. Furthermore, the gaseous combustion products trapped in the porosity of the aggregate can also effect the mechanical "stiffness" of the compressed aggregate, and hence alter the rate of propagation of a compaction wave. Recently, Dick [18] re-examined data from his earlier SDT experiments on 65% TMD HMX and, independent of this work, came to a similar conclusion about the existence of wave-induced reaction.

Compaction waves in this model are treated as reactive shock waves. The mechanism responsible for wave-induced reaction of some portion of the solid material is undoubtedly related to mechanical work done at high strain rate. A description of this process in a granular aggregate involves extremely complex physics and is presently unavailable. Of course, a shock wave model (zero thickness, and infinite strain rate) could not predict the strain-rate history imposed

on material which passes through the compaction wave. To circumvent this problem, the analysis assumes that a prescribed fraction of solid material reacts within the shock front to form gaseous combustion products immediately downstream. Outside the shock front, reaction ceases. In reality, reaction probably does fail when the system is near the limiting condition. For those systems which exceed this limit, it is more likely that reaction "falters" during an induction period and then resumes.

The equilibrium shock wave model [34] of compaction waves intentionally neglects all "loss" mechanisms as well as rate-dependent material processes. Resistance to porosity change is assumed vanishingly small, i.e., the compressed aggregate instantaneously adjusts to its equilibrium stress state [see Section IIC]. Deviator components of the mixture stress tensor are ignored and the equilibrium stress state is based on a mixture pressure. It is assumed that both phases travel at the same velocity in the compressed aggregate, which eliminates gas/particle drag. Inter-phase heat transfer is also neglected, although the two phases may exist at different temperatures. The heat transfer problem is addressed separately in Ref. 34, and this artificial decoupling is removed in Ref. 36. Friction between the compressed aggregate and the lateral confining boundary is ignored. Combustion occurs only within the wave front itself. A specified fraction, η , of the granular solid material can react and form gas-phase combustion products (with a given energy release) during passage of the shock wave, i.e., shock-induced reaction. Although the eventual goal is to be able to predict the value of the important parameter η , at present its value must be specified. Thus, in certain cases, this analysis will be used to interpret experimental data instead of predicting it.

The model problem illustrated in Fig. 7 is used to simulate the PDC experiment. The computational problem involves two shock waves and a contact discontinuity, each of which is treated as a moving internal boundary. One shock wave (V_{s1}) travels back up the Lexan rod (projectile) to arrest its initial motion, and the other (V_{s2}) represents the compaction wave in the granular material. The contact discontinuity is the interface boundary between the compressed Lexan rod and the compacted aggregate. With the assumptions outlined above, constant velocity impact leads to steady propagation of all three waves; there are no transients. This provides a substantial simplification in the solution procedure which is discussed in Ref. 34 along with the equation system.

It is important to note how the assumptions used in the theory enter the comparisons. All "loss" processes have been neglected, and the compressed aggregate behind the compaction shock wave is constrained to the equilibrium stress state. When predictions of compaction wave speed are plotted versus projectile speed, this incorporates the assumption of an ideal momentum transfer at projectile impact, i.e., no losses at impact. On this plot, it is common that the experimental data lie on or below the inert shock wave prediction. When the predictions are plotted versus interface speed (called particle velocity in Sandusky's work), all losses associated with projectile impact have been removed from the comparison. If experimental data lie above the inert shock wave prediction in this plot, some mechanism (such as heat release during reaction) is driving the wave, or dynamic compaction of the aggregate has produced a stress state greater than the equilibrium value.

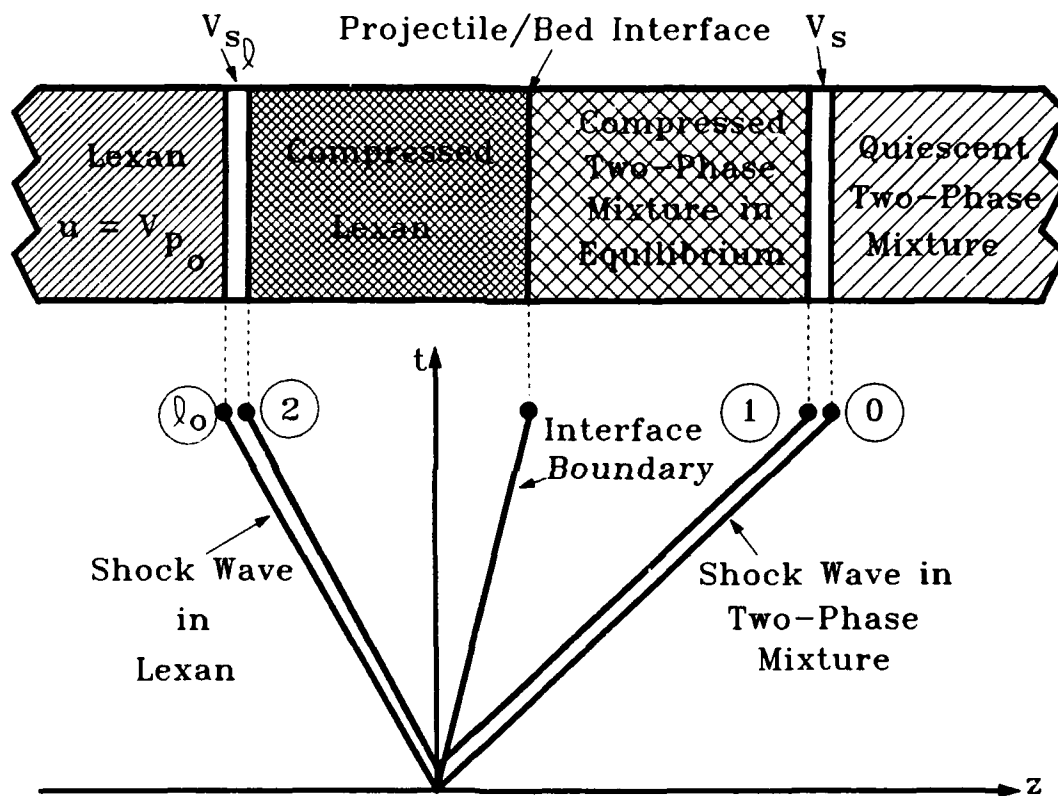


Figure 7 - Schematic of computational problem used to simulate the NSWC piston-driven-compaction experiment [12-15]. Compaction wave in two-phase mixture is reactive equilibrium shock wave.

Predictions from the equilibrium shock wave model have been compared to experimental data from the PDC experiment for many different granular materials (inert and energetic) with widely varying properties. The reader is invited to consult Ref. 34 for details on a number of these comparisons. Three example cases will be discussed here.

A. #20 Sieve Cut from Class D HMX

Cyclotetramethylenetetranitramine (HMX) is a brittle crystalline energetic substance which is a major ingredient in secondary explosives and high energy propellants. Class D HMX is characterized by a broad particle size distribution, and thus successive samples taken from this material may exhibit different mechanical properties. To eliminate this uncertainty, Elban & Chiarito [38] prepared a sieve cut from Class D material which has an average particle size of 925 μm within a narrow distribution. Predictions for compaction wave speed in this material at initial density of 60% TMD are shown in Fig. 8 versus interface speed (particle velocity). Figure 8 also includes data from two PDC experiments [14] conducted in the intermediate confinement provided by the thin-wall aluminum tube which eliminates the uncertainty associated with radial deformation of Lexan tubes. The good comparison between theory and experiment suggests that compaction waves in #20 sieve-cut HMX behave as inert waves, at least up to a particle velocity of 125 m/s. Note that fracture of HMX grains during compression of the aggregate is implicitly included in the equilibrium stress state, but otherwise has been ignored. Of course as these waves increase in strength, they will not remain inert. But the simple theory has provided an important base line to assess the behavior of stronger waves.

B. WC-231 Propellant

A second example is provided by WC-231 which is a double-base (25% NG in NC) propellant whose grains are shaped like "fat pancakes" (rolled spheres) with an average diameter of approximately 790 microns. Predictions for compaction wave speed in 50% TMD WC-231 versus interface speed are compared in Fig. 9 to data from several of NSWC's PDC and CGC (cold gas compaction) experiments [13,14]. The comparison shows that the experimental compaction wave speeds are greater than the model predictions for an inert wave. Since loss mechanisms have been ignored, something has to be "driving" these waves. In principle, rate-dependent resistance to dynamic compaction of the granular aggregate could create an increased stress state which would support the higher speed; however, rate-dependent compaction models [19,20, and Section III] suggest that the magnitude of relaxation time required to maintain this condition for the duration of the experiment would produce excessively thick compaction waves (not indicated by the experiment). The other possibility is wave-induced reaction involving a small fraction of solid material (also postulated by Dick [18]). Since the aggregate is simultaneously being compressed, the newly created combustion gases released into the available porosity of the aggregate are trapped and will exert a pressure. This gas pressure increases the "stiffness" of the two-phase aggregate, which in turn supports an increased compaction wave speed. Computations show that wave-induced reaction (which releases the total heat of reaction of the solid) of a few tenths of one percent of the solid phase creates enough gas pressure to stiffen the aggregate and enable it to support the compaction wave speeds measured in the experiments. Sandusky's [14] comments concerning the extent of reaction eventually observed in two of the experiments are noted in Fig. 9; they support (but do not prove) the concept of a reactive compaction wave.

(text continues on page 24)

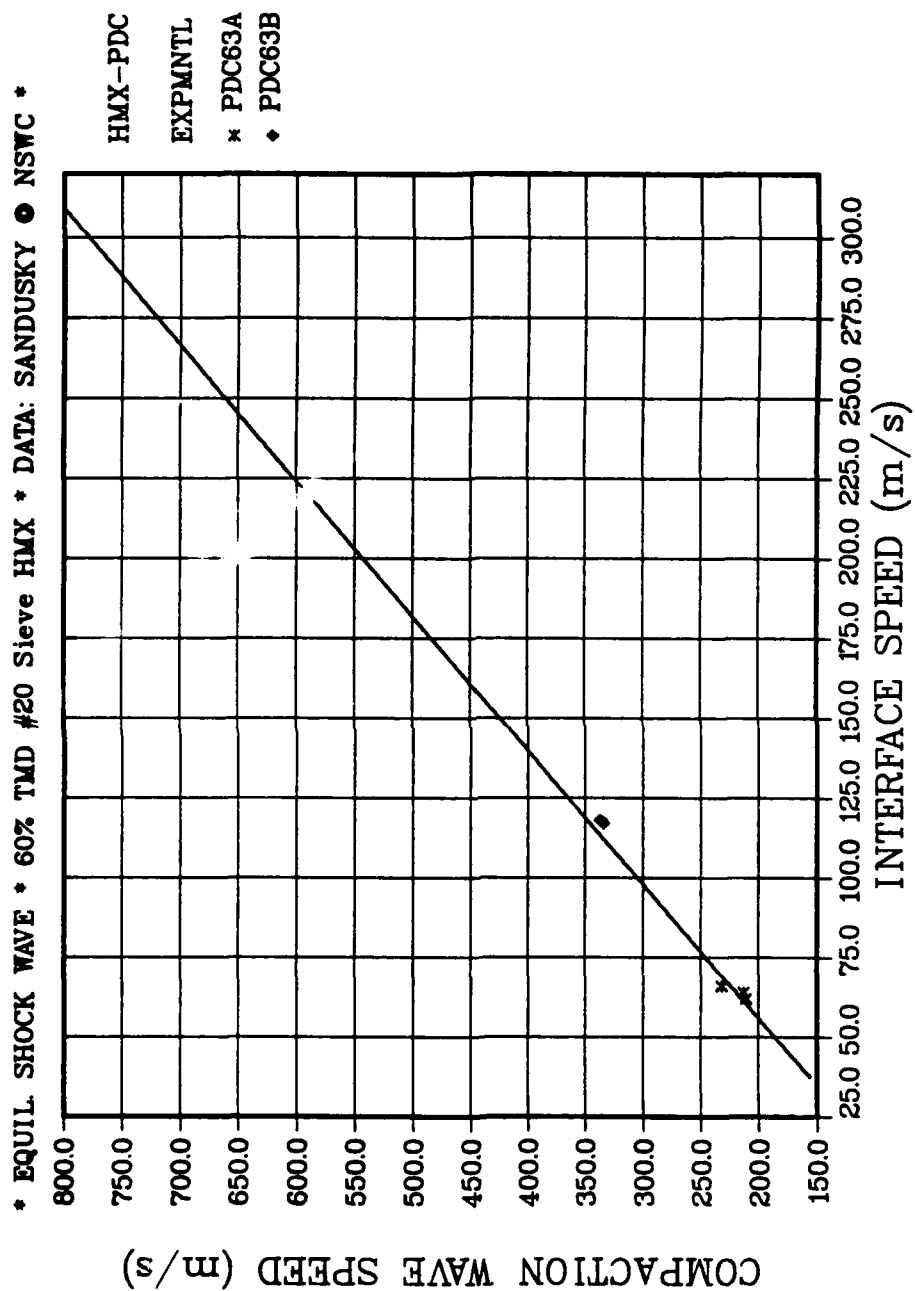


Figure 8 - Predicted compaction wave speed versus interface speed for 60% TMD #20 sieve cut HMX. Solid line represents inert compaction wave. PDC data from Sandusky [13].

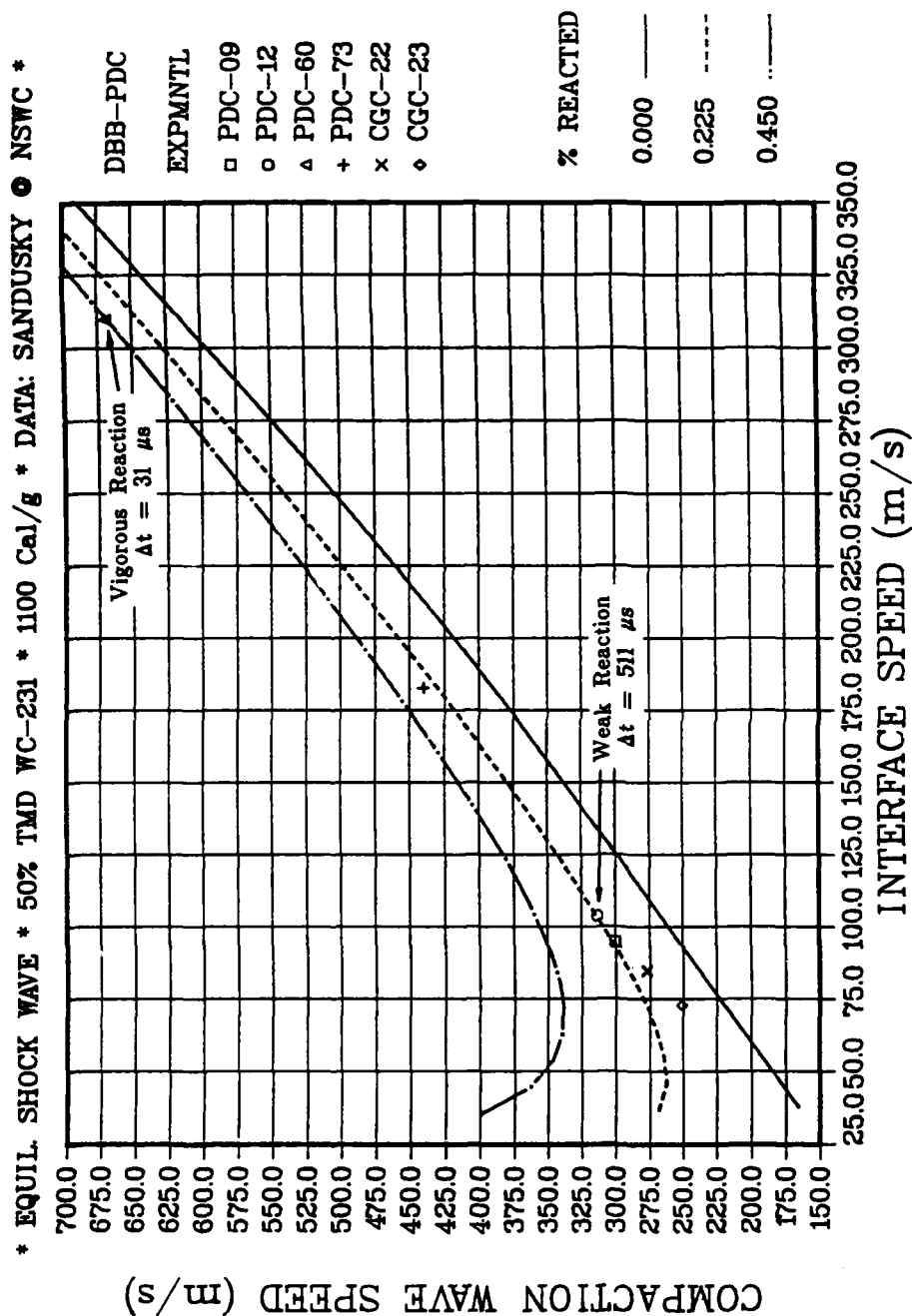


Figure 9 - Predicted compaction/shock wave speed versus interface speed (particle velocity) for 50% TMD WC-231 propellant. Solid line is inert compaction wave, dashed and chain-dot lines involve wave-induced reaction. Data from PDC and CGC experiments [13,14]. Noted on figure are Sandusky's comments for PDC-12 and PDC-60 concerning the nature of the reaction and the interval of time before appearance of visible flame.

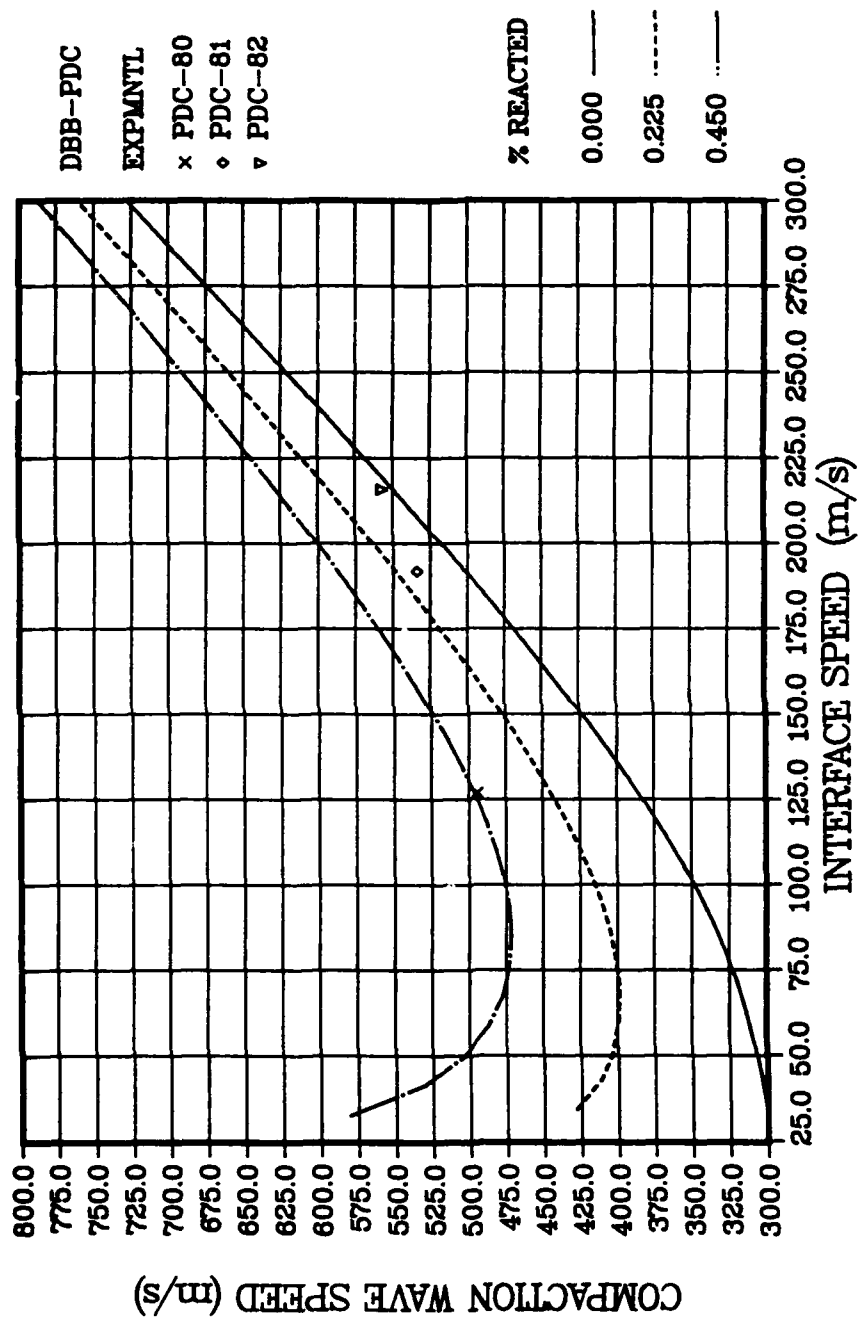


Figure 10 - Predicted compaction wave speed vs interface speed (particle velocity) for 60% TMD TS-3659 ball propellant. Data from the NSWC PDC experiment [15]. Solid line is inert compaction wave, dashed and chain-dot lines involve wave-induced reaction.

C. TS-3659 Ball Propellant

A third example is the granular propellant used as the basis for three out of four modeling problems in the 1988 JANNAF Propulsion Systems Hazards Subcommittee Modeling Workshop [32]. TS-3659 is a double-base (21.5% NG in NC) ball propellant with nearly spherical grains of 434 μm average diameter. Predictions for compaction wave speed are compared in Fig. 10 to NSWC data from the three PDC experiments which backed-up the modeling workshop problems. As in the case of WC-231, the PDC data lie above the prediction for an inert compaction wave suggesting that wave-induced reaction was involved. However, the trend in WC-231 that increasing particle velocities (stronger waves) are accompanied by a monotonic increase in the amount of wave-induced reaction is reversed in TS-3659. This reversed trend also applies to WC-140 single-base propellant and ABL-2523 casting powder. The comparison in Fig. 9 for TS-3659 suggests that as the waves become stronger, a smaller percent of the solid-phase material entering the wave front is involved in reaction. This does not necessarily mean that very strong compaction waves will behave as inert shock waves; experimental evidence is quite the opposite. One possible explanation is that the high strain rate in the stronger waves is momentarily creating high temperature material at grain boundaries which becomes viscous or liquid-like. This viscous layer permits grain sliding and allows the aggregate to collapse toward the equilibrium stress state for inert material, without a proportional increase in reactivity. The existence of these opposite trends (apparent reactivity increases or decreases with wave strength) serves to underscore how little is known about the micro-mechanics at the grain level, and exactly what mechanisms are responsible for compressive ignition of material. Clearly, this problem will require further study.

V. COLLISION OF REACTIVE COMPACTION/SHOCK WAVES [35]

It is common practice to display data from impact experiments (e.g., PDC [12-15] at NSWC), DDT experiments (e.g., Bernecker [8] at NSWC) and the combustion-driven piston experiment (e.g., McAfee [10,11] at LANL) in "Distance-Time" plots. In many cases, these X-T plots appear to show abrupt changes in propagation speed as the compaction wave accelerates to a reactive shock wave (speeds in the range of 1-3 km/s) and then to a detonation wave. Furthermore, Bernecker's DDT experiment [8] with TS-3659 double-base ball propellant shows the presence of a rearward propagating compressive wave, i.e., a wave which propagates back into material which is already burning. The origin of this wave seems to be in the vicinity of an increase in speed of a strong compaction wave.

The PDC experiments have led to the observation [14] that the time to the onset of compressive reaction correlates as " $\tau^2 \Delta t = \text{constant}$ ", where τ is a measure of the stress state in the solid phase and Δt is the time interval after impact. Sandusky notes that the first appearance of "flame" usually occurs in material adjacent to the projectile face. Vigorous combustion in this region will generate and support a stress wave system which must propagate into material already compressed by the initial compaction wave. The objective of this effort was to determine if collision of this wave system with the leading compaction front might produce an altered wave pattern responsible for the abrupt change in speed during acceleration.

A. Model Development

Simulation of the collision between two compaction/shock waves of the same family (the weaker wave is overtaken from behind) employs the reactive equilibrium shock wave model discussed in Section IV. The collision model follows from a simple idea. To begin, consider a piston in contact with a quiescent inert rate-independent medium as sketched in Fig. 11. At time zero, the piston assumes a constant velocity. A plot of this event in the "Distance-Time" plane shows a constant velocity shock wave running ahead of the piston path.

Note the direct analogy of this wave diagram with the flow field produced by steady two-dimensional supersonic flow over a wedge (i.e., the piston path). Focusing on the analogy with supersonic flow for a moment, imagine that the single wedge is replaced with a double wedge, i.e., the body has a second abrupt change in slope (see shaded region in Fig. 12). Of course, this new slope change will create a second shock wave which eventually must collide with the leading shock wave. As illustrated in Fig. 12 for a nonreacting medium, the collision produces a combined shock wave whose strength is intermediate between the strengths of the two waves attached to the body. A centered simple wave system (expansion fan) anchored at the collision point will attempt to equilibrate this pressure difference.

Of course steady supersonic flow over a double wedge is not the problem of interest. However, application of this wave diagram to one-dimensional wave propagation requires an interpretation of the second increase in piston velocity. Once the projectile impacts the granular bed in the PDC experiment, it does not suddenly accelerate to an increased speed after a certain time interval. On the contrary, its velocity may begin to decrease. However, the onset of combustion of material adjacent to the piston face might generate a sudden increase in stress level which would have the same effect as an increase in piston velocity. Thus, the present model will employ an increase in piston velocity to simulate the effect of vigorous combustion which begins at the piston face, after a suitable delay time, and then propagates away from the piston into the compressed aggregate. Note that the combustion process which "begins" at the piston face is the onset of substantial burning in the aggregate since, in the model of Section IV, a small amount of the solid material could have already reacted within the initial compaction wave.

The wave diagram for a double impact shown in Fig. 12 applies to an inert medium. If, however, the medium is reactive and shock waves are capable of inducing energy release, the wave pattern can easily be altered. In particular, if the combined shock wave induces a nominal increase in reactivity compared to the initial shock wave, this will raise the downstream mixture pressure (or stress level) enough to wipe out any expansion wave. Any further increase in reactivity will raise the mixture pressure such that a rearward propagating shock wave will appear in the location of the original expansion wave system, as illustrated in Fig. 13. The dividing streamline (chain-dot line) which passes through the collision point becomes a contact discontinuity between the regions downstream of shock waves (3) and (4) (see Fig. 13). A contact discontinuity separates two regions with different density and temperature, but particle velocity and mixture pressure must be equal. The physical meaning is the following. All the material lying above the contact discontinuity (closest to shock wave 4) has been influenced only by shock wave (4); all the material lying below has been subjected to shock waves (1), (2) and (3). This contact discontinuity plays an important role in the examples to follow.

(text continues on page 29)

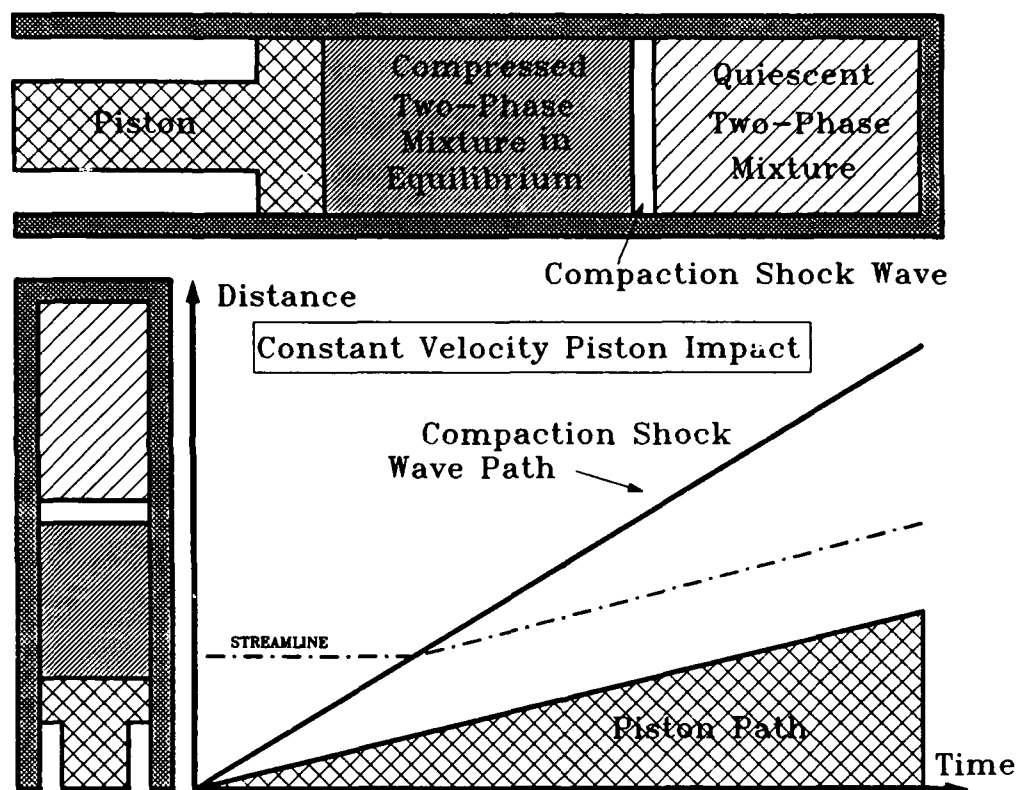


Figure 11 - Distance-time plot of constant-velocity-piston impact on a quiescent inert rate-independent medium. Note analogy with steady two-dimensional supersonic flow over a wedge.

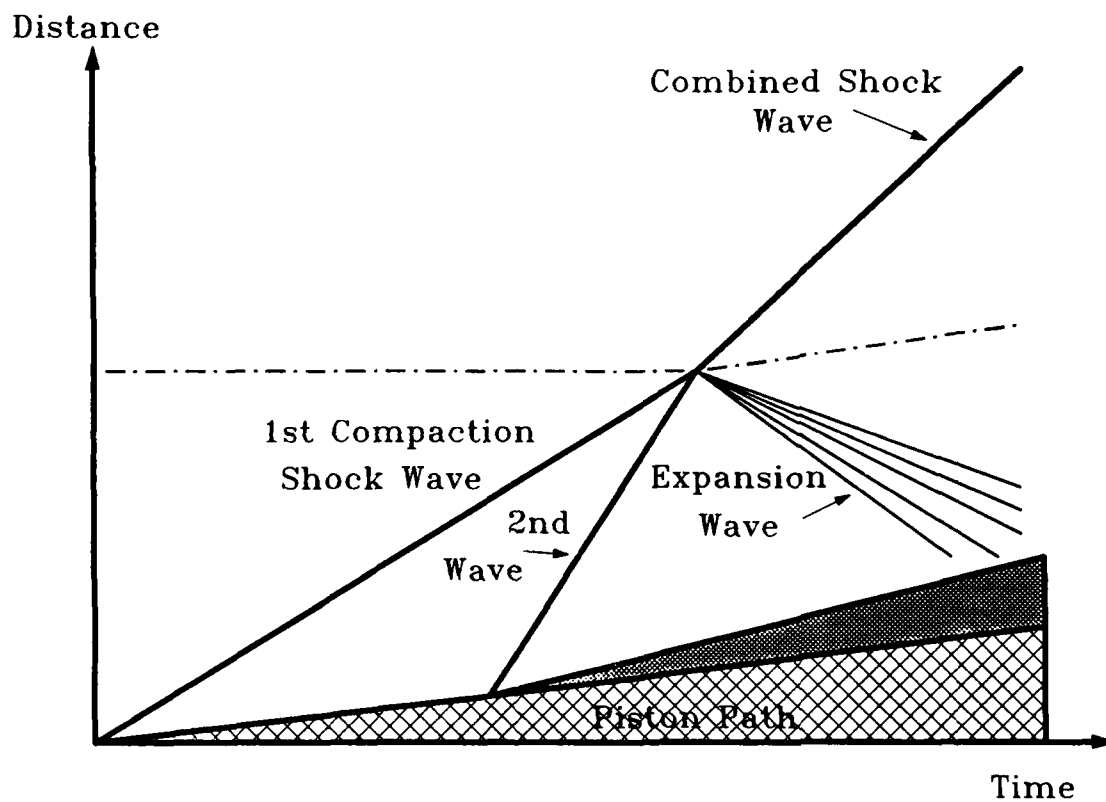


Figure 12 - Distance-time plot of double impact of piston (two abrupt changes to constant velocity) on a quiescent inert rate-independent medium. Note analogy with steady supersonic flow over a double wedge.

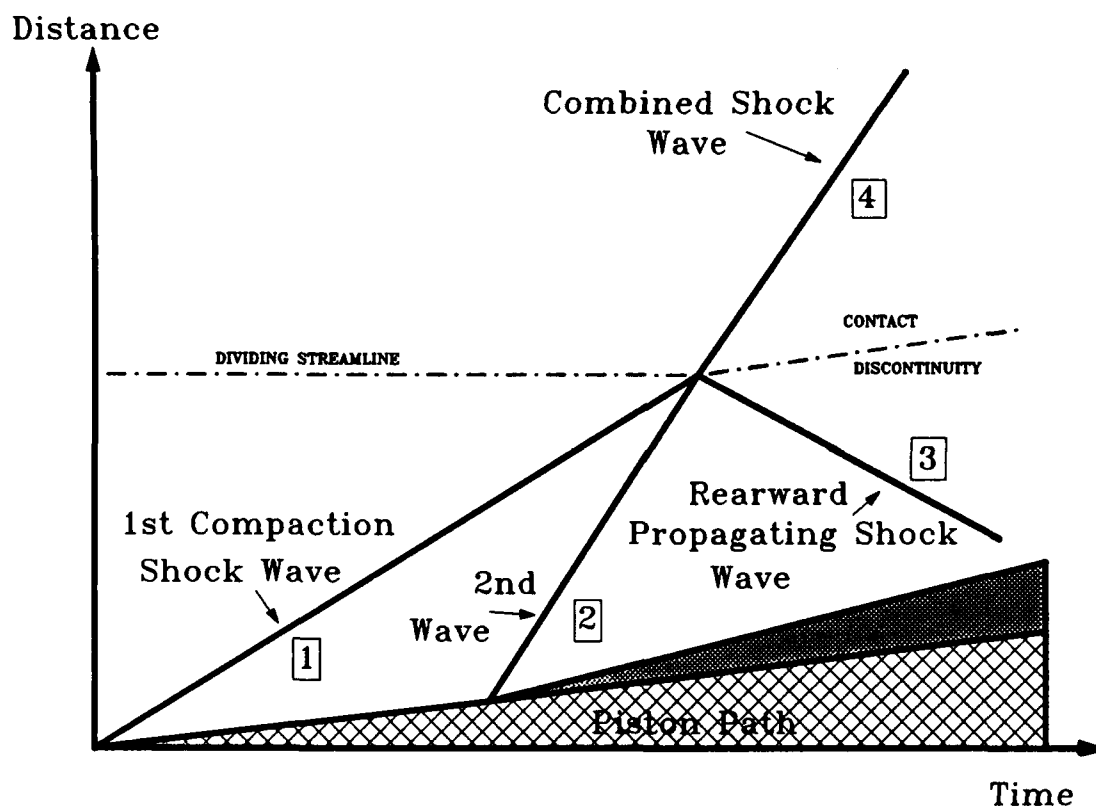


Figure 13 - Possible distance-time plot of double piston impact on quiescent rate-independent reactive medium.

The problem to be solved is that posed in Fig. 13. Both piston velocities are assumed constant. Since all rate processes have been removed from the equation system, each shock wave is quasi-steady and travels at a constant velocity. Thus the solution can be found from a system of coupled "jump condition" equations which are listed in Ref. 35 along with a description of the solution procedure. These equations are based on the same set of assumptions as the equilibrium shock wave theory of Section IV and will not be repeated here. Note again that the analysis cannot predict the amount of reactivity, η , in the wave-induced reaction; this value must be deduced from comparison to experimental wave patterns. In some examples, it will be assumed that the shock-induced reaction releases the total heat of reaction of the energetic solid. However, in single- and double-base propellants, the available evidence suggests that only a fraction of the total heat of combustion is released in this reaction (see discussion below).

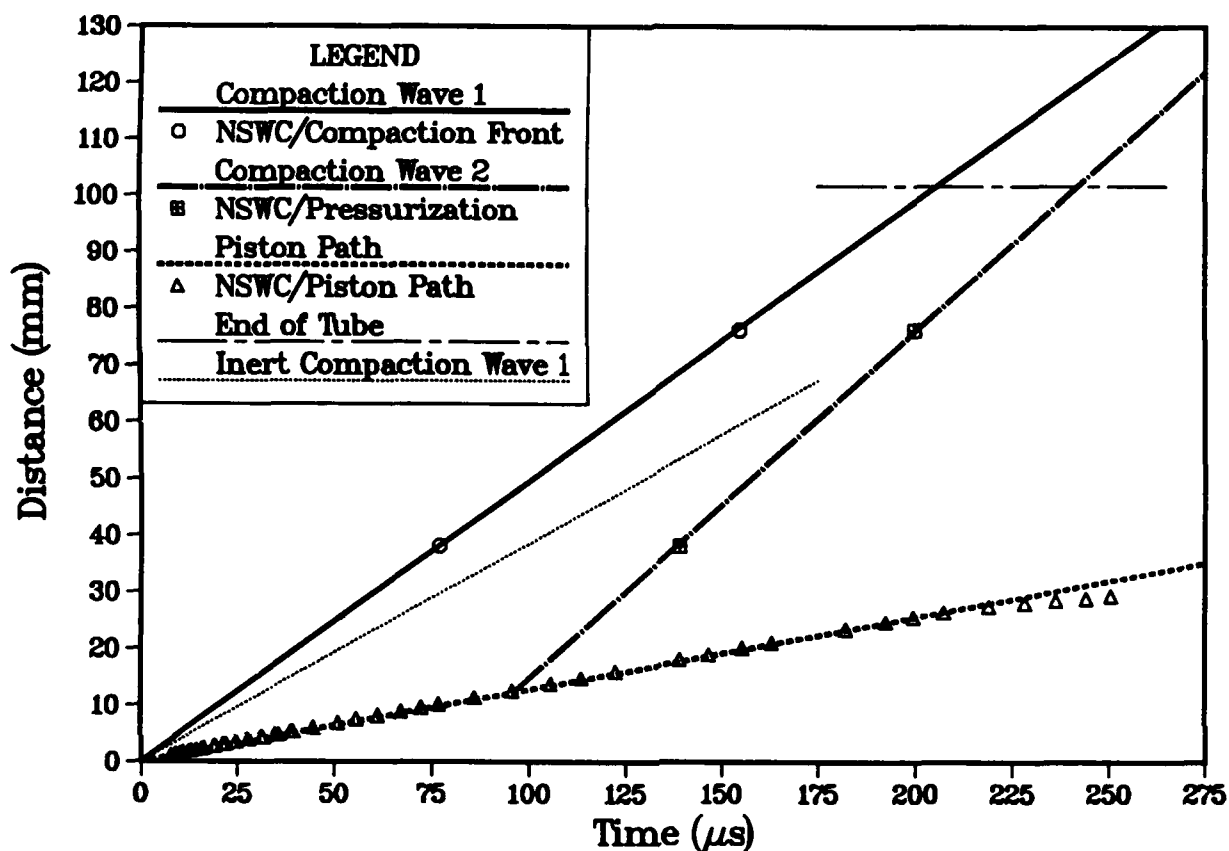
B. Results

This analysis will be used to interpret data from Sandusky's [14,15] PDC experiment, a combustion-driven piston experiment of McAfee [10,11], and a DDT experiment reported by Bernecker [8]. Granular materials include two double-base ball propellants (WC-231 and TS-3659) as well as Class D HMX. Values of the modeling parameters used to define the quasi-static stress state, total energy release, properties of the gas-phase combustion products, etc., for these materials can be found in Refs. 34a and 35b.

PDC-80 / 60.2% TMD TS-3659 Ball Propellant

TS-3659 is a double base ball propellant (nominally 21.6% NG in NC) with essentially spherical grains (434 μm diameter). The PDC experiment [15] denoted PDC-80 involved a 160 m/s impact on 60.2% TMD propellant confined in the aluminum tube, 101.7 mm long. Although later runs in this series made use of microwave interferometry to track motion of the strong compaction front, PDC-80 relied on two wall-mounted pressure transducers located at 38.1 and 76.2 mm from the impacted end. The time at which the compaction front passes the gage location is determined as the midpoint of the initial pressure rise. Each transducer record is also used to estimate the time for the "onset" of significant pressurization, which is somewhat subjective but not unreasonable. These data appear in Fig. 14 along with the location of the projectile face after impact; particle velocity is nearly constant at 127 m/s before a deceleration begins beyond 200 μs (presumably due to vigorous combustion). By this time, however, the leading compaction front has reached the downstream end of the tube. Although the tube eventually ruptured, there was no transition to detonation.

Predictions from the model are compared to the PDC data in Fig. 14. There are two observations here which seem to have general applicability. The first concerns the under-prediction of propagation speed of the leading compaction front. The PDC data imply a wave speed of 494 m/s, but present theory predicts 385 m/s for an inert wave in which the aggregate maintains the equilibrium stress state. However, if this compaction wave induces reaction accompanied by full heat release (1104 cal/g for TS-3659), then conversion of only 0.44% of the solid would create enough gas pressure to stiffen the aggregate and allow it to support the wave speed of 494 m/s. The magnitude of gas pressure required to support the increased wave speed is nearly independent of an important ambiguity concerning the amount of energy released in the wave-induced reaction. Reaction-generated



PARTIAL ENERGY RELEASE (304 cal/g)							
Shock	$\eta(\%)$	$V_s(\text{mm}/\mu\text{s})$	$P_m(\text{MPa})$	$P_g(\text{MPa})$	ϵ_s	$\rho_m(\text{g/cc})$	ρ_m/ρ_{m0}
quiescent	0.0	0.0	0.10	0.10	0.60	.9844	1.0
wave 1	1.32	0.4947	61.93	36.82	0.787	1.324	1.345
wave 2	0.0	0.613	62.57	37.22	0.7887	1.327	1.348

Figure 14 - Distance-time data for PDC-80; 160 m/s impact on 60.2% TMD TS-3659 propellant. Data from Ref. 15. Tabular values are model predictions downstream of indicated wave.

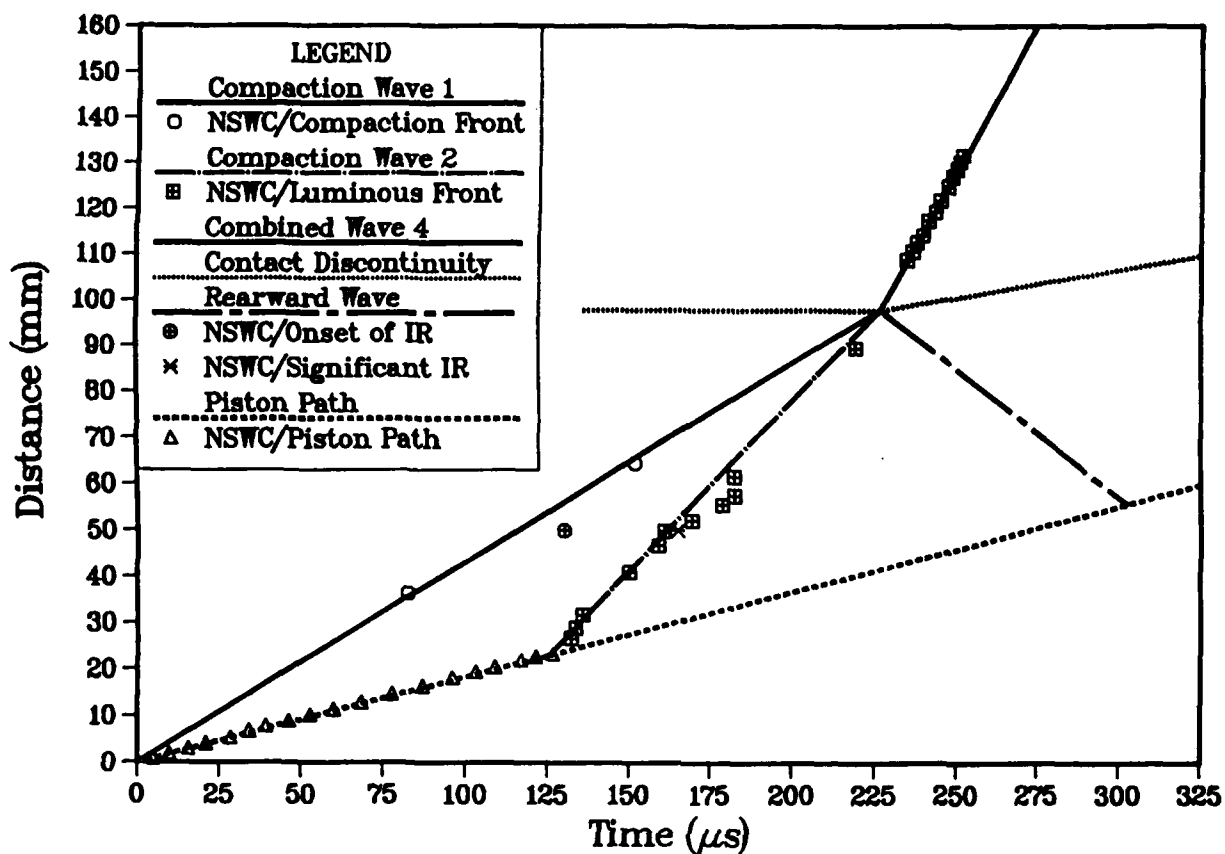
gas pressure is essentially a function of the product of the energy released and the amount of solid converted to gaseous products. Little evidence is available to determine the amount of energy release accompanying this reaction. However, liberation of the full heat of combustion of the solid phase means that the product gases trapped in the porosity of the aggregate will be near the equilibrium flame temperature (except for minute amounts of reaction). Unless the aggregate has been compressed above 90% TMD, confined gases at these temperatures should produce visible radiation which could be seen by a high-speed camera looking through a Lexan tube confinement. For TS-3659 propellant, Glancy et al. [15] attempted three such runs at impact speeds up to 290 m/s and failed to see any evidence of light on the camera records, although the tube ruptured. This observation implies that wave-induced reaction in TS-3659 releases only a fraction of the total energy, and this fraction is less than the value which would produce gas-phase temperatures of say 1500°K. As an example, the computational results in Fig. 14 show that a compaction wave speed of 494 m/s could be supported by reaction of 1.32% releasing only 304 cal/g (27.5% of the total) which leads to a gas temperature of 1243°K.

The second observation concerns the implied propagation speed and strength of the second compression wave. Differencing the two data points determined from the transducer records as the "onset" of significant pressurization (see Fig. 14) produces a wave speed of 624 m/s. If, in the model, the piston velocity is assumed to increase by 1 m/s at 95 μ s, this anchors a very weak "shock" wave which propagates into the aggregate at 613 m/s virtually passing through the data points. The implication is that the leading edge of the pressurization wave propagates near the local sound speed in the compressed material. Since the transducers testify to a rapidly rising pressure field downstream of wave (2), the quasi-steady assumption in the model breaks down in this important region. Thus the single weak wave (2) shown in Fig. 14 does not properly represent the influence of vigorous combustion which begins near the piston face. Successive pressure increases generated by transient combustion behind wave (2) will propagate at increasing speeds toward the collision point, and their coalescence may influence the "trigger" mechanism.

PDC-73 / 49.4% TMD WC-231 Propellant

WC-231 is a double-base ball propellant (nominally 25% NG in NC) whose grains are shaped like "fat pancakes" (spheres which have been rolled) with an average diameter of 790 μ m. In PDC-73 [15], 49.4% TMD WC-231 is confined in a Lexan tube and impacted at a projectile speed of 220 m/s. Transition to detonation did not occur within the experimental tube length (146 mm).

A simulation is shown in Fig. 15 along with the PDC data [15]. If the piston velocity is equated to the measured particle velocity of 183 m/s, the model predicts the leading compaction front (if inert) would propagate at 390 m/s; the PDC data imply approximately 430 m/s. If wave-induced reaction releases the full heat of combustion (1150 cal/g, assumed), then reaction of only 0.22% of the solid would support the observed wave speed. The luminosity data suggest that vigorous reaction begins near the piston face at approximately 125 μ s. Assuming a 1 m/s increase in piston velocity at this time generates a weak shock wave propagating at 736 m/s which forms a boundary for the leading edge of luminosity. Although overly simplistic, if collision of this second shock wave with the leading compaction front were to trigger about 5% reaction, the combined shock wave would propagate at 1.31 km/s and pass through the experimental data for strong luminosity. The



Shock	$\eta(\%)$	$V_s(\text{mm}/\mu\text{s})$	$P_m(\text{MPa})$	$P_g(\text{MPa})$	ϵ_s	$\rho_m(\text{g/cc})$	ρ_m/ρ_{mo}
quiescent	0.0	0.0	0.10	0.10	0.50	.8205	1.0
wave 1	0.22	0.4309	64.79	33.97	0.859	1.426	1.738
wave 2	0.0	0.735	65.58	34.42	0.8604	1.429	1.741
wave 4	5.2	1.309	131.1	131.0	0.5095	.9049	1.103
wave 3	0.0	-0.557	131.1	77.46	0.9288	1.559	1.900

PARTIAL ENERGY RELEASE (250 cal/g)

wave 1	0.80	0.4313	64.85	35.32	0.853	1.425	1.737
wave 2	0.0	0.738	65.65	35.79	0.855	1.428	1.740

Figure 15 - Distance-time data for PDC-73; 220 m/s impact on 49.4% TMD WC-231 propellant. Data from Ref. 15. Tabular values are model predictions downstream of indicated wave.

predicted magnitude of reaction to drive the combined shock wave is plausible, but it is unlikely that collision of the postulated weak second shock wave with the leading wave could be the sole trigger for the increase in reactivity; transient combustion behind the second wave must play a role. The fact that luminosity was not observed directly behind the leading front again suggests partial energy release in the wave-induced reaction. If it is assumed that only 250 cal/g are liberated by reaction of 0.8% of the solid, the wave pattern in Fig. 15 is unchanged except that the temperature of the trapped gases reaches only 1205°K. In both simulations of PDC-73, the leading edge of luminosity propagates at the local sound speed in the aggregate just as the onset of pressurization did in PDC-80.

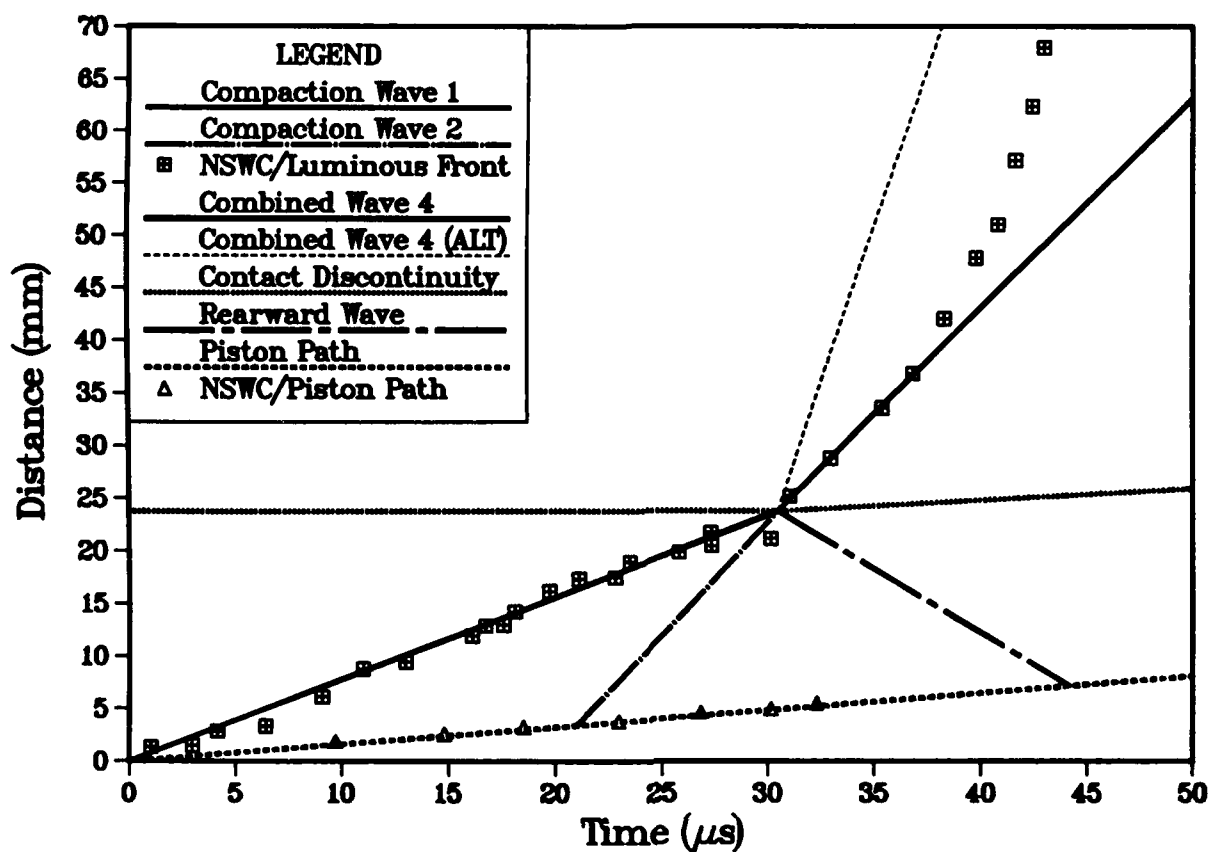
Partial confirmation of the reactive wave assumption in the present model may be provided by an experimental measurement [15] unique to PDC-73. This run included two infrared detectors which observed the aggregate through a NaCl window aperture (50 mm from the impacted end) in the wall of the Lexan tube. Although the IR signals were not calibrated for absolute temperature, their ratio indicates relative temperature [15]. First response from the two detectors occurred at 121 and 127 μ s, while the maximum ratio (maximum temperature) occurred at 130 μ s; arrival time of the leading compaction wave is predicted to be 117 μ s. This strongly suggests that the compaction wave itself initiated reaction. Just behind the wave representing the leading edge of luminosity, the IR signals indicate a broad-based participation in reaction but temperatures remain below the previous maximum until after the appearance of the brightly luminous front which coincides with the combined shock wave in the present model.

PDC-27 / 73% TMD Class D HMX

Simulations of impact on Class D HMX are clouded by the influence of particle size distribution, which introduces a variability in quasi-static compaction behavior [38] and hence wave propagation speed in the present study. But a simulation of one of Sandusky's PDC runs will be used here to illustrate some consequences of the multiple wave structure. PDC-27 [14] involved Class D HMX loaded at 73% TMD into a 147 mm long Lexan tube and impacted at 267 m/s; a transition to detonation did take place as indicated in Fig. 16. Since luminosity is coincident with the leading compaction front, the simulation of wave-induced reaction assumed total energy release and found that reaction of approximately 0.5% is required to support the observed wave speed of 778 m/s. If collision triggers reaction of 3.2%, the combined shock wave will be driven at 2 km/s and pass through the next four data points for strong luminosity. In this run, the wave continues to accelerate and quickly achieves the detonation velocity of 7.46 km/s.

Up to this point, the role played by the rearward propagating shock wave (3) and the contact discontinuity between waves (3) & (4) has been rather obscure. This study would contend, however, that the density differences bounded by these waves should be clearly discernable in a radiograph. Fig. 17 is a plot of the spatial distribution of mixture density (ratioed to initial mixture density) at 35 μ s, derived from the computed flow field for PDC-27 shown in Fig. 16. It simulates what a flash radiograph would record if triggered (at 35 μ s) shortly after the collision. There are several interesting features here. Density of the reacting mixture directly behind the combined shock wave (4) traveling at 2 km/s is not much greater than the quiescent value. Even though this reacting mixture is supporting a stress of 300 MPa, the solid volume fraction is virtually unchanged because the high pressure gas-phase combustion products can carry the same "load"

(text continues on page 38)



Shock	$\eta(\%)$	$V_s(\text{mm}/\mu\text{s})$	$P_m(\text{MPa})$	$P_g(\text{MPa})$	ϵ_s	$\rho_m(\text{g/cc})$	ρ_m/ρ_{m0}
quiescent	0.0	0.0	0.1	0.1	0.73	1.389	1.0
wave 1	0.46	0.7786	174.2	143.1	0.9067	1.752	1.261
wave 2	0.009	2.143	177.7	146.5	0.9068	1.753	1.261
wave 4	3.2	2.019	305.6	305.5	0.7327	1.469	1.057
wave 3	0.0	-1.213	305.6	237.7	0.9364	1.823	1.312

ALTERED PDC-27							
wave 4	5.87	6.01	477.3	477.3	0.6737	1.403	1.009
wave 3	0.0	-1.469	477.3	358.1	0.9533	1.873	1.348

Figure 16 - Distance-time data for PDC-27; 267 m/s impact on 73% TMD Class D HMX. Data from Ref. 14. Tabular values are model predictions downstream of indicated wave.

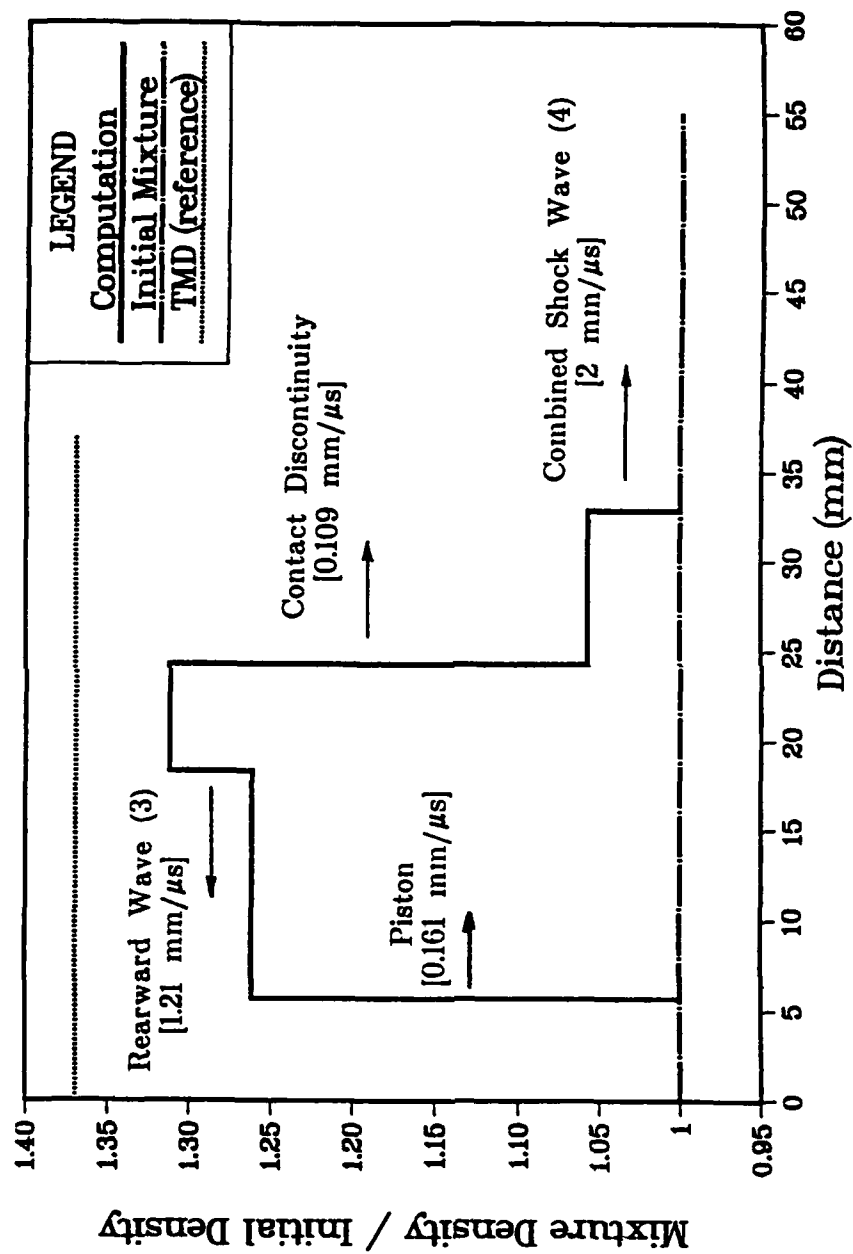


Figure 17 - Simulated radiograph triggered at 35 μ s in PDC-27. Numerical values from model predictions listed in Figure 16.

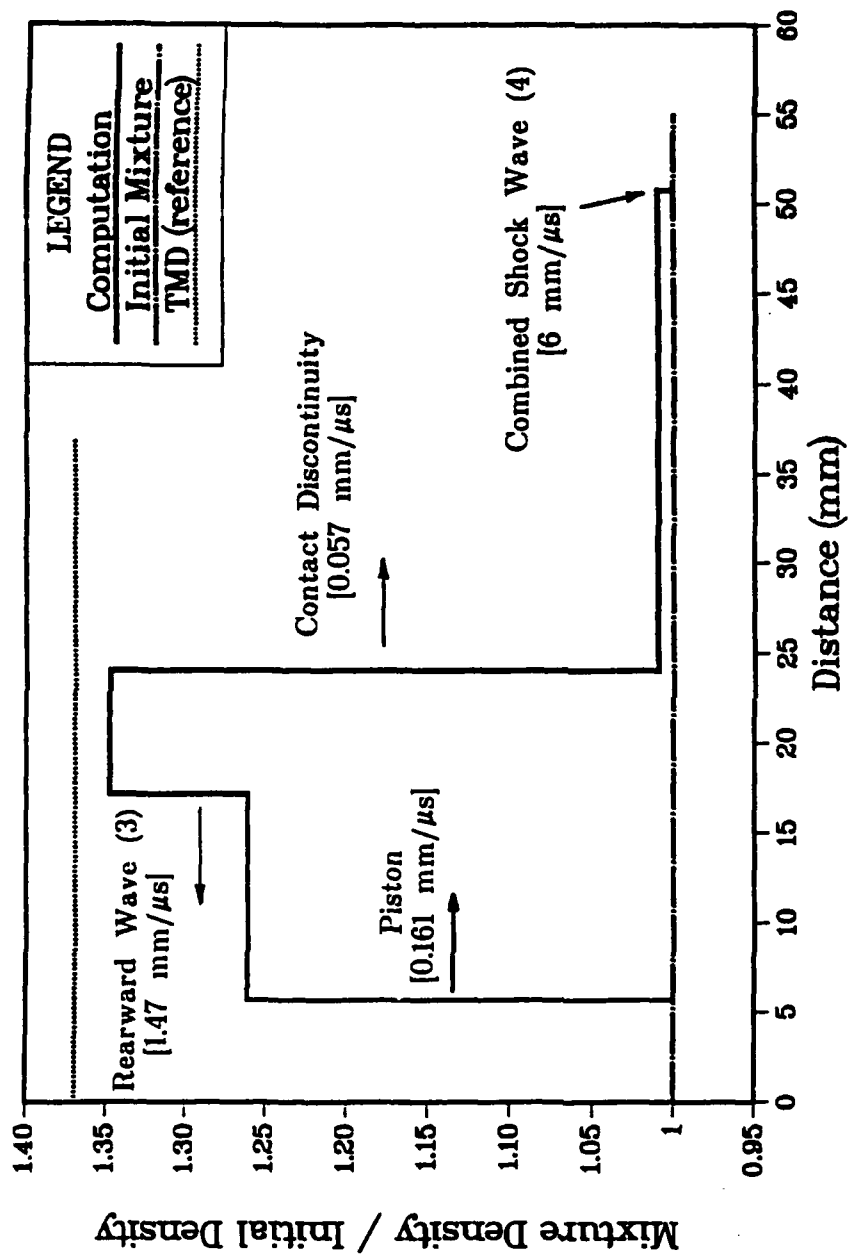
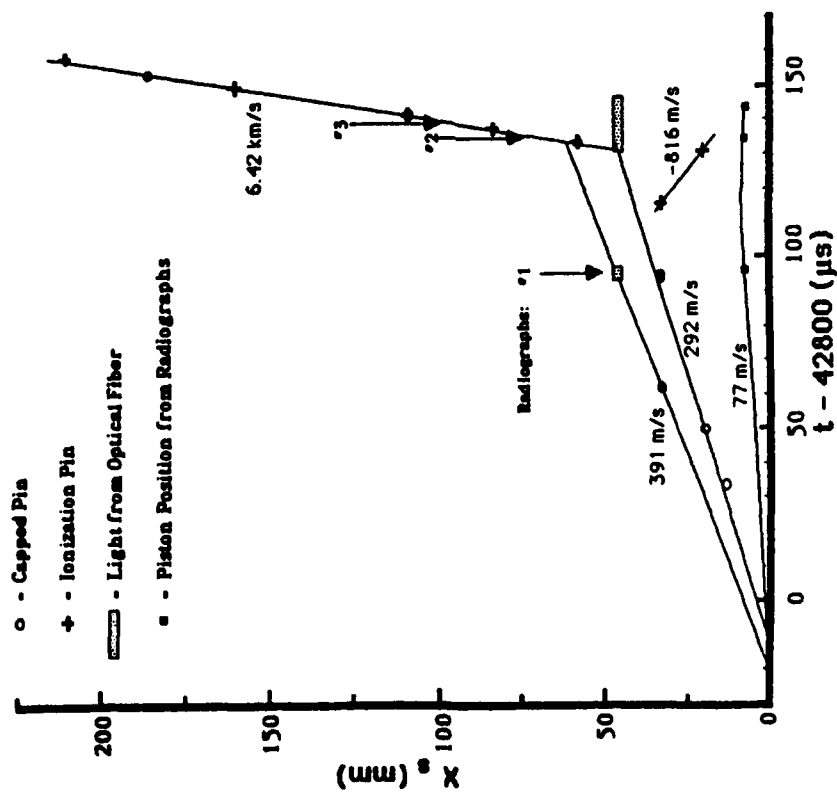
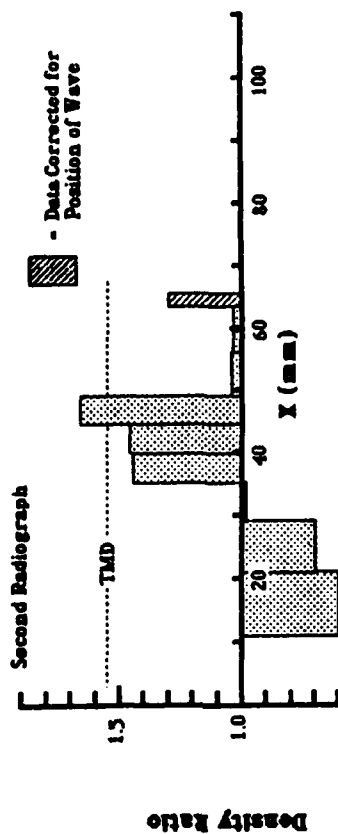


Figure 18 - Simulated radiograph triggered at 35 μ s in ALTERED PDC-27. Numerical values from model predictions listed in Figure 16.



(a) Distance-time data / Run B-9153



(b) Radiograph #2 / Run B-9153

Figure 19 - Data from LANL combustion-driven-piston experiment with 64% TMD
Class A HMX. Figures courtesy of McAfee et. al. [10,11]

as the solid material. The high density region ("plug") is material trapped behind the slow moving contact discontinuity. The highest density represents material which has been compressed by shock waves (1), (2) & (3). The "reverse step" in density is created by shock wave (3) which is propagating rearward into material already subjected to (1) & (2). This density pattern is accentuated when the collision triggers an increased level of reaction in the combined shock wave (4). For demonstration purposes, the flow field for PDC-27 was altered by increasing the amount of reaction assumed to be triggered by the collision. Although shock waves (1) & (2) remain unchanged, the case labelled ALTERED PDC-27 (see table under Fig. 16) predicts a combined shock wave (4) propagating at 6 km/s. The corresponding simulated radiograph at 35 μ s is shown in Fig. 18. Note that mixture density behind shock wave (4) is now virtually equal to the quiescent value. The highest density in the "plug" has increased, the velocity of the leading edge (contact discontinuity) of the "plug" has slowed to less than 100 m/s, and the reverse step is more pronounced because the rearward propagating shock wave (3) is stronger.

PDC-27 did not happen to include flash radiography, but it may be appropriate to compare the above prediction to a result obtained by McAfee [10,11] in 64% TMD Class A HMX. In McAfee's experiment, combustion of ignitor material at one end in a closed tube creates a rising pressure field against a steel cylinder or "piston" which is then driven into the confined Class A HMX. Confinement is a fairly thin-walled maraging steel tube which allows flash radiography to record the position of tracer foils seeded into the original bed; diagnostics also include capped and ionization pins. The X-T plot of McAfee's run B-9153 reproduced here as Fig. 19a shows that a transition to detonation (6.42 km/s) did occur. Radiograph #2 was taken just after the transition, and the results are reproduced in Fig. 19b. Some striking similarities are evident when comparing this experimental result with the simulated radiograph in Fig. 18 for the 6 km/s combined shock wave (4). If it can be assumed, in McAfee's experiment, that a shock wave collision triggered an abrupt increase in wave-induced reaction, then the present model predictions would appear to be compatible with his observations.

DDT SHOT A266 / 59.8% TMD TS-3659

At the present time, none of the impact experiments have produced pressure transducer records which offer conclusive evidence for the presence of the rearward propagating wave. Such evidence is provided by a DDT experiment. Bernecker [8] has reported results for 59.8% TMD TS-3659 confined in the thick wall steel tube which was instrumented with a series of ionization pins as well as several wall-mounted transducers [8]. The arrival time of the strong reaction front can be extracted from the pin data, but the transducers continue to record a time-history after the front has passed. The results [8] from Shot A266 are reproduced here in Fig. 20, in terms of x^* and t^* which are distance and time referenced to the onset of detonation. The acceleration of the strong compaction front from 620 m/s to 2.15 km/s is accompanied by a rearward propagating compression wave (speed of ~ 1.7 km/s) as indicated by the transducer excursions at symbols D, E, F & G.

The present theory based on simple motion of a piston driver is ill-equipped to simulate a DDT experiment which begins with ignitor combustion. In particular, no experimental value of particle velocity is available to determine the motion of a hypothetical "piston". A simulation was based on a 230 m/s particle

velocity and 0.29% reaction to create the strong compaction front at 630 m/s, a 45 μ s time delay, and then a 1 m/s increase in particle velocity to anchor the second wave. Although clearly not unique, this wave structure predicts that a collision which triggers $\sim 10\%$ reaction would produce a combined shock wave (4) traveling at 2.15 km/s. Furthermore, a rearward propagating shock wave (3) will travel at 1.72 km/s if it induces an additional 0.72% reaction in the already burning material compressed by waves (1) & (2). The path of both these waves lies parallel to the experimental data. Comparison of the transducer time-history to the predicted pressure level of 350 MPa behind shock wave (3) indicates that theory is low by approximately a factor of two, which may not be surprising when considering the assumptions which have been made. Although the analysis suggests that the rearward wave was triggered by a collision, this computational example does not constitute proof.

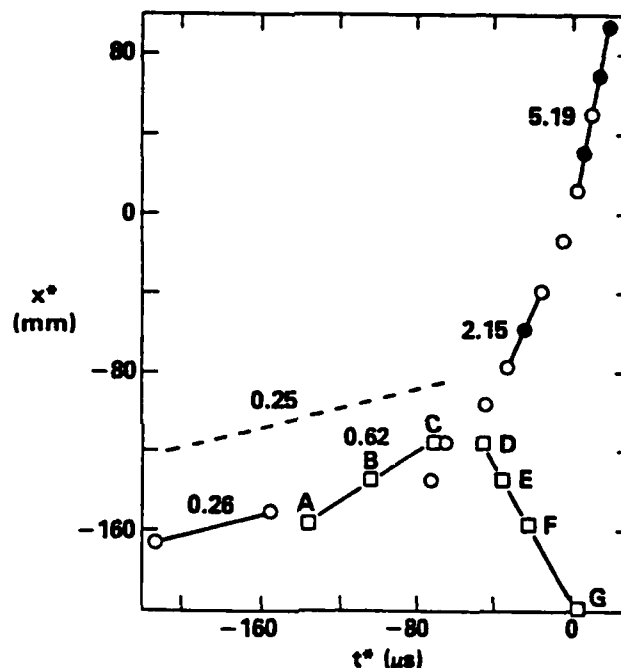


Figure 20 - Relative distance-time data from Bernecker's [8] DDT Shot A266 using 59.8% TMD TS-3659 ball propellant (circles = probe response, squares = transducer excursion; velocity in mm/ μ s).

To summarize this section, various laboratory experiments on SDT and DDT in granular energetic material have observed abrupt increases in the speed of propagation of compaction waves and the leading edge of luminosity. The DDT experiment, in at least one case, has evidence of a strong rearward propagating wave. A possible explanation is provided by a simple quasi-steady model which envisions an increase in reactivity triggered by the collision of two reactive compaction/shock waves. Simulation of experimental data shows that:

(a) The leading compaction wave created by modest impact on confined granular energetic material is not necessarily inert. The experimental propagation speeds which exceed the predicted inert wave speed could be supported by wave-induced reaction of a few tenths of one percent of the solid material, if the

reaction releases the total heat of combustion. If wave-induced reaction is accompanied by partial heat release (highly probable for single and double base propellants), then the magnitude of reactivity is near one percent.

(b) After a time delay, the onset of vigorous combustion of material adjacent to the piston face will drive a second compressive wave system into the aggregate which has been formed by the initial compaction wave. The leading edge of this second wave system propagates at a speed near the local sound velocity.

(c) The analysis predicts that the abrupt increases in propagation speed observed experimentally would require the collision to induce reaction in the range of 2% - 10%. Transient combustion (neglected in this model) behind the leading edge of the secondary wave system must play a role in the "trigger" mechanism.

(d) The wave pattern produced by the collision includes both a combined compaction/shock wave exhibiting an abrupt increase in speed, and a rearward wave which propagates back into material compressed by the first two waves. A simulated radiograph taken shortly after the collision predicts:

(1) The density behind the combined shock wave may appear nearly equal to the quiescent value. Wave-induced reaction generates enough gas pressure to counteract (resist) the normal occurrence of bed compaction caused by a large value of mixture stress.

(2) A high density ("plug") region is trapped behind the slow-moving contact discontinuity.

(3) The spatial distribution of the high density region will exhibit a "reverse step" as a direct result of the rearward propagating shock wave.

It appears from these simulations that the appearance of a rearward propagating wave may be a direct indicator that a "trigger" mechanism is responsible for the abrupt increase in wave speed. The lack of any rearward propagating wave may signify that the transition mechanism is controlled by nearly complete combustion which "drives" from behind until it catches the leading compaction front, which is essentially the mechanism deduced fifteen years ago by Bernecker & Price [4].

VI. TRANSIENT REACTIVE SHOCK WAVE MODEL [36]

A basic objective here is to create a more realistic description of the transient events seen in the PDC experiment by removing many of the restrictive assumptions adopted in the previous three models. This one-dimensional model is designed to simulate the configuration shown in Fig. 1. As before, the mixture of compressible granular solids and gas deforms in uniaxial strain. It is also assumed that the mixture responds to a change in density by instantaneously adjusting to the equilibrium stress state defined in Section II, i.e., rate-dependent resistance to porosity change is neglected. However, this model does account for

- (a) deviator stress components in the formulation of the mixture stress tensor,
- (b) a traction force (friction) between the sliding aggregate and the confining boundary,
- (c) a drag force between the gas and solid particles (gas and solid phases have different velocities),
- (d) heat transfer between the two phases,
- (e) ignition and transient combustion of the solid phase, and
- (f) reaction of a gas-phase intermediate species to a final combustion product.

Although the impact-generated compaction wave is modeled as a shock wave, no propagation speed is constrained to be quasi-steady. Combustion-generated compression wave systems can appear at any time in the transient flow field.

The conversion of energetic solid material to final gaseous combustion products is a complex process which is not well understood. Although solid propellant combustion can often be represented with a pressure-dependent prescription for surface regression rate, this implicitly assumes that the gas-phase flame zone is quasi-steady and remains anchored to the interface. Considerable additional detail is required for a description of ignition and the transient events leading up to an "established" flame zone near the solid surface. Even if the complete decomposition scheme and associated multi-species reaction parameters were known, this level of detail is far beyond the scope of the present effort. A first step, however, is the simple two species reaction scheme sketched in Fig. 21. It is assumed that " R_1 " is a reactive intermediate gas-phase species which is the result of a partial or incomplete decomposition of the energetic solid. Then, " R_1 " will liberate the remaining energy in a gas-phase reaction to form " R_2 ", the final flame product. The present model envisions a staged combustion process which changes at a "transition" value of gas pressure defined as P_{tr} (assumed constant here). When the local gas pressure is less than P_{tr} , solid-phase decomposition is incomplete and releases the reactive intermediate species R_1 into the surrounding gas mixture. When the local gas pressure exceeds P_{tr} , solid-phase decomposition goes to completion and releases the final product gas R_2 . The gas-phase reaction which converts R_1 to R_2 can occur at any time or location. The precedent for such a scheme can be found in the two-stage flame zone of a double-base propellant, and in the ignition and flame spreading problems [51] observed with certain LOVA nitramine propellants used in guns. Price et. al. [23,24] have been pursuing similar ideas for several years.

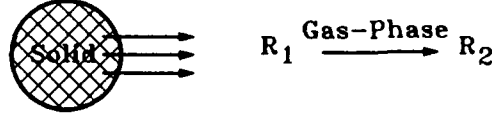
REACTION / COMBUSTION SCHEME

R_1 = Reactive Intermediate at Energy Level Δe_{gr}^0

R_2 = Final Combustion Product at Energy Level e_g^0

In Gas Phase: $R_1 \rightarrow R_2$

For Gas Pressure < Transition Pressure:



For Gas Pressure > Transition Pressure:

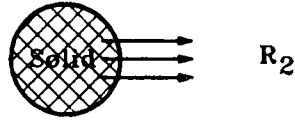


Figure 21 - Schematic of combustion process in model.

The model reaction scheme is an extreme simplification, but it may be useful in demonstrating potential interactions. The impact-generated compaction wave begins the process by inducing reaction of a small amount of energetic solid within the wave front itself (see discussion in Section IV). It is assumed that this wave-induced reaction produces the reactive intermediate gas species, R_1 , which is trapped in the porosity of the compressed aggregate. This trapped gas must wait through an induction time or delay time, t_{del} , before the reaction which converts R_1 to R_2 can begin; the idea of a delay time was taken from the work of Baer and Nunziato [20]. Once the gas-phase reaction is underway, the pressure and temperature of the gas-phase mixture will increase. This increases the heat transfer rate to the solid phase, which raises the solid-phase surface temperature (predicted with the scheme devised by Baer [48]). Solid-phase combustion begins when the computed surface temperature exceeds an ignition value (typically, 473°K here). Combustion of the solid phase proceeds at a prescribed pressure-dependent rate producing intermediate species R_1 when $P_g < P_{tr}$ and then R_2 above the transition pressure. Given an initial value of delay time, t_{del}^0 , the local value follows from a solution of,

$$D(t_{del})/Dt_g = -(P_g/P_g^0)^2. \quad (15)$$

The global gas-phase reaction, $R_1 \rightarrow R_2$, proceeds at the finite rate, \dot{m}_{gr} , where

$$\begin{aligned} \text{for } t_{del} > 0.0 \quad \dot{m}_{gr} &= 0.0 \\ \text{for } t_{del} < 0.0 \quad \dot{m}_{gr} &= A_{gr} Y_1 \rho_g \exp(-E_{gr} / T_g) \end{aligned} \quad (16)$$

Since this is not an elementary reaction, the rate parameters A_{gr} and E_{gr} must be estimated. Keeping in mind that the mass generation rate, \dot{m} , from solid-phase combustion/pyrolysis produces R_1 when $P_g < P_{tr}$ and R_2 otherwise, the time rate-of-change of Y_1 can be written,

$$D(Y_1)/Dt_g = [\dot{m}(\text{when } P_g < P_{tr}) - \dot{m}_{gr} - Y_1 \dot{m}] \quad \text{for } t_{del} < 0.0 \quad (17)$$

where the first term on the RHS vanishes when the solid combustion process goes directly to completion ($P_g > P_{tr}$).

The balance equations are written in a translating coordinate system where

$$V_c = V_c(t) = \text{local velocity of axial coordinate.}$$

Relative velocities for each phase are then

and $U_s = u_s - V_c = \text{solid-phase velocity relative to local coordinate system,}$

$U_g = u_g - V_c = \text{gas-phase velocity relative to local coordinate system.}$

Balance of Mass / Solid Phase:

$$\varepsilon_s \left(\frac{D \rho_s}{D t_s} \right) + \hat{\rho}_s u_{sz} + \rho_s \left(\frac{D \varepsilon_s}{D t_s} \right) = - \dot{m} \quad (18)$$

Balance of Mass / Gas Phase:

$$\varepsilon_g \left(\frac{D \rho_g}{D t_g} \right) + \hat{\rho}_g u_{gz} - \rho_g \left(\frac{D \varepsilon_s}{D t_g} \right) = + \dot{m} \quad (19)$$

Balance of Momentum / Solid Phase:

$$\hat{\rho}_s \left(\frac{D u_s}{D t_s} \right) + \varepsilon_s \sigma_{sz} + \beta_s \varepsilon_{sz} = f_d - f_w \quad (20)$$

Balance of Momentum / Gas Phase:

$$\hat{\rho}_g \left(\frac{D u_g}{D t_g} \right) + \varepsilon_g P_{gz} = - f_d - \dot{m} (u_g - u_s) \quad (21)$$

Balance of Energy / Solid Phase:

$$\hat{\rho}_s \left(\frac{D e_s}{D t_s} \right) + \varepsilon_s \sigma_s u_{sz} + (\sigma_s - \beta_s) \left(\frac{D \varepsilon_s}{D t_s} \right) = q - (\sigma_s - \beta_s) \frac{\dot{m}}{\rho_s} \quad (22)$$

Balance of Energy / Gas Phase:

$$\begin{aligned} \hat{\rho}_g \left(\frac{D e_g}{D t_g} \right) + \varepsilon_g P_g u_{gz} - P_g \left(\frac{D \varepsilon_s}{D t_g} \right) = \\ + f_d (u_g - u_s) - q + \dot{m} \left[(e_s - e_g) + \frac{(\sigma_s - \beta_s)}{\rho_s} + \frac{(u_s - u_g)^2}{2} \right] \end{aligned} \quad (23)$$

$$\text{where } \frac{D ()}{D t_s} \equiv ()_t + U_s ()_z \quad \frac{D ()}{D t_g} \equiv ()_t + U_g ()_z$$

The above equation system is incomplete without a relationship between porosity and the state of stress in the mixture; in the present analysis, this rate-independent relationship is denoted the "equilibrium stress state" and is described in Section II [see Eq. 8].

A deliberate attempt was made to preserve the integrity of the equation system by deriving a numerical solution procedure based on the method-of-characteristics (MOC). A MOC solution holds the promise of faithfully reproducing the local wave motion and propagating shock waves as discontinuities without spurious numerical distortion. The disadvantages include a complicated derivation and a non-trivial coding exercise to obtain the solution. These disadvantages are accentuated in two-phase flow. Single-phase flow yields three characteristic directions and their associated compatibility conditions, all of which can be solved explicitly although the procedure involves iteration. The current system of two-phase flow equations which are constrained to the equilibrium stress state is more difficult to solve. The system consists of a mass, momentum, and energy equation for each phase (Eqs. 18-23), along with a statement of the equilibrium stress state (Eq. 8).

Given:

$$\beta_s (\varepsilon_s) = \sigma_s - P_g ; \quad \sigma_s = P_s (\rho_s, e_s) / \psi (\varepsilon_s)$$

$$\beta_s' \equiv \frac{d}{d\varepsilon_s} \beta_s \quad ; \quad \psi' \equiv \frac{d}{d\varepsilon_s} \psi$$

Define:

$$\begin{aligned}
 a_g^2 &\equiv (P_g)_{\rho_g} + (P_g / \rho_g^2) (P_g)_{e_g} \\
 a_{1s}^2 &\equiv \left[(P_s)_{\rho_s} + (\sigma_s / \rho_s^2) (P_s)_{e_s} \right] / \psi \\
 A_{1s}^2 &\equiv a_{1s}^2 - (\beta_s / \psi \rho_s^2) (P_s)_{e_s} \\
 \alpha_g &\equiv \frac{\rho_g a_g^2}{\epsilon_g} ; \quad \alpha_{1s} \equiv \frac{\rho_s a_{1s}^2}{\epsilon_s} ; \quad \alpha_A \equiv \frac{\rho_s A_{1s}^2}{\epsilon_s} + \frac{\sigma_s \psi'}{\psi} \\
 C_{\tilde{x}} &\equiv (\alpha_A + \beta_s') / (\alpha_g + \alpha_A + \beta_s') \\
 C_{\tilde{y}} &\equiv [\alpha_g + \beta_s' + (\beta_s / \epsilon_s)] / (\alpha_g + \alpha_A + \beta_s') \\
 C_{\tilde{z}} &\equiv (\beta_s' + \beta_s / \epsilon_s) / (\alpha_g + \alpha_A + \beta_s')
 \end{aligned}$$

The six distinct characteristic directions follow from the roots of

$$W_s W_g \left(W_s^2 W_g^2 - C_{\tilde{x}} a_g^2 W_s^2 - C_{\tilde{y}} a_{1s}^2 W_g^2 + C_{\tilde{z}} a_g^2 a_{1s}^2 \right) = 0 \quad (24)$$

$$\text{where } W_s \equiv \frac{dz}{dt} - U_s ; \quad W_g \equiv \frac{dz}{dt} - U_g$$

The two trivial roots, $W_s = 0$ and $W_g = 0$, represent the respective streamlines. Unfortunately, the fourth-order expression in brackets does not factor explicitly, and the four "acoustic" directions,

$$W_s^+, W_s^-, W_g^+, W_g^-$$

are the four real roots which must be found numerically. The relationship of these roots is sketched in Fig. 22 below, where 7-1 represents the solid-phase streamline, 6-1 is the gas-phase streamline, 2-1 and 5-1 are the right-running and left-running solid-phase acoustic directions, respectively, and 3-1 and 4-1 are the right-running and left-running gas-phase acoustic directions, respectively. The compatibility conditions face a similar complication. Both energy equations can be written in characteristic form along their respective streamlines, i.e.,

$$\rho_s = \rho_s(\sigma_s) \quad \text{and} \quad \rho_g = \rho_g(P_g).$$

However, the remaining four dependent variables (u_s , u_g , σ_s and ϵ_s , here) are coupled in the matrix equation,

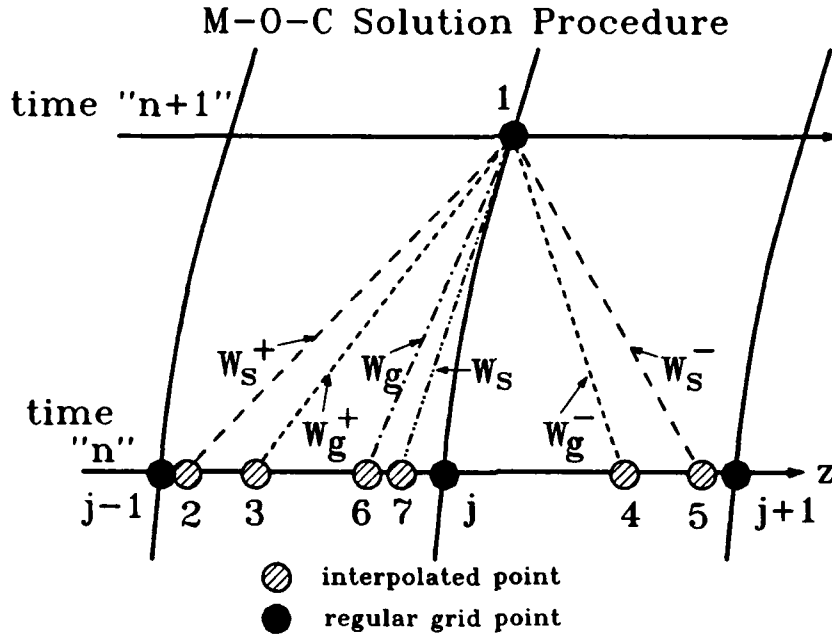


Figure 22 - Schematic representation of method-of-characteristics solution procedure.

$$F_s (W_g^2 - a_g^2) - F_g (W_s^2 - a_{ls}^2) = 0 \quad (25)$$

where

$$F_s \equiv \rho_s a_{ls}^2 (\dot{u}_s - H_{u_s}) + W_s \left[(\dot{\sigma}_s - H_{\sigma_s}) + \alpha_A (\dot{\epsilon}_s - H_{\epsilon_s}) \right]$$

$$F_g \equiv \rho_g a_g^2 (\dot{u}_g - H_{u_g}) + W_g \left[(\dot{\sigma}_s - H_{\sigma_s}) - (\alpha_g + \beta_s) (\dot{\epsilon}_s - H_{\epsilon_s}) \right]$$

$$\text{and} \quad (\dot{}) \equiv \frac{d}{dt} ()$$

With reference to Fig. 22, the solution is found in the following sequence. Using an estimate for all six characteristic directions, Eq. 25 is inverted to give values for u_s , u_g , σ_s and ϵ_s at the new point "1". The stress state equation immediately specifies P_g . The two energy equations yield the density values, and the equations of state provide the internal energies. Then, the characteristic directions must be re-solved (Eq. 24) and the whole process repeated until convergence is obtained. Although this procedure is somewhat involved, flow fields for the problems discussed below require only 1 to 2 minutes on the BRL Cray-2.

Within the constraints of the present review, it is not possible to include a discussion of all the computations made with this model. Instead, this section will focus on three important areas in the simulation of NSWC's PDC experiment: (A) the influence of the projectile path, (B) simulation accuracy when the granular material is inert, and (C) the influence of the energy release mechanism. In (B), the examples are based on PDC-M34 and PDC-74 which involve the inert material

melamine (46-56 μm diameter). In (A) and (C), the examples are based on the experimental runs PDC-80 and PDC-81, both of which involve Lexan projectile impact on approximately 60% TMD TS-3659 ball propellant (spherical grains, 434 μm diameter) which has a nominal composition of 21% NG in NC (estimated heat of explosion is 1104 cal/g). Additional details about the experiments can be found in Refs. 15 and 42; both PDC-80 and 81 were part of the JANNAF Modeling Workshop summarized in Ref. 32.

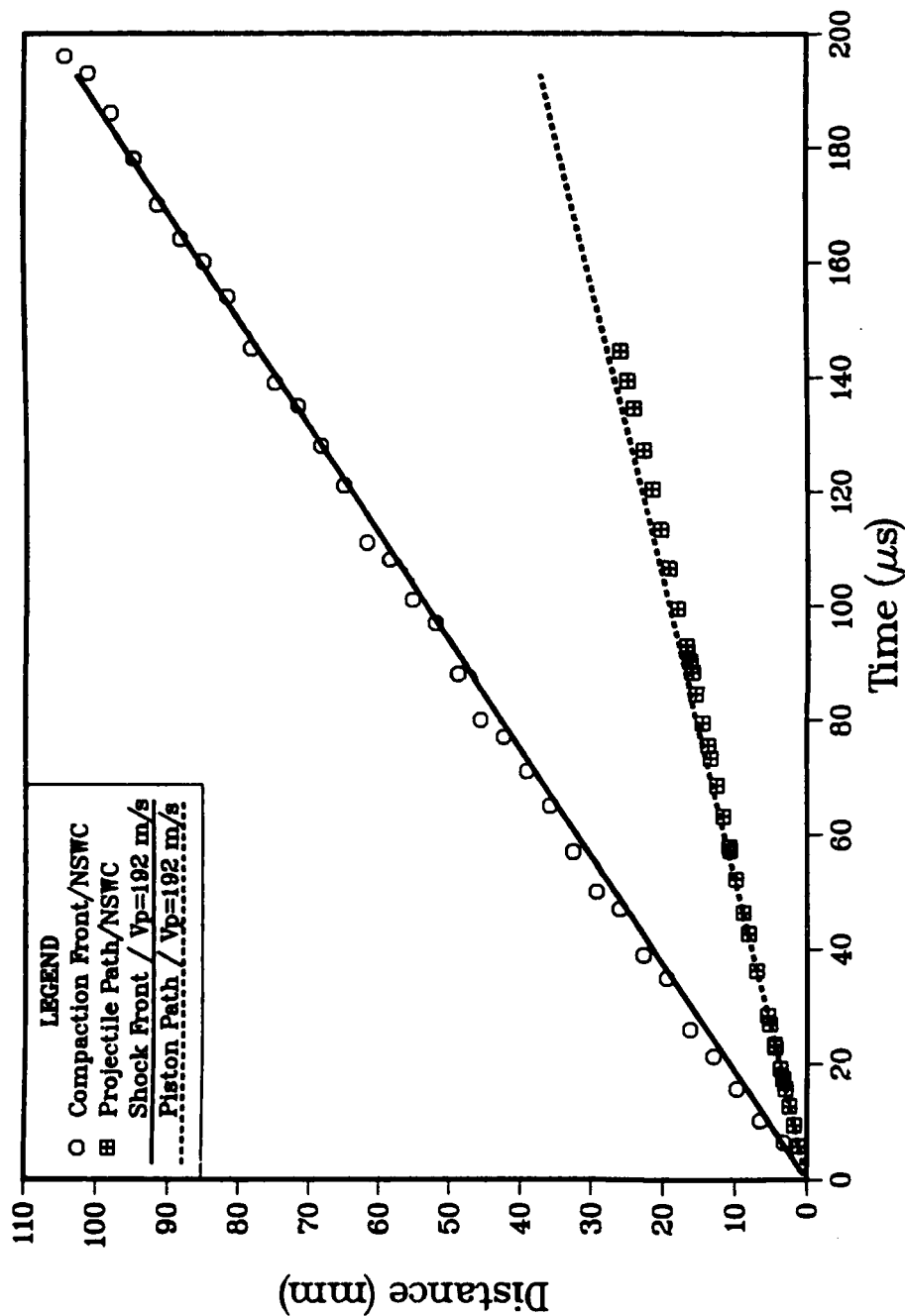
A. Influence of Projectile Path / PDC Experiment

Typical low-range response from the two wall-mounted pressure transducers can be found in PDC-81 (see Fig. 23b; gage #1 is located at 38.1 mm, gage #2 is at 76.2 mm, and tube length is 146.8 mm). After the impact-generated compaction front passes each gage location, the response shows a nearly linear "decay" from the initial maximum value until the beginning of rapid pressurization presumably due to significant reaction. The strength of this linear decay seems to increase with projectile speed at impact. None of the models at the JANNAF Modeling Workshop [32] predicted this decay, and the behavior went unexplained. Predictions of a runaway event depend critically on, and are extremely sensitive to, the competition between sources of heat generation (reactions) and heat loss mechanisms which occurs in this region. A successful model must be able to predict this stress state.

The results displayed in Figs. 23-25 are simulations of PDC-81 compared to experimental data for compaction wave locus, projectile front locus, and the wall-mounted gage records. The simulations assume no gas-phase reaction, and no solid-phase combustion other than a small amount of reaction induced by the compaction wave itself. Note that the experimental data for projectile face location (squares, in Fig. 23a) form the basis for the time-dependent boundary condition at the impacted boundary. Assuming the projectile boundary to have a constant velocity of 192 m/s produces the results shown in Fig. 23. Recall that the present theory assumes an instantaneous adjustment to the equilibrium stress state and predicts compaction waves to be infinitesimally-thin shock waves. Since true wave thickness is not simulated, the best possible comparison is for the predicted pressure jump behind the shock wave to occur at the mid-point of the initial rise reported by the experimental gage. As seen in Fig. 23, the locus of the predicted compaction wave is close to the NSWC microwave interferometry data, and the timing of the initial response from the simulated wall gages is close to the mid-point of the actual gage rise time. Similar to many other cases, the predicted magnitude of the initial maximum value is also close to the experimental value, implying that these gages are responding to the radial component of the equilibrium mixture stress state. The predicted gage response shows no evidence of a "decay"; instead there is a slight increase as the result of wall friction operating on a continuously increasing amount of aggregate which is sliding past the lateral confining boundary. Of course, with the assumption of a constant projectile velocity, this computation did not accurately simulate the projectile face location beyond, say, 50 μs .

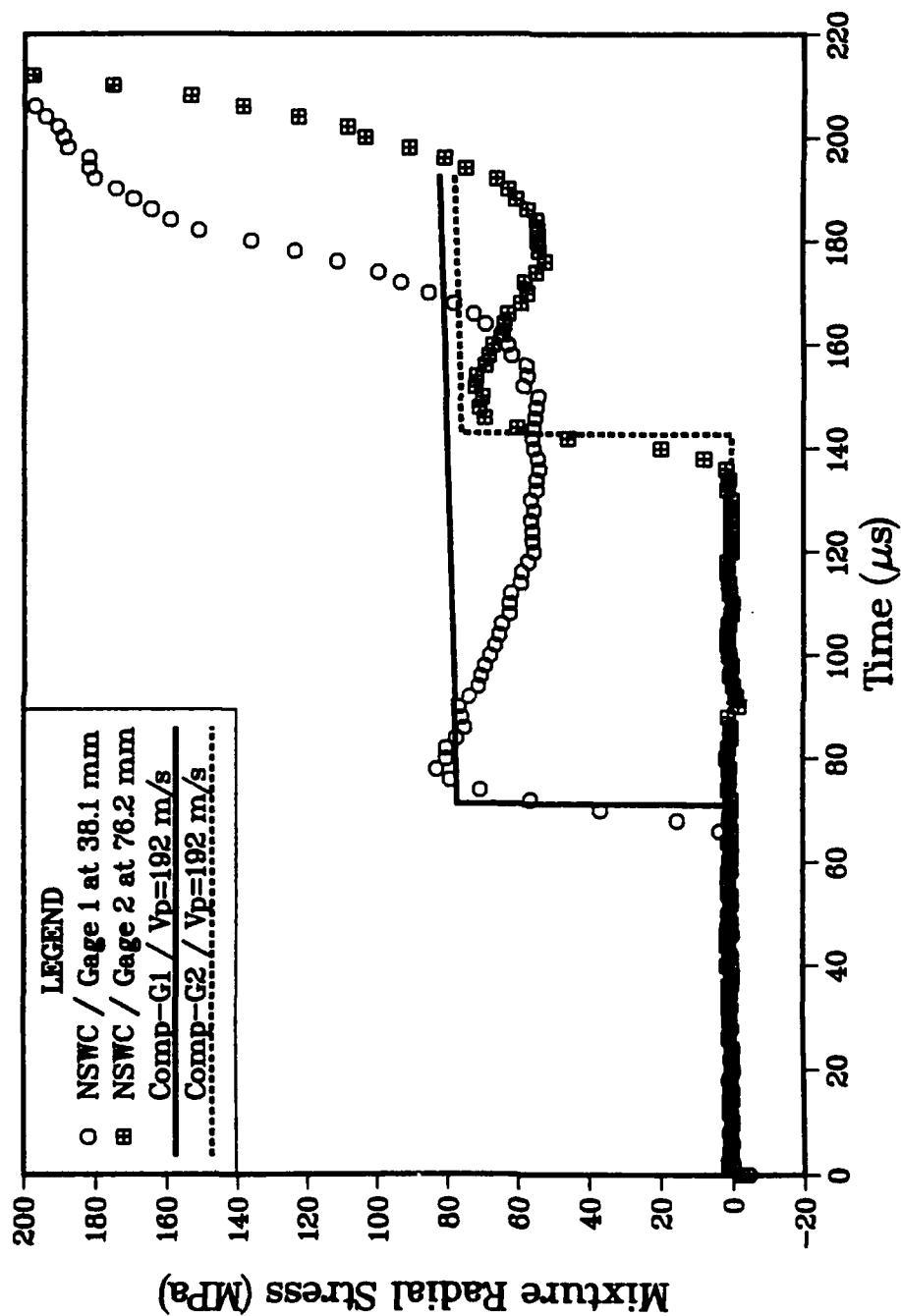
If it is assumed that the projectile velocity, near 40 μs , slows down smoothly from 192 m/s to 173 m/s, the predicted projectile locus ("dual-linear") closely matches the experimental data as illustrated in Fig. 24a. Now, however, the computed compaction wave locus falls increasingly behind the microwave data, and the computed response at gage #2 is late compared to the experimental gage record (Fig. 24b). The expansion wave created by the slowing projectile has

(text continues on page 54)



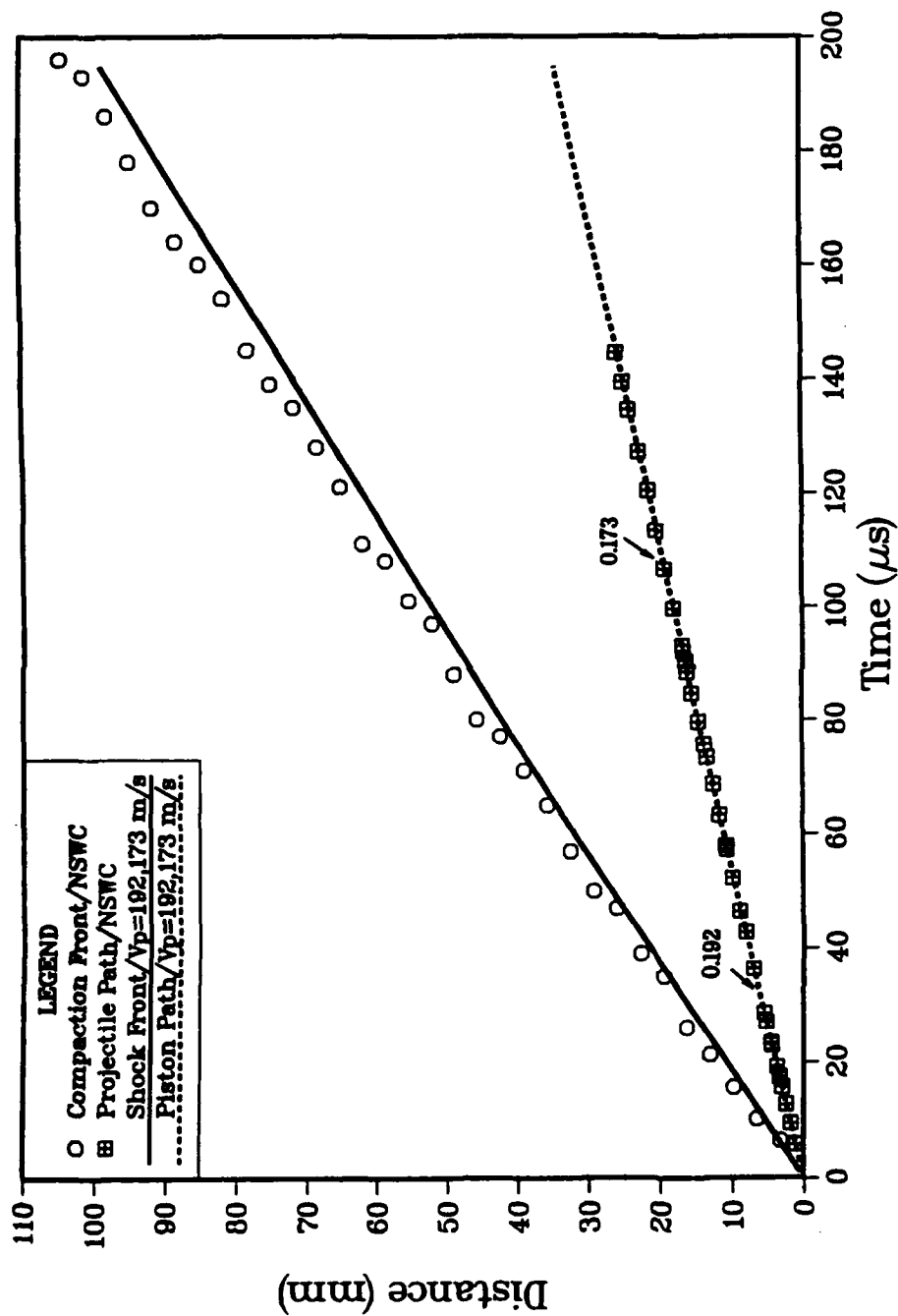
(a) Compaction wave locus and projectile locus for PDC-81.
(computation assumes projectile locus follows from constant velocity)

Figure 23 - Comparison of model predictions and NSWC data [15] from PDC-81: 237 m/s impact of Lexan projectile on 60.1% TMD TS-3659 ball propellant. Model computation assumes projectile interface speed = 192 m/s (constant), and no gas-phase reaction or propellant ignition.



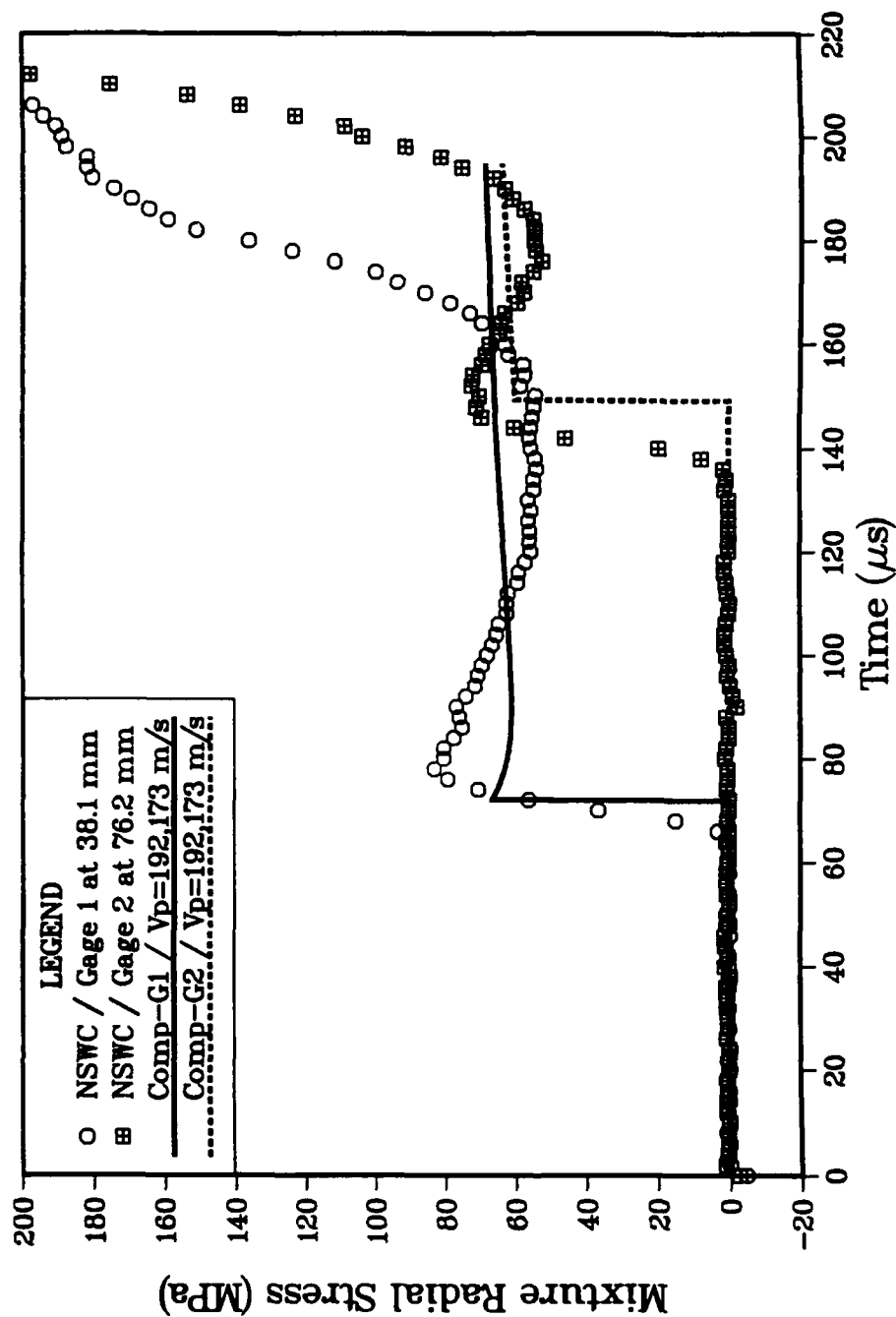
(b) Wall-mounted pressure transducer records from PDC-81.

Figure 23 - Comparison of model predictions and NSWC data [15] from PDC-81: 237 m/s impact of Lexan projectile on 60.1% TMD TS-3659 ball propellant. Model computation assumes projectile interface speed = 192 m/s (constant), and no gas-phase reaction or propellant ignition.



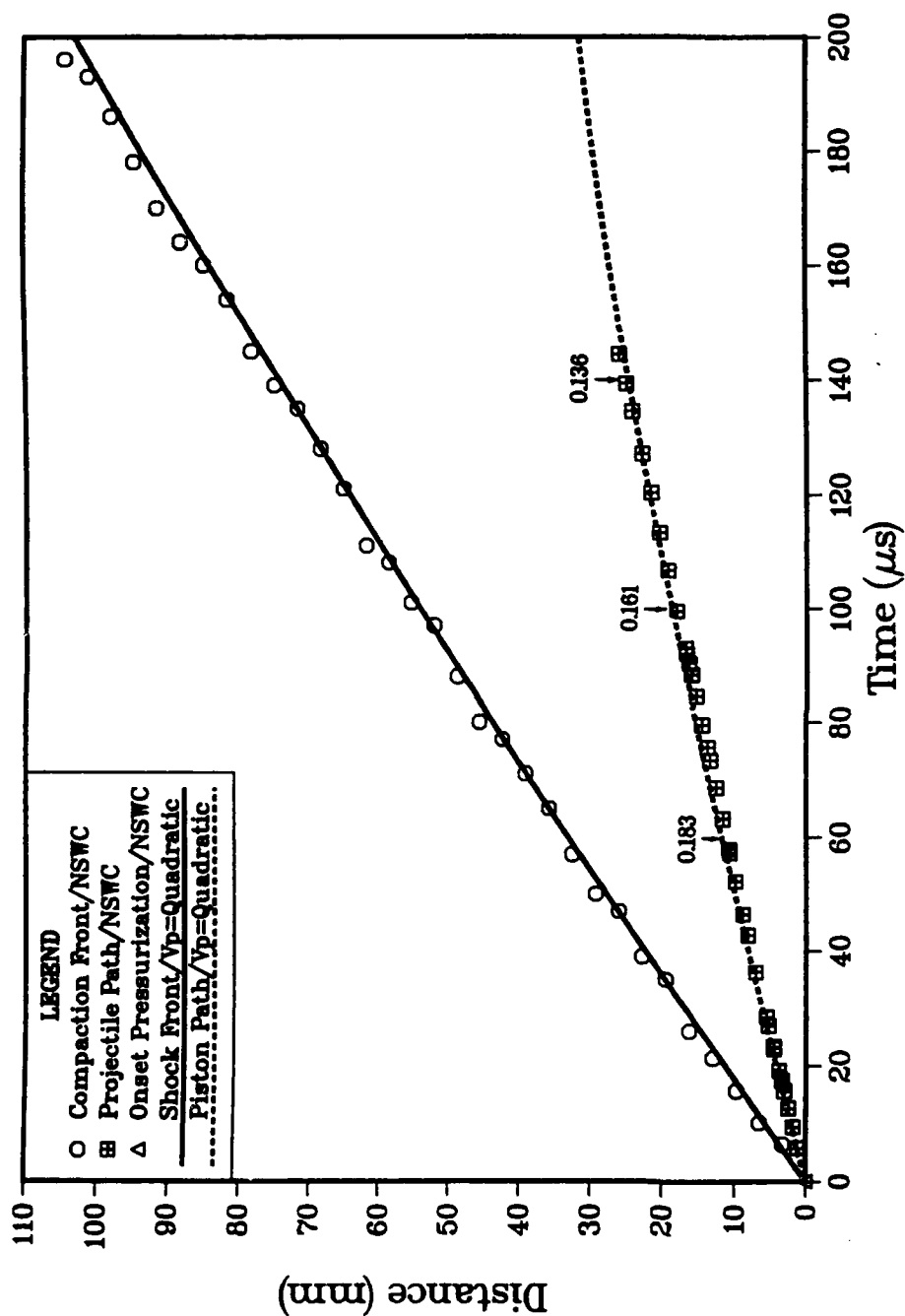
(a) Compaction wave locus and projectile locus for PDC-81.
(Computation assumes "dual-linear" projectile path; numbers are velocity in mm/ μ s)

Figure 24 - Comparison of model predictions and NSW data [15] from PDC-81: 237 m/s impact of Lexan projectile on 60.1% TMD TS-3659 ball propellant. Model computation based on "dual-linear" projectile path; projectile interface speed = 192 m/s up to 40 μ s, then = 173 m/s. Computation assumes no gas-phase reaction or propellant ignition.



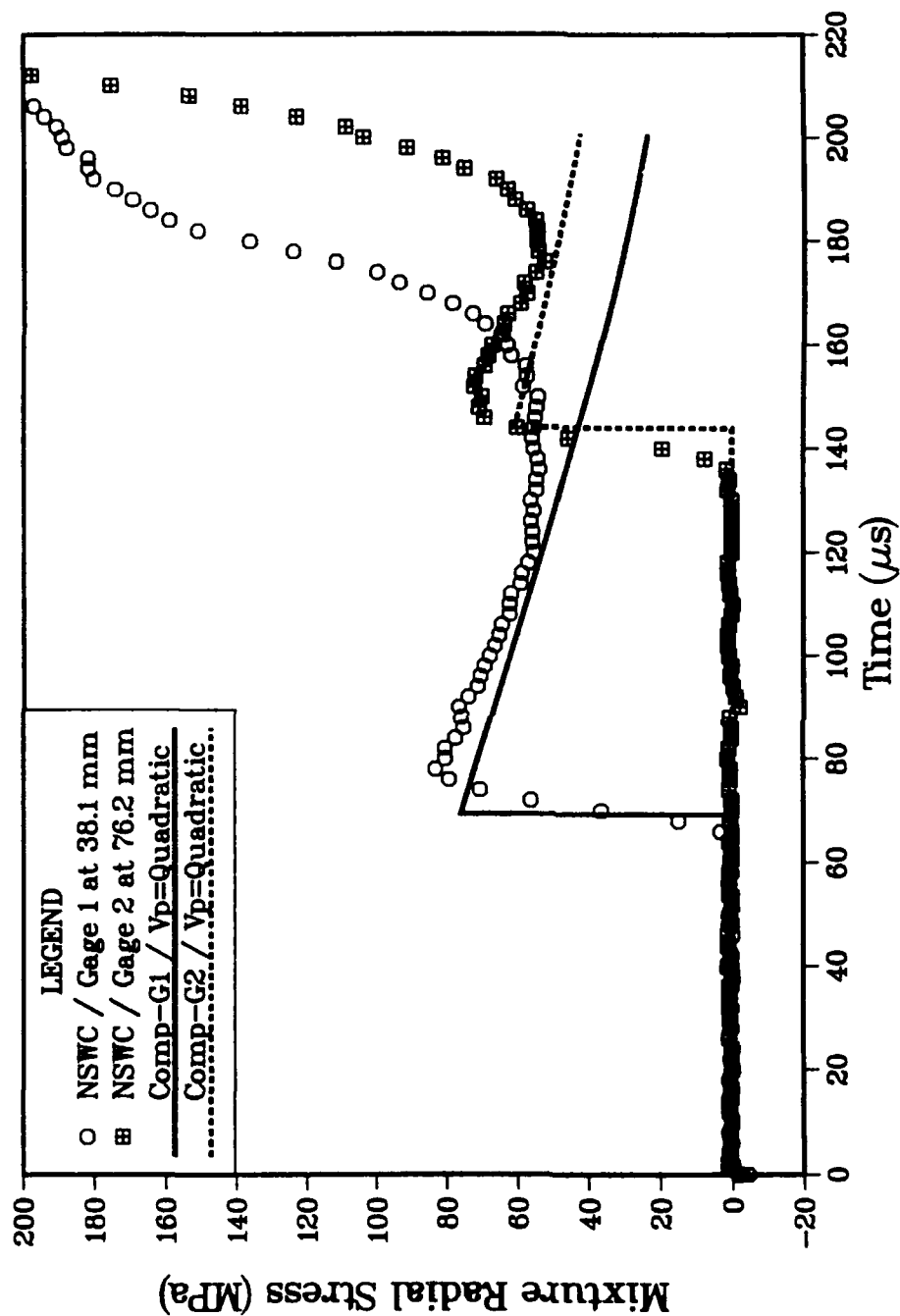
(b) Wall-mounted pressure transducer records from PDC-81.

Figure 24 - Comparison of model predictions and NSWC data [15] from PDC-81: 237 m/s impact of Lexan projectile on 60.1% TMD TS-3659 ball propellant. Model computation based on "dual-linear" projectile path; projectile interface speed = 192 m/s up to 40 μ s, then = 173 m/s. Computation assumes no gas-phase reaction or propellant ignition.



(a) Compaction wave locus and projectile locus for PDC-81.
(Computation assumes "quadratic" projectile path; numbers are velocity in mm/ μ s)

Figure 25 - Comparison of model predictions and NSWC data [15] from PDC-81: 237 m/s impact of Lexan projectile on 60.1% TMD TS-3659 ball propellant. Model computation based on "quadratic" projectile path; projectile interface speed is a quadratic function of time. Computation assumes no gas-phase reaction or propellant ignition.



(b) Wall-mounted pressure transducer records from PDC-81.

Figure 25 - Comparison of model predictions and NSWC data [15] from PDC-81: 237 m/s impact of Lexan projectile on 60.1% TMD TS-3659 ball propellant. Model computation based on "quadratic" projectile path; projectile interface speed is a quadratic function of time. Computation assumes no gas-phase reaction or propellant ignition.

lowered the magnitude of both gage responses (Fig. 24b), but at best the computed response represents an "average" of the experimental data. The linear decay region is still not predicted.

Out of frustration, this investigation began to examine the problem from another point of view. With Ref. 26b and the discussions at the JANNAF Modeling Workshop [32] as background, it was postulated that substantial deformation of the front face of the Lexan projectile in the PDC experiment may indeed be important. This deformation might not be reflected in the position of scribe lines on the body of the projectile, which is the basis of the experimental data for projectile locus. Assume for the moment that the microwave data for compaction wave locus is more accurate than the data given for projectile locus. On close examination, the microwave data for compaction wave locus actually show a curved path. If it can be assumed that the compaction (shock) wave locus up to a time of, say, 120 μ s is not substantially influenced by reaction, then the effective projectile path must also have been curved (not two straight lines). This study posed the inverse problem: attempt to determine the projectile path which will create the experimental compaction wave locus. One possibility (not a unique answer) is shown by the results in Fig. 25. As can be seen, a slight curvature to the projectile path (projectile velocity is quadratic in time) leads to a computed compaction wave locus which is a close match with the NSWC microwave data (Fig. 25a). Furthermore, the predicted gage response DOES reproduce the linear decay behavior seen by the wall-mounted pressure transducers (Fig. 25b). On the basis of these examples, this investigation feels with reasonable certainty that the front face of the Lexan projectile in the PDC experiments was deforming under impact, and that the true locus was a curved path. The important implication is that the true path is not accurately known. As discussed below, this has important consequences in attempting to verify reaction mechanisms when the basis of comparison is the wall-mounted gage records.

B. Simulation of PDC-M34 / 65% TMD Melamine (Inert Material)

Before addressing the complexities created by impact-induced reaction, it would be interesting to evaluate how well the theory can simulate the NSWC PDC experiment when the confined granular material is inert. A recent run denoted PDC-M34 [53] (see Fig. 26 below) involved 65% TMD melamine (Eastman 1540) which has a particle size distribution between 46 - 56 μ m. In addition to the fact that melamine should behave as an inert, PDC-M34 employed an aluminum projectile (206 m/s initial speed) which should not deform under impact. This removes the uncertainties in projectile locus caused by deformation of a Lexan projectile as discussed in Section VI-A. Furthermore, confinement in PDC-M34 was provided by a 147 mm long thick-walled steel tube which effectively eliminates radial expansion of the tube wall. As in the earlier PDC experiments, the locus of the projectile face was determined from the motion of scribe lines on the projectile body as recorded by a high-speed camera looking through a slit in the tube wall. Microwave interferometry through the downstream end of the tube was used to determine the location of the strong compaction front. The time-history of the stress field was monitored at three fixed locations by the wall-mounted pressure transducers noted in Fig. 26.

Before the transient model can predict wave behavior, it is necessary to evaluate the equilibrium stress state of the granular aggregate. This calibration is done against data obtained in the quasi-static compaction experiment. Nearly ten years ago, Elban et. al. [52] determined the three data sets plotted in Fig. 27a as

NSWC Shot PDC-M34 / 65% TMD Melamine

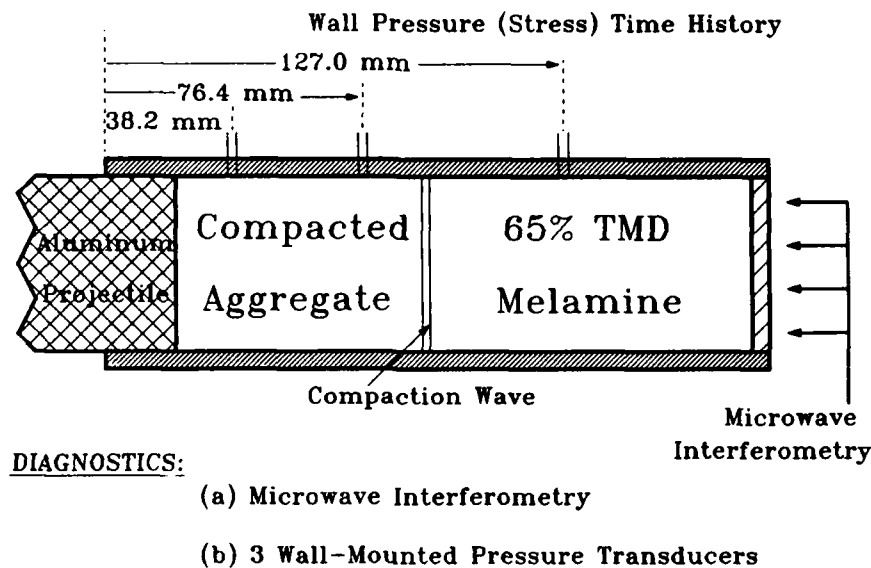
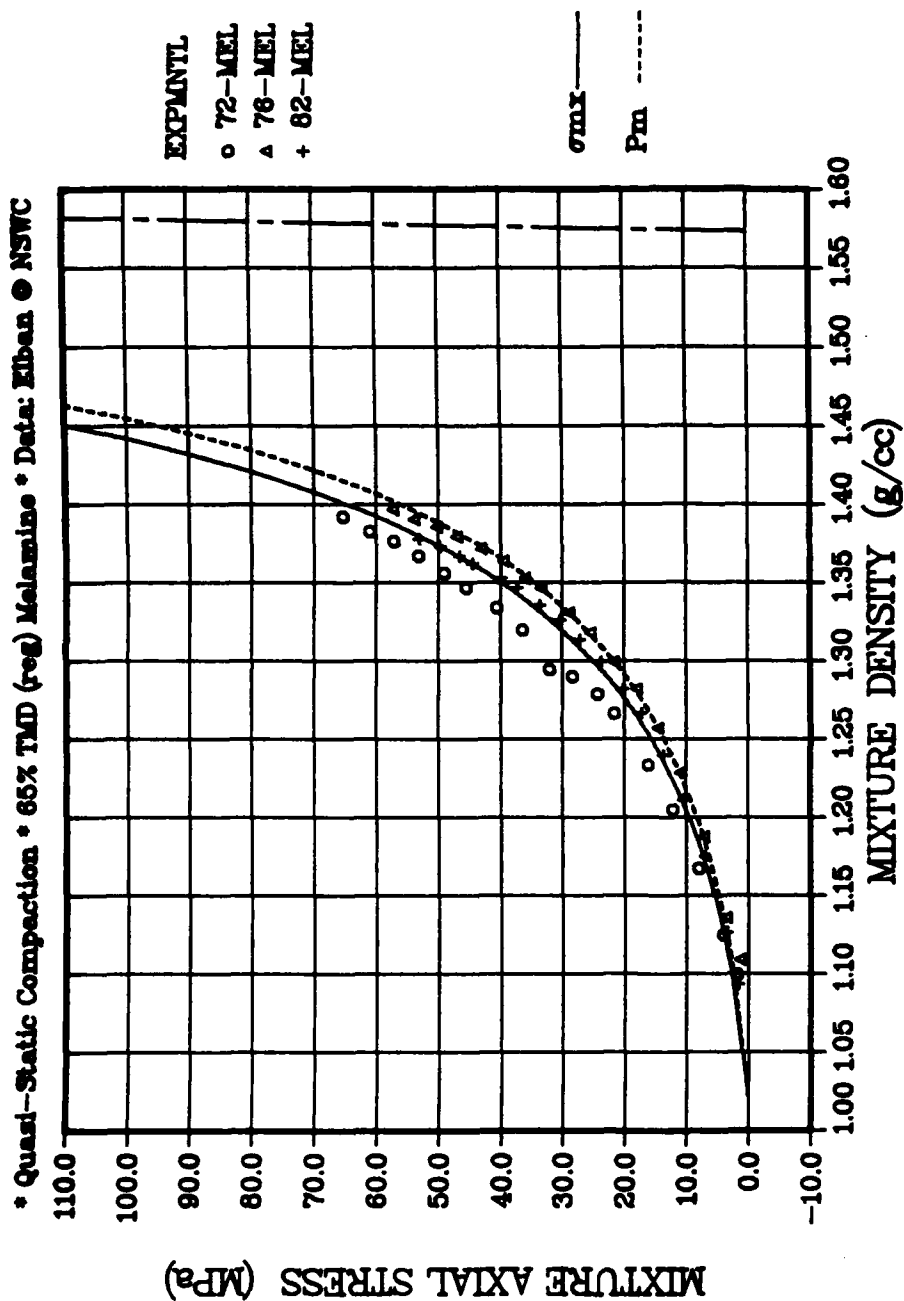


Figure 26 - Schematic of NSWC piston-driven-compaction shot PDC-M34 [53].

representative of 65% TMD melamine. The solid line shown in Fig. 27a is a "best fit" approximation generated by the present theory when $\tau_1=1.0$ (kpsi), $p_1=0.0$, $B_2=4.0$ and $p_2=0.7$ (same as in Fig. A-1, p. 67 in Ref. 34). In the discussion to follow, this representation will be referred to as "regular" melamine. The equilibrium shock wave theory developed in Ref. 34 uses the equilibrium stress state to predict values of compaction wave speed as a function of particle velocity. These predictions for regular melamine, shown as the dashed line in Fig. 28, are compared with values of compaction wave speed from two earlier PDC experiments [13] (PDC-41A and 41B) in 65% TMD melamine. The comparison is well within the range attributable to the particle size distribution in melamine as illustrated by the quasi-static compaction data sets in Fig. 27a. Thus, the analysis of Ref. 34 which assumes that the granular aggregate instantaneously adjusts to the equilibrium stress state appears to predict the correct behavior of compaction wave speed in melamine.

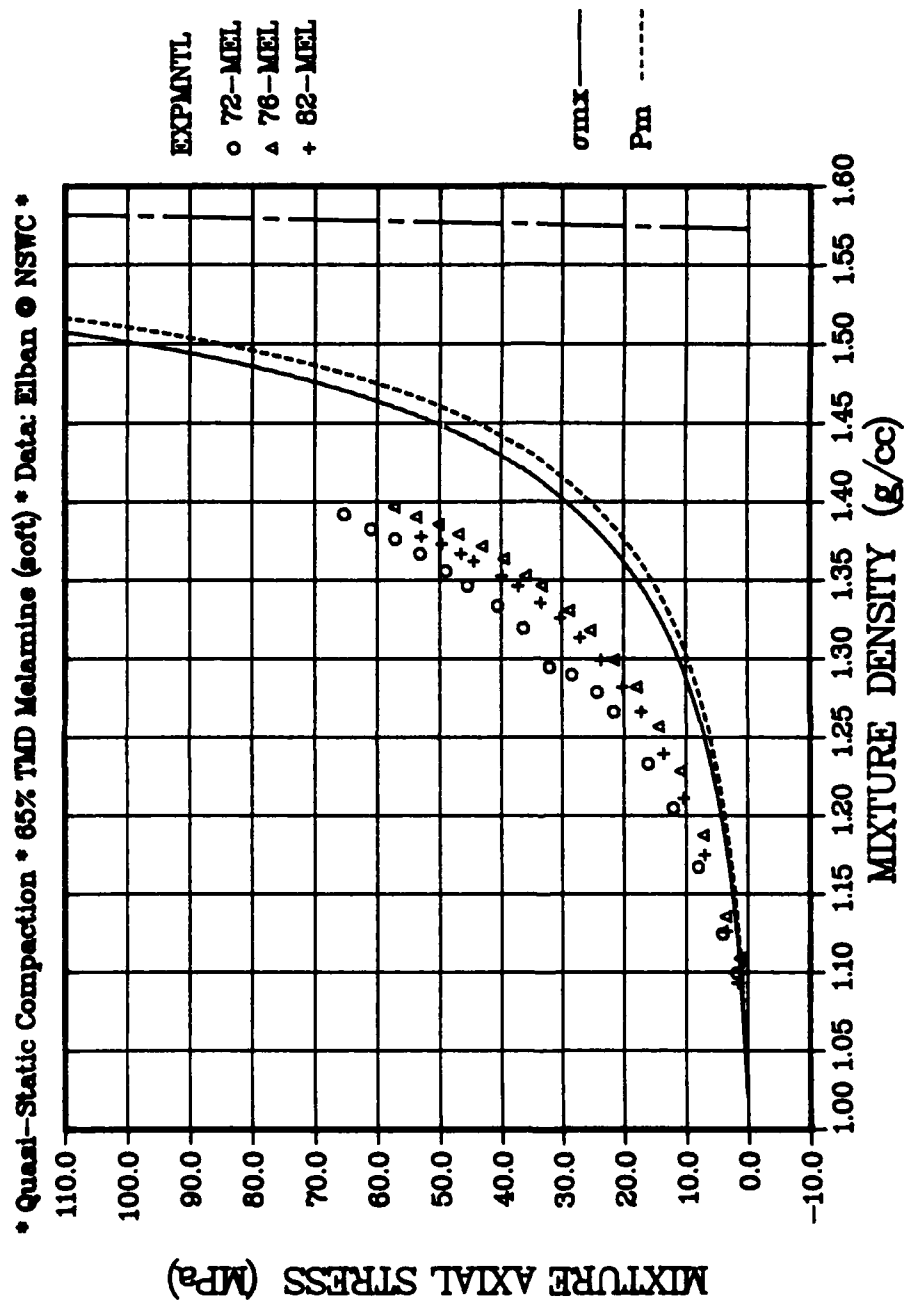
The PDC experiment of interest here is PDC-M34 [53] which also involved 65% TMD melamine but was run very recently (Dec 1989). The value of compaction wave speed (from the microwave data) just after impact is plotted in Fig. 28 which shows that this value is located considerably below the prediction for an inert compaction wave. Now if dynamic resistance to porosity change at this particle velocity has become important, the observed value of wave speed should lie above (not below) the theoretical prediction which has ignored it. An explanation may be related to the age of the material; ten-year old melamine may have absorbed moisture and aged such that the granular aggregate now offers less resistance (is "softer") to compaction forces than it did in Elban's [52] original measurements. Exploring this hypothesis, the present study arbitrarily adjusted one of the parameters ($B_2=1.75$) controlling the strength of the equilibrium stress state to obtain the solid line shown in Fig. 27b denoted as "soft" melamine. Again using the equilibrium shock wave theory [34], predictions for compaction wave speed in "soft" melamine are shown as the solid line in Fig. 28; the intent was to get

(text continues on page 62)



(a) "Regular" melamine (defined by $\tau_1=1.0$ kpsi, $p_1=0$, $B_2=4.0$, $p_2=7$ in Eq. 9).

Figure 27 - Quasi-static stress state for isothermal compaction of melamine initially at 65% TMD. Data from Elban et. al. [52]. Solid line represents approximation for axial component of mixture stress, σ_{mx} ; dashed line represents mixture pressure, P_m ; chain-dot line represents TMD.



(b) "Soft" melamine (defined by $\tau_1=1.0$ kpsi, $p_1=0$, $B_2=1.75$, $p_2=.7$ in Eq. 9).

Figure 27 - Quasi-static stress state for isothermal compaction of melamine initially at 65% TMD. Data from Elban et. al. [52]. Solid line represents approximation for axial component of mixture stress, σ_{mx} ; dashed line represents mixture pressure, P_m ; chain-dot line represents TMD.

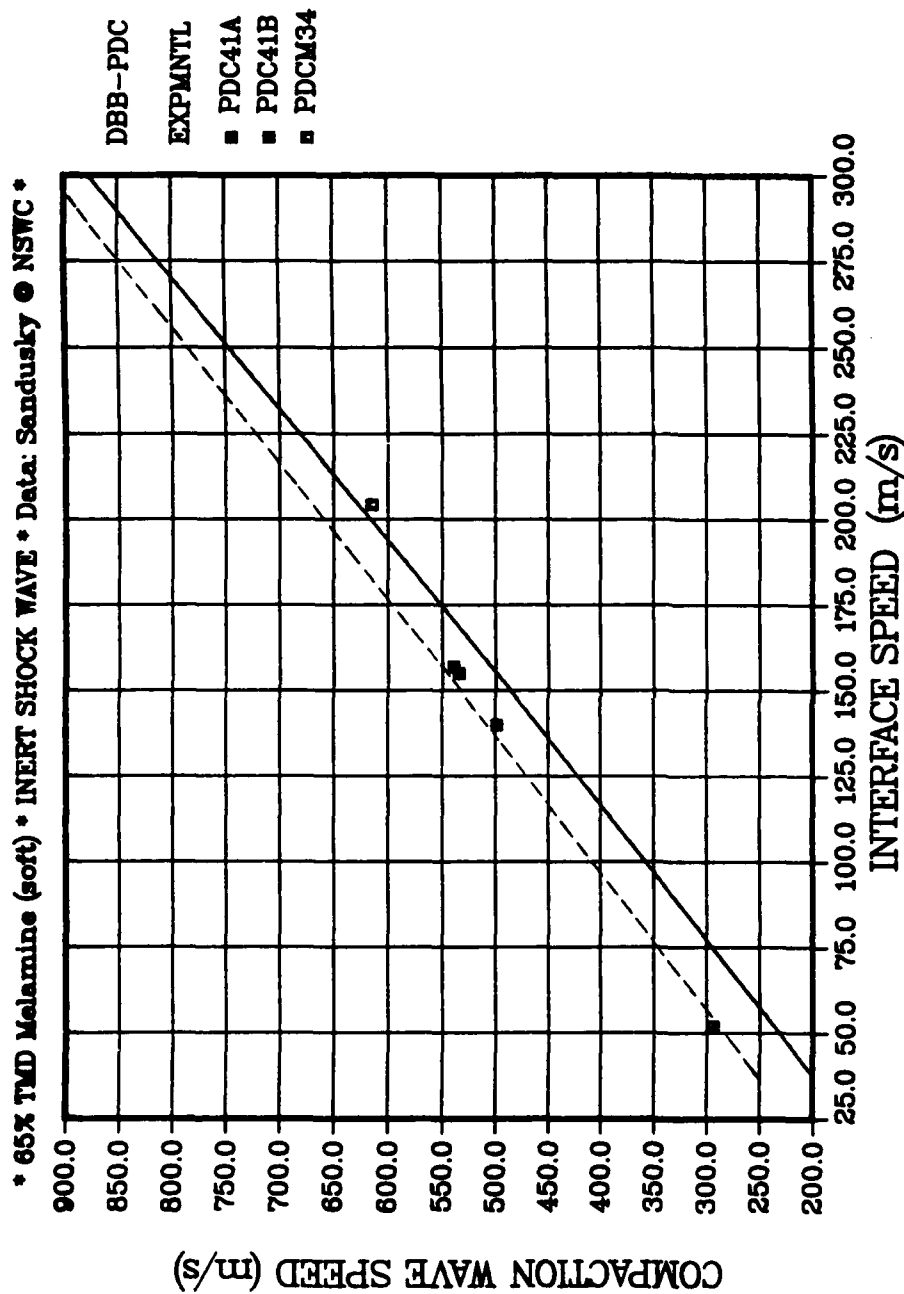


Figure 28 - Using analysis of Ref. 34, predicted compaction wave speed vs. interface speed (particle velocity) for melamine initially at 65% TMD. PDC data (41A and 41B) from Sandusky and Liddiard [13]; dashed line is prediction based on "regular" melamine. PDC data (M34) from Sandusky and Glancy [53]; solid line is prediction based on "soft" melamine.

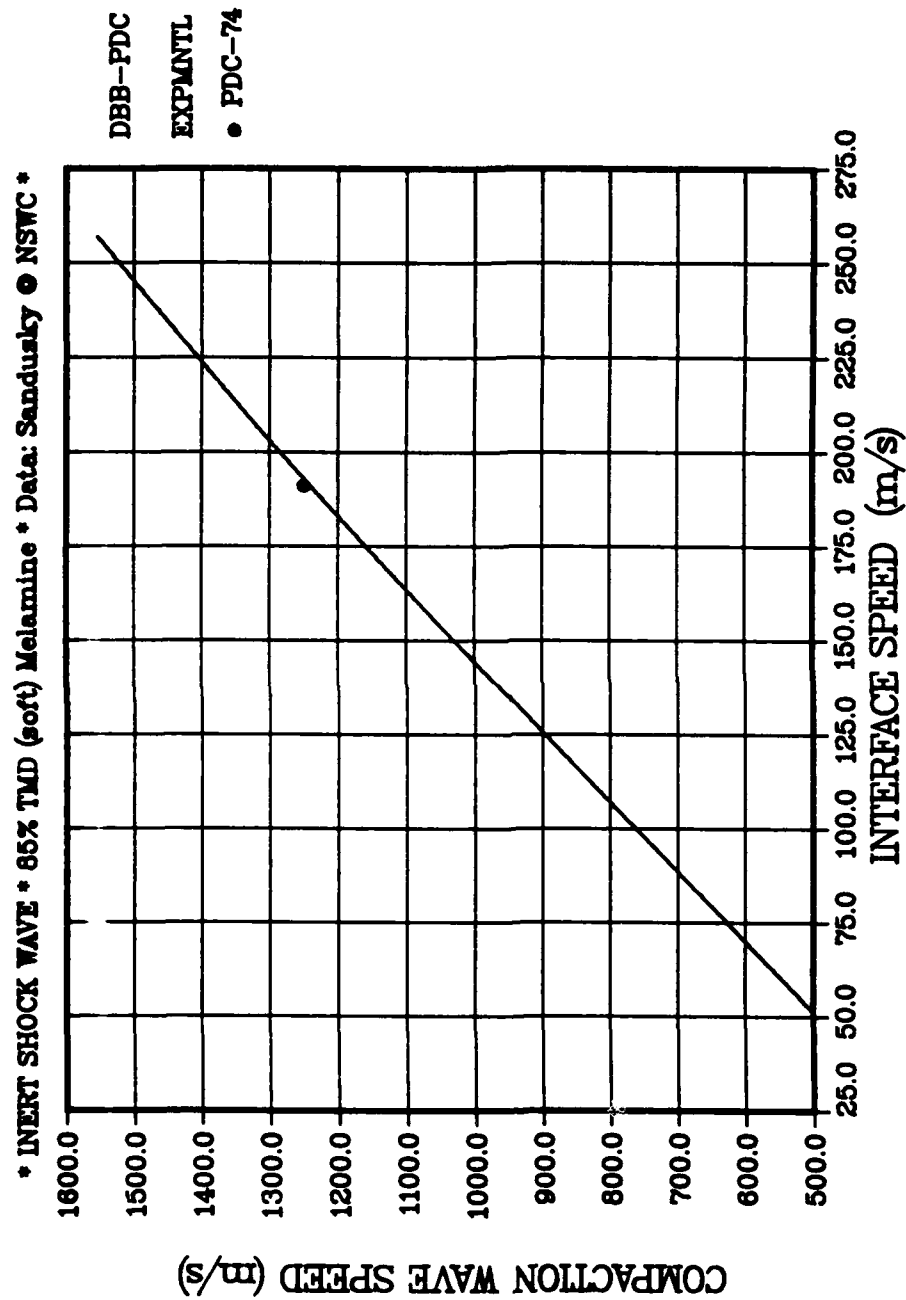
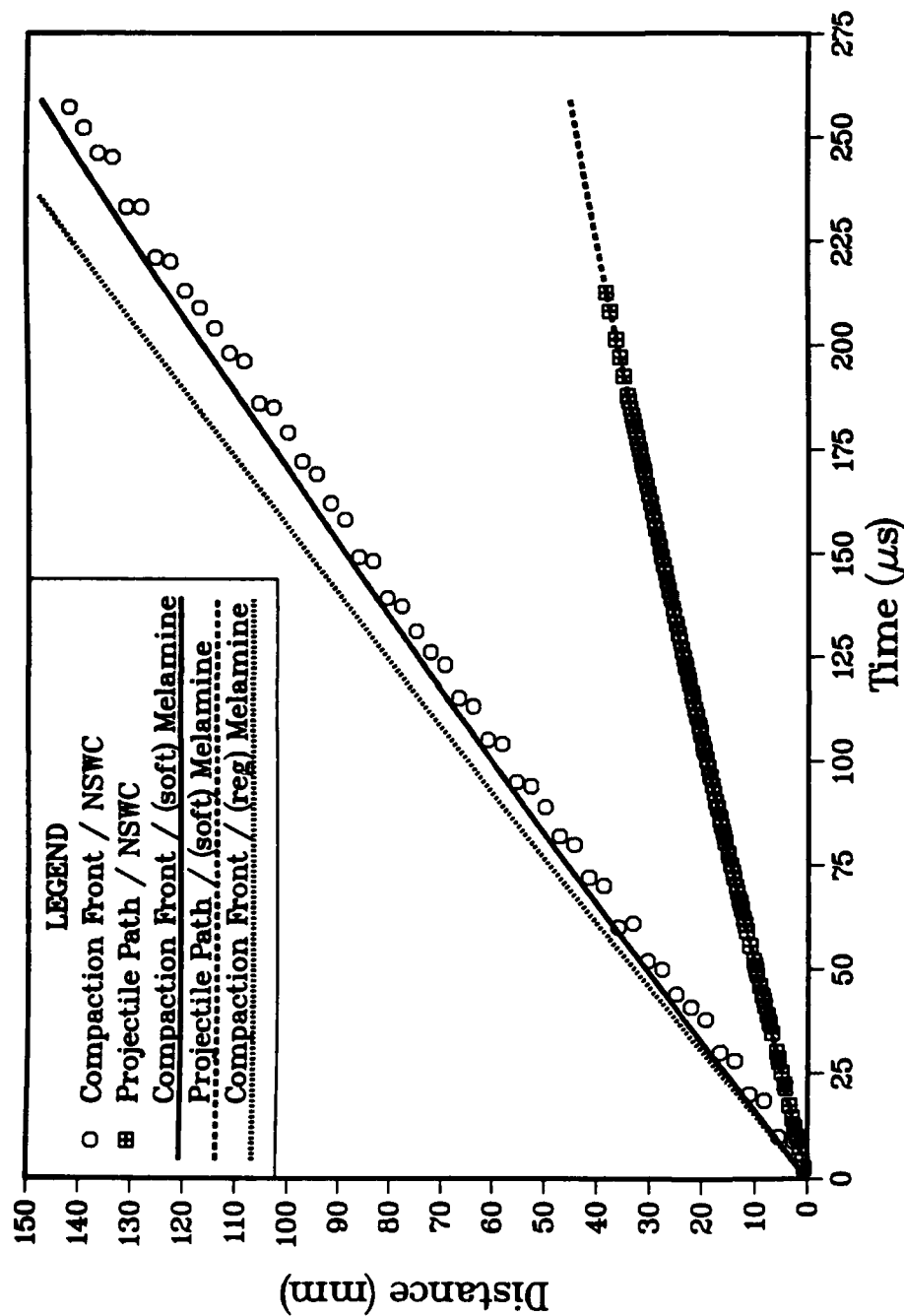
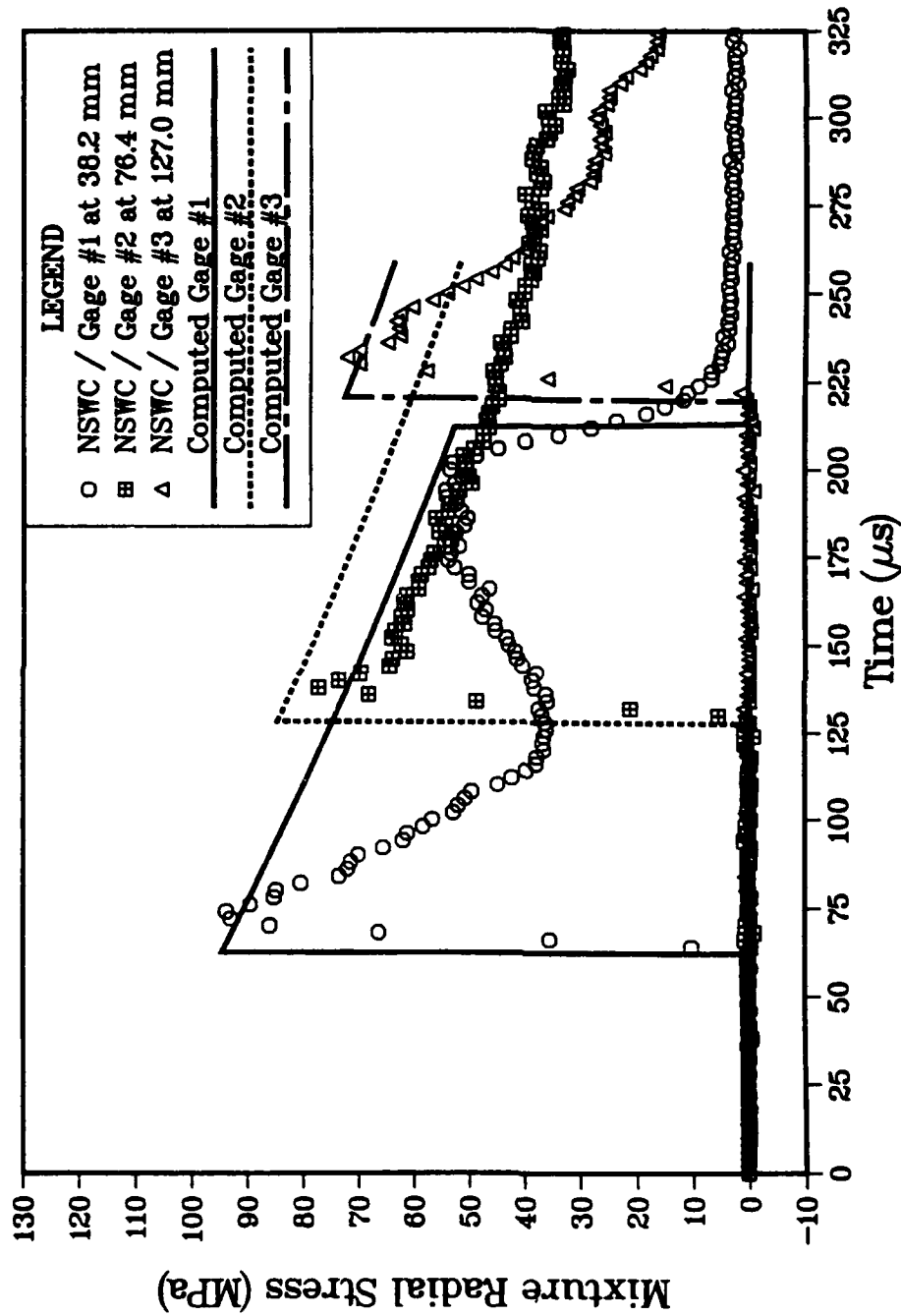


Figure 29 - Using analysis of Ref. 34, predicted compaction wave speed vs. interface speed (particle velocity) for melamine initially at 85% TMD. PDC data (74) from Sandusky and Glancy [53]; solid line is prediction based on "soft" melamine.



(a) Comparison of NSWC data [53] for compaction wave locus and projectile face locus with model predictions. NSWC projectile locus is used as boundary condition. Solid line is predicted compaction wave locus based on "soft" melamine; dotted line is based on "regular" melamine.

Figure 30 - Comparison of model predictions with NSWC data [53] from PDC-M34: 206 m/s impact of aluminum projectile on 65% TMD melamine. Simulation ignores wall friction and assumes melamine is inert.



(b) Comparison of NSWC data [53] from wall-mounted pressure transducers with model simulation based on "soft" melamine initially at 65% TMD.

Figure 30 - Comparison of model predictions with NSWC data [53] from PDC-M34: 206 m/s impact of aluminum projectile on 65% TMD melamine. Simulation ignores wall friction and assumes melamine is inert.

close to the experimental value for PDC-M34, not to match it exactly. Another recent PDC run in melamine may support the "softening" hypothesis. During check-out of a remotely operated quasi-static compaction apparatus at NSWC, melamine was compacted to 85% TMD. The PDC run denoted PDC-74 [53] involved a 217 m/s impact on this 85% TMD aggregate. Since there is no quasi-static compaction data available for melamine initially at 85% TMD, the present theory was used to estimate the behavior, and then this equilibrium stress state was supplied to the equilibrium shock wave theory [34]. The resultant predictions are shown in Fig. 29 along with the experimental value of compaction wave speed from PDC-74. The comparison is quite good, suggesting that the assumed "soft" melamine properties do describe the behavior of ten-year old melamine used recently in the PDC experiment.

The simulation of PDC-M34 is based on the assumption that the equilibrium stress state is described by "soft" melamine. The time-dependent projectile-face boundary condition follows from a quadratic function of time which was fit to the NSWC projectile path data (see Fig. 30a). The predicted compaction wave locus (solid line in Fig. 30a) is slightly ahead of the NSWC microwave data, but this calculated compaction wave locus appears to mimic the observed curvature. The predicted transducer response (radial component of mixture stress) is compared to the experimental data for all three gage locations in Fig. 30b. The computed values of initial response seem to be close to the transducer data in all three cases. Note that the quadratic path of the aluminum projectile has produced a linear "decay" behavior in each computed gage response which is quite similar to that discussed in Section VI-A above. However, there are significant deviations after the initial response. Particularly at gage #1, the calculation does not reproduce the sharp decrease in stress, nor the subsequent recovery. Interestingly, the experimental record recovers to approximately the calculated values just as the gage location is covered by the moving projectile. At gage #2, the experimental record begins with a sharp decrease but then suddenly levels out to a curve which is nearly parallel to the computed response. The brief comparison at gage #3 ends when the computation predicts the compaction wave has reached the downstream boundary. The transducer records beyond approximately 260 μ s may have been influenced by wave motion reflected from this downstream boundary.

The computation suggests that a smooth expansion wave system propagates into the compressed aggregate as the projectile velocity slows down along the quadratic path in time. This expansion wave system provides an explanation for the decreasing initial maximum value reported by successive transducers, and the gentle decay seen by gage #2. However, it offers no explanation for the sharp decrease and subsequent recovery seen by gage #1, or the initial sharp decrease seen by gage #2. Sandusky [53] has speculated that these events may be the result of a slightly-recessed 4 mm diameter transducer responding to a sliding aggregate composed of 50 μ m diameter particles.

C. Influence of Energy Release / PDC Experiment

Our previous theory [34] for a quasi-steady reactive shock wave suggested that ignition of the compacted aggregate might be controlled by heat transfer from the hot gaseous products trapped in the pores (hot pockets) of the aggregate. It was postulated that ignition would begin when a sufficient thermal wave was established in the cold solid material surrounding these pores. The crucial issue is the initial temperature of the gases in the pores. Recall that for TS-3659 propellant, Glancy et al. [15] conducted three PDC runs in Lexan confinement at

impact speeds up to 290 m/s and failed to see any evidence of light on the camera records, although the tube ruptured. This observation implies that wave-induced reaction in TS-3659 releases only a fraction of the total energy, and this fraction is less than the value which would produce gas-phase temperatures of say 1500°K. For the computation of PDC-80 shown in Fig. 31a, the amount of energy released in the wave-induced reaction was adjusted such that the temperature of the gases trapped in the pores of the aggregate was approximately 1450°K. This simulation of PDC-80 included wall boundary friction, accounted for heat transfer to the solid material, but no further gas-phase reaction. None of the solid surface reached the 473°K surface temperature ignition criterion, and hence no ignition occurred. Since the transducers clearly show that reaction did begin before the end of this calculation, it is concluded that heat transfer from an inert hot gas trapped in the pores cannot be the sole source of ignition. At least for TS-3659 propellant, there must be some additional source of reaction which leads to ignition of the aggregate.

This study explored the possibility that a delayed gas-phase reaction, which converts R_1 to R_2 , is the additional source of energy which ignites the granular solid material. Bäer and Nunziato [19,20] have postulated a "compressive" reaction with a sudden increase in energy release which accomplishes the same result. The discussion example is based on PDC-80, simulated with a constant projectile speed of 127 m/s which gives a good representation of the projectile locus up to a time of 200 μ s (see Fig. 31b). Assuming a 96 μ s delay (and the parameters listed in Table I) produces the results shown in Fig. 32a for gage #1. In a rough sense, the runaway pressure curves have the correct shape but the "break away" is more abrupt than the experimental data would indicate. This behavior is typical of all computations which assume that, immediately after ignition, combustion produces full energy release (solid $\rightarrow R_2$). The two curves in Fig. 32a differ only in the amount of surface area within the aggregate which is involved in the combustion process. The steeper curve (chain-dash) is produced by combustion of the full surface area of the deformed grains, while the solid curve follows from combustion of only the exposed surface area of the grains. The "knee" in this curve in the

(text continues on page 70)

Table I - Input Parameters for PDC-80

60.2% TMD TS-3659 Propellant

Gas-Phase Reaction: $t_{del}^0 = 85$ microsecs

$$A_{gr} = 1.3 \times 10^6 (\text{sec-cm}^3)^{-1}$$

$$E_{gr} = 7500 \text{ K}$$

$$\Delta e_{gr}^0 = 900 \text{ cal/g}$$

Combustion (Solid $\rightarrow R_2$): $r(\text{cm/s}) = .244 P(\text{MPa})^{0.857}$

Energy Release:

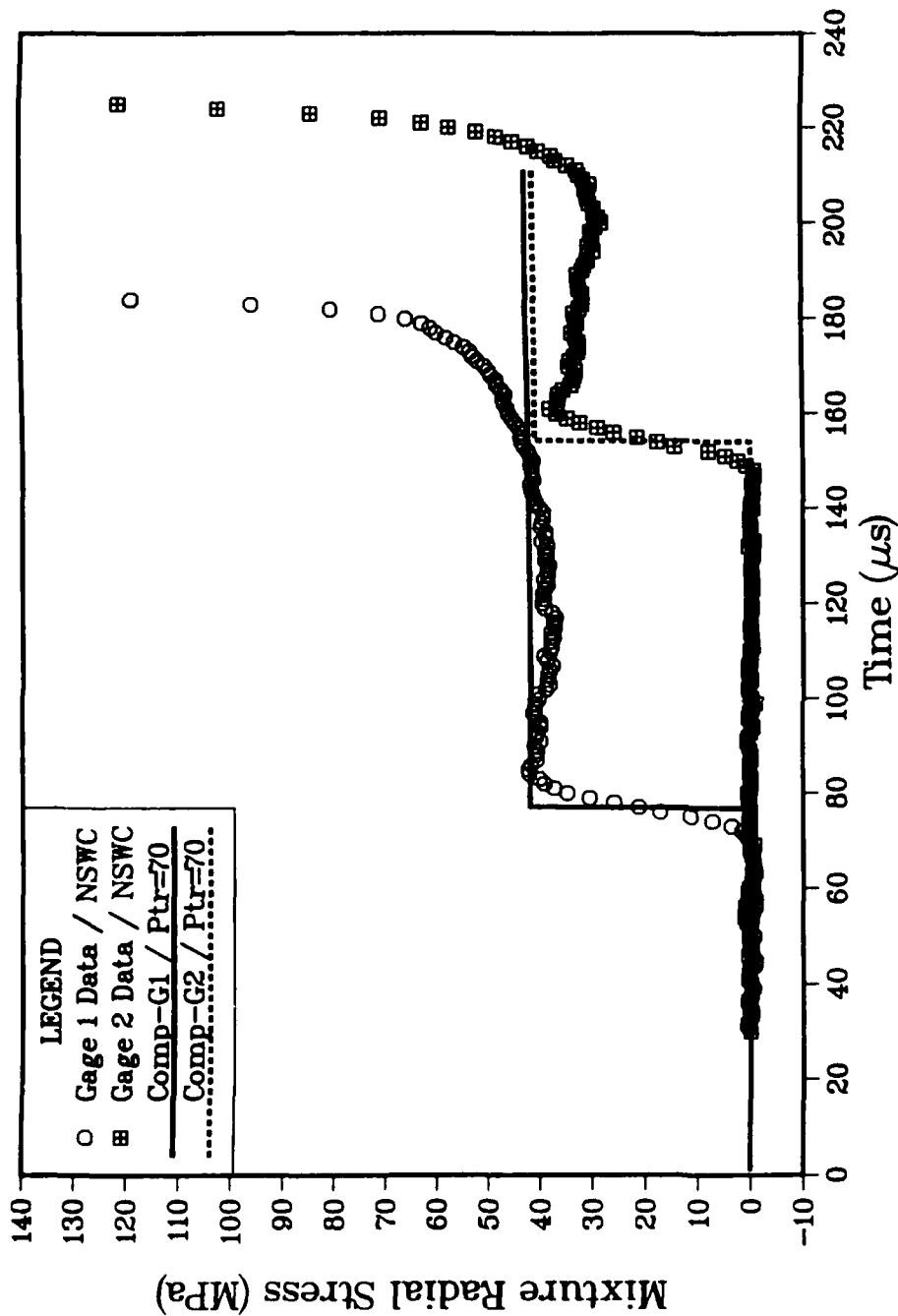
$$(a) \text{ Solid } \rightarrow R_2 : 1104 \text{ cal/g}$$

$$(b) \text{ Solid } \rightarrow R_1 : 204 \text{ cal/g}$$

$$(c) R_1 \rightarrow R_2 : 900 \text{ cal/g}$$

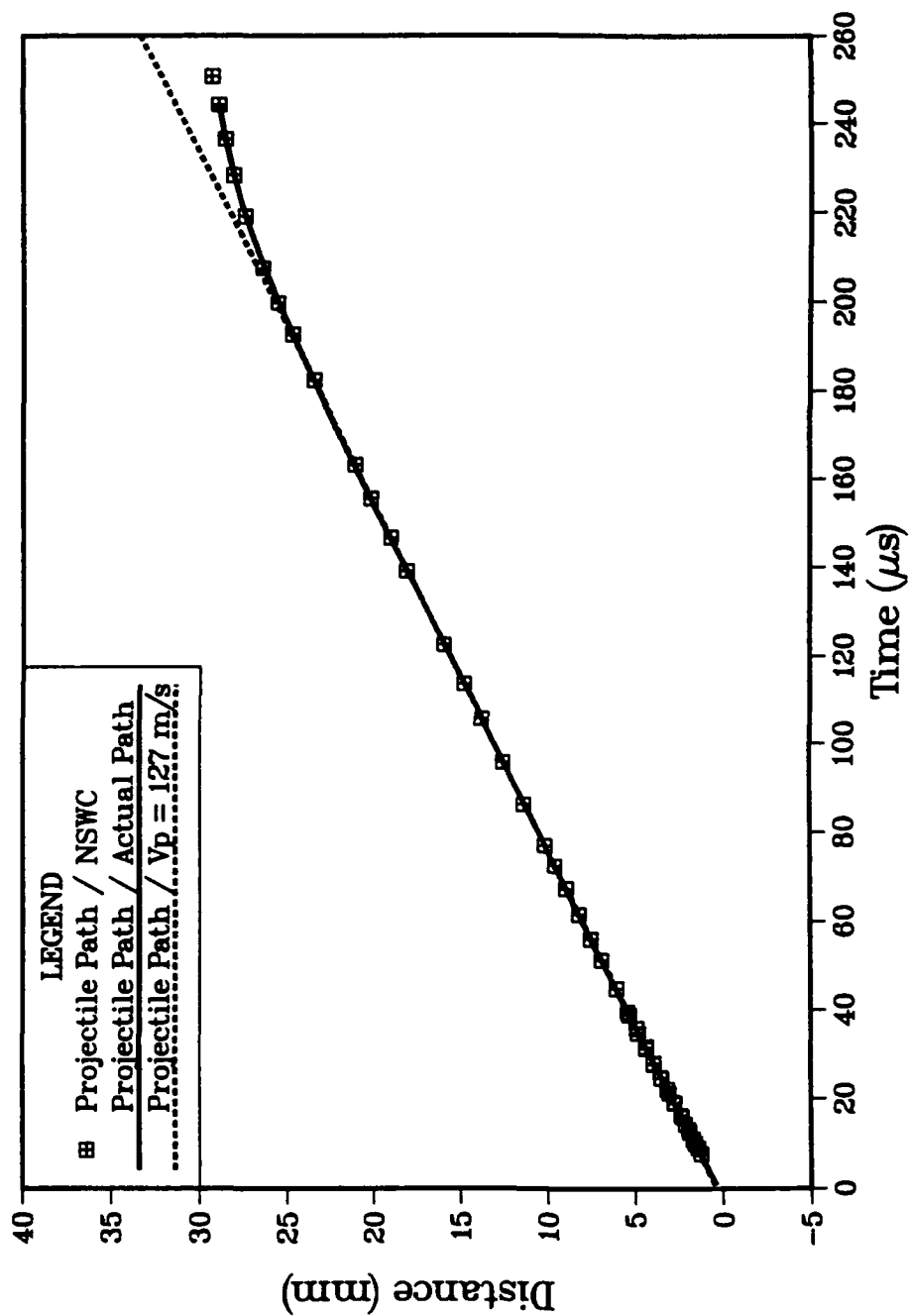
Wave-induced Reaction: (b)

$$\eta = 1.8\%$$



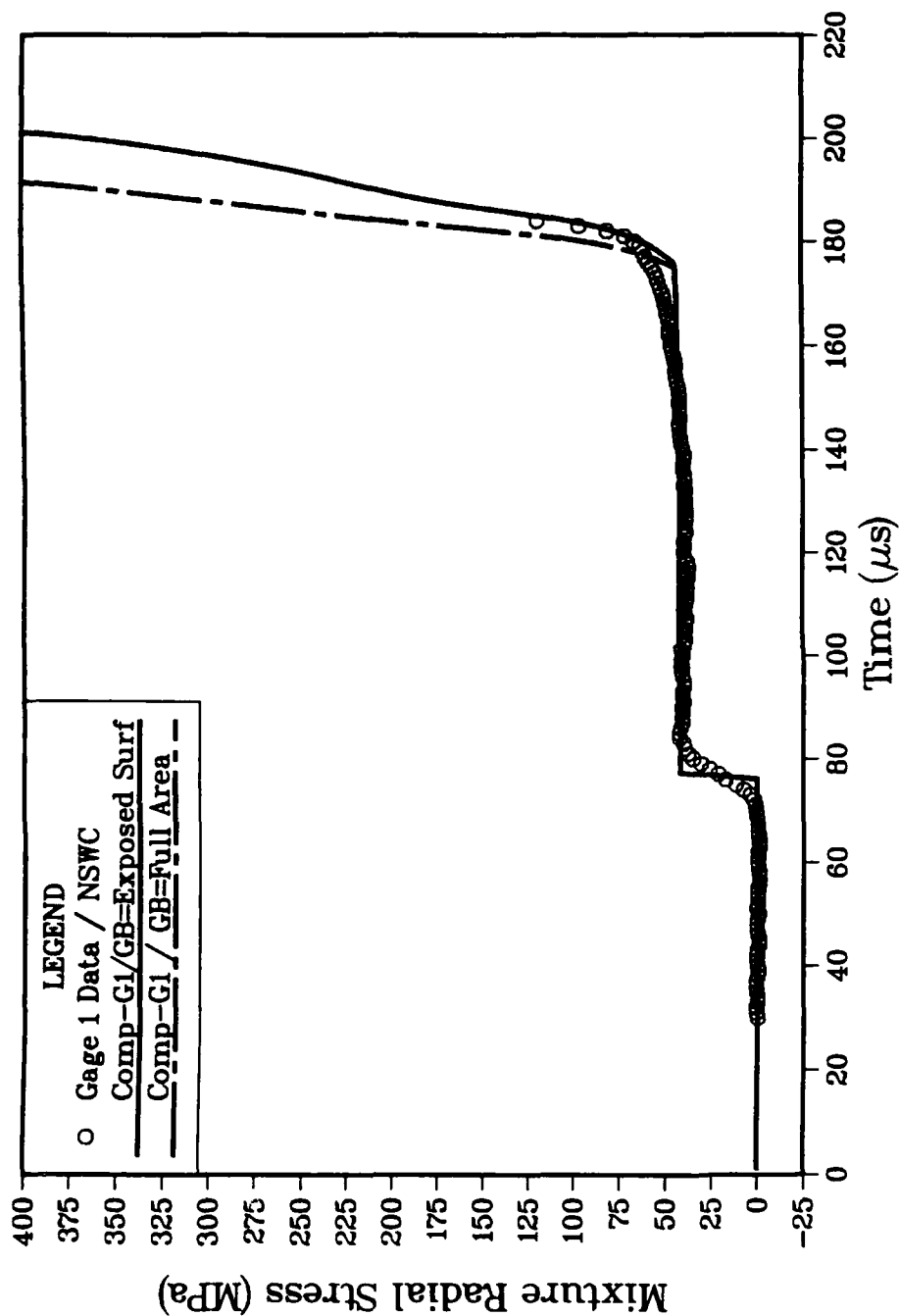
(a) Comparison of model predictions and NSW data [42] from wall-mounted pressure transducers in PDC-80 (gage #1 is located at 38.1 mm, and gage #2 is at 76.2mm). Model computation assumes wave-induced reaction releases 404 cal/g creating initial gas temperature of 1450°K; no further gas-phase reaction. Solid propellant does not ignite.

Figure 31 - Comparison of model predictions and NSW data [15] from PDC-80: 160 m/s impact of Lexan projectile on 60.2% TMD TS-3659 ball propellant.



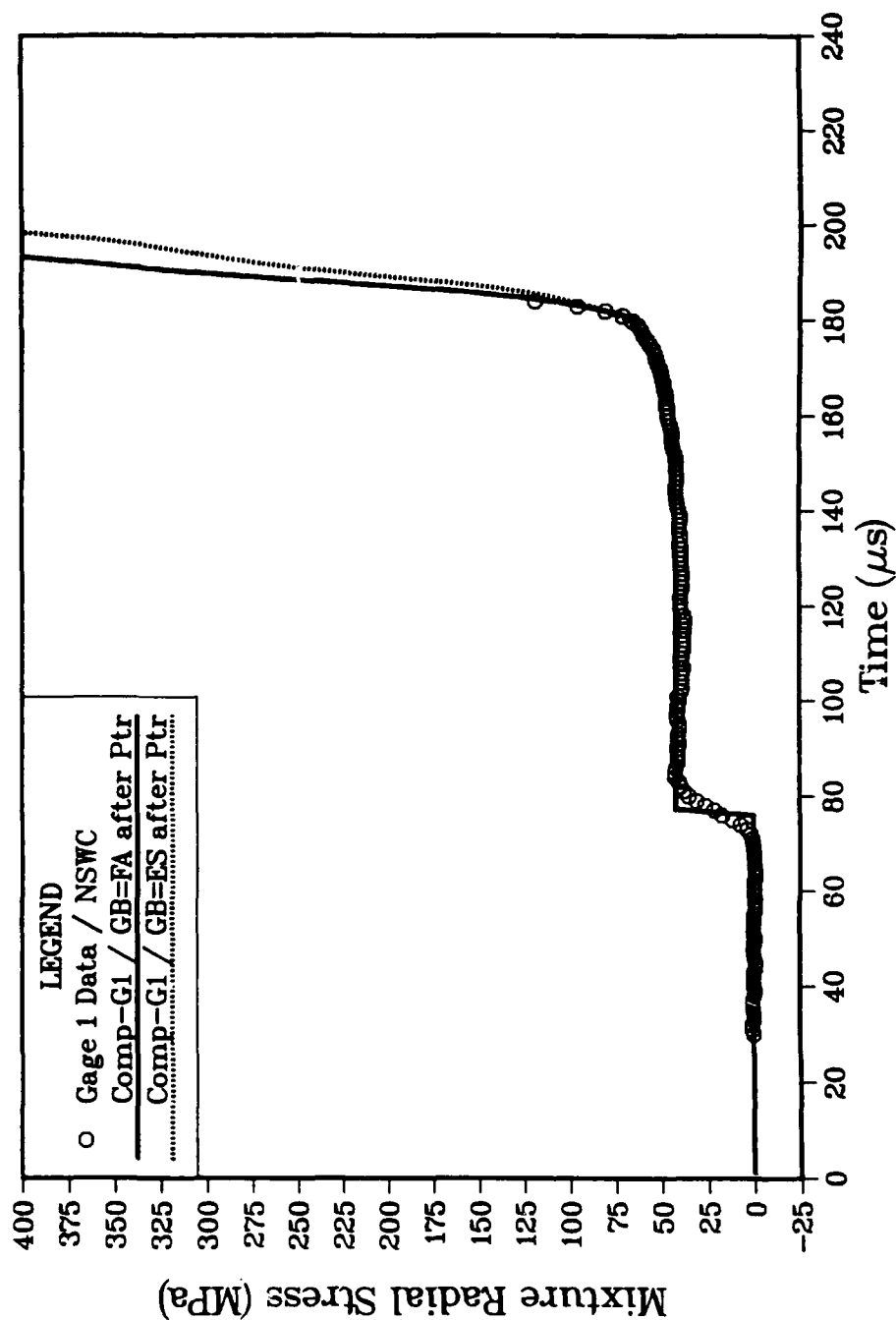
(b) Comparison of assumed paths and NSW data for projectile interface locus from PDC-80. Dashed line results from constant speed = 127 m/s. Solid line is curve-fit to experimental data.

Figure 31 - Comparison of model predictions and NSW data [15] from PDC-80: 160 m/s impact of Lexan projectile on 60.2% TMD TS-3659 ball propellant.



(a) Model computation assumes effective transition pressure, $P_{tr} = 0$. Solid curve based on combustion of exposed surface area of grains in deformed aggregate. Chain-dash curve based on combustion of full surface area of grains.

Figure 32 - Comparison of model predictions and NSWC data [42] from wall-mounted pressure transducer at 38.1 mm (gage #1) for PDC-80: 160 m/s impact of Lexan projectile on 60.2% TMD TS-3659 ball propellant.



(b) Model computation assumes transition pressure, $P_{tr} = 70$ MPa. Solid curve based on combustion of full surface area of grains in deformed aggregate, when $P_g > P_{tr}$. Dashed curve based on combustion of exposed surface area of grains, when $P_g > P_{tr}$.

Figure 32 - Comparison of model predictions and NSWSC data [42] from wall-mounted pressure transducer at 38.1 mm (gauge #1) for PDC-80: 160 m/s impact of Lexan projectile on 60.2% TMD TS-3659 ball propellant.

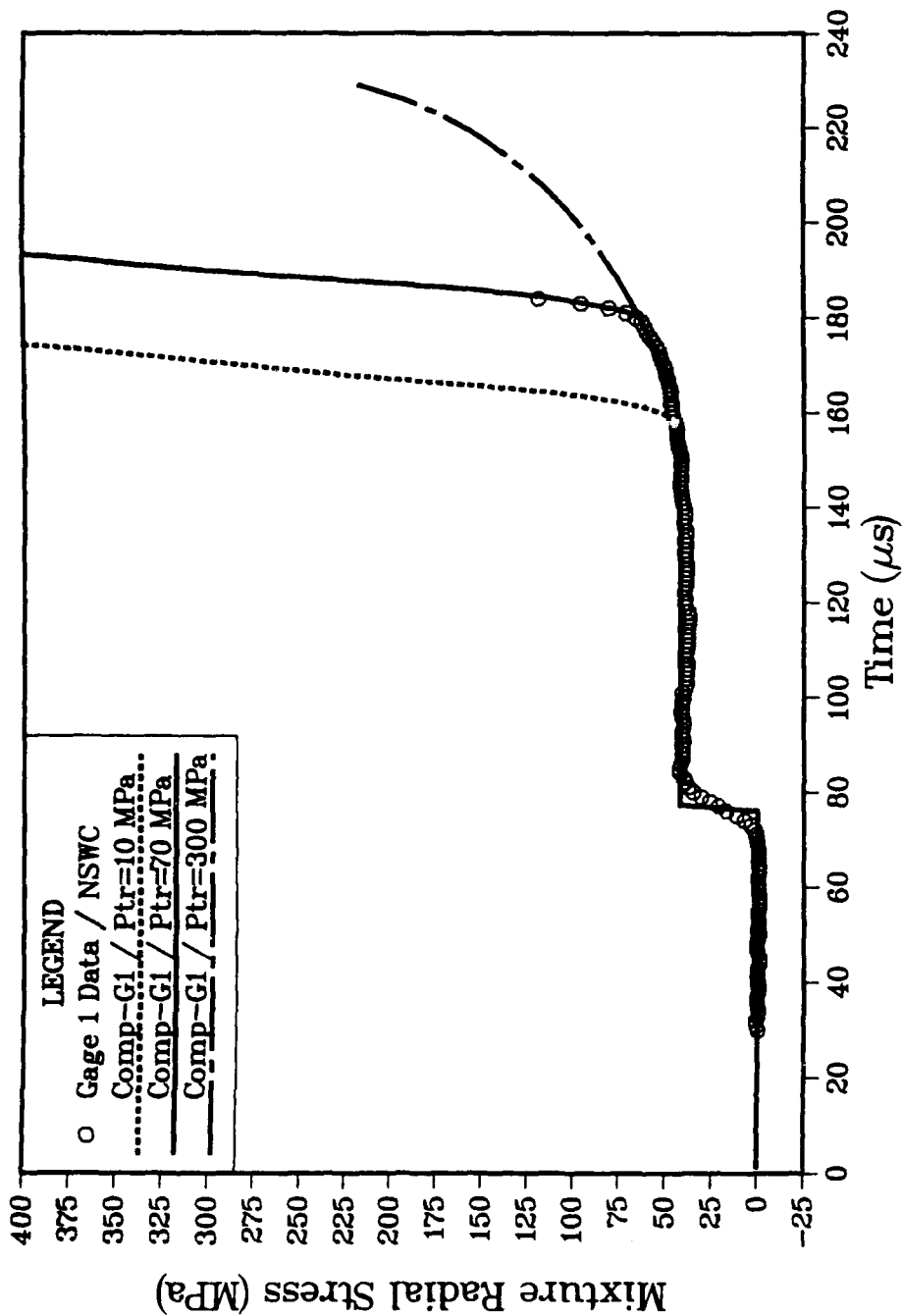


Figure 33 - Influence of transition pressure. Comparison of model predictions and NSWC data [42] from wall-mounted pressure transducer at 38.1 mm (gage #1) for PDC-80: 160 m/s impact of Lexan projectile on 60.2% TMD TS-3659 ball propellant. Model computations assume transition pressure, P_{tr} , is 10 MPa (dashed curved), 70 MPa (solid curve), and 300 MPa (chain-dash curve).

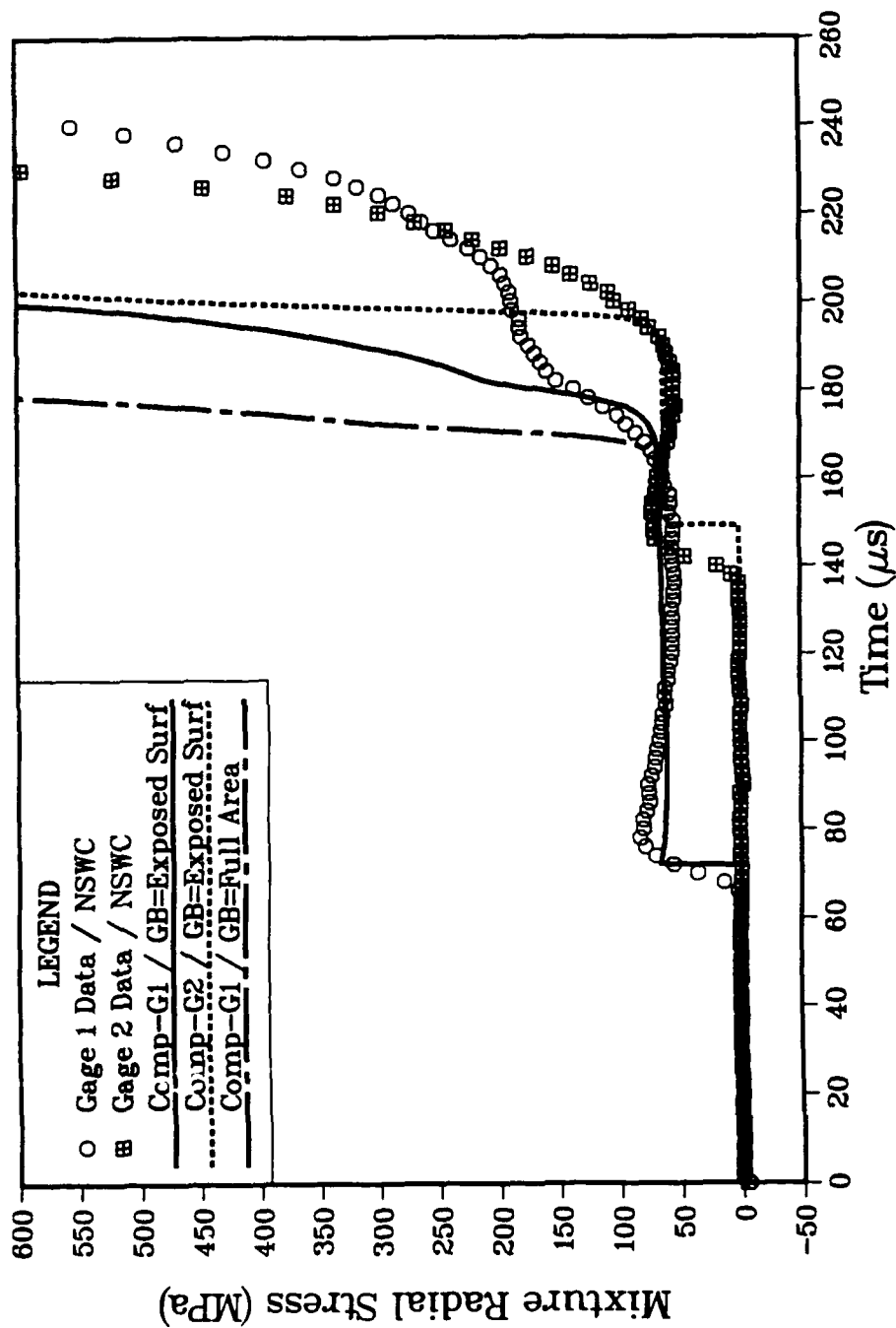


Figure 34 - Comparison of model predictions and NSW data [42] from wall-mounted pressure transducers from PDC-81: 237 m/s impact of Lexan projectile on 60.1% TMD TS-3659 ball propellant. Model computations based on "dual-linear" (192m/s, and 173 m/s) projectile path shown in Fig. 24a. Transition pressure is 70 MPa. Chain-dash curve assumes combustion of full surface area when $P_g > P_{tr}$; other curves assume combustion of exposed surface area when $P_g > P_{tr}$.

range 200 - 300 MPa is a typical consequence of the slower energy deposition rate produced by combustion of only the exposed surface area. This "knee" results from the slight expansion wave caused by the formation of the rapid pressure buildup region into a forward propagating wave system and its movement away from the projectile face.

Changing the energy release mechanism has a substantial influence on the rate of pressure build-up. Setting $P_{tr}=70$ MPa (combustion of exposed surface area of the solid is accompanied by partial energy release while $P_g < P_{tr}$) produces the results shown in Fig. 32b. This prediction for the gage #1 record comes much closer to simulating the gentle lift-off behavior seen by the experiment. There are certainly no claims of uniqueness here, but none of the other schemes attempted by this investigation would reproduce this behavior. The two predictions in Fig. 32b differ only in the amount of surface area involved in the combustion process after $P_g > P_{tr}$; in this example surface area plays a secondary role, but there are too few experimental data points to decide which assumption is better. The dramatic influence of changes in the value of P_{tr} is shown by the results in Fig. 33. The dashed curve is produced by full energy release after ignition, the solid curve ($P_{tr}=70$ MPa) is repeated from Fig. 32b, and the chain-dashed curve assumes partial energy release up to $P_g=300$ MPa (quite unrealistic). A faster gas-phase reaction would tend to steepen the latter curve. If there were ever any doubt, these results show the important role played by the combustion mechanism in the early portion of the transition to detonation. And, of course, the mechanism may change with different materials. Further study will be required in this important area.

The predictions for PDC-80 discussed above assume a constant projectile speed of 127 m/s. Re-computing these cases using a curve-fit (see solid line in Fig. 31b) to the experimental data for projectile path displayed in Fig. 31b results in only minor changes to the predicted gage response. This is not true for the simulation of PDC-81, however. Figure 34 shows a full simulation of PDC-81 using the "dual-linear" projectile locus (Fig. 24a) which matches the given experimental data. The reaction parameters are the same as in PDC-80, except $t_{del}^0=65$ μ s and $\Delta e_{gr}^0=850$ cal/g. The prediction for gage #1 based on combustion of the total surface area of the grains (chain-dashed curve) exhibits a steep rise which is not supported by the experimental data. The other prediction for gage #1 (solid line) assumes combustion of only the exposed surface area, and exhibits a "knee" near 200 MPa similar to the experimental data. The prediction for gage #2 begins runaway similar to the data, but then becomes a strong reactive shock wave much like that seen in PDC-82. The experimental data from both gages, however, show a slower growth rate. The fact that the record from gage #1 actually crosses that from gage #2 suggests that an expansion wave is propagating from the direction of the projectile face. The computation shown in Fig. 34, however, assumes the projectile speed is maintained at 173 m/s. Comparison between experimental data and prediction strongly suggests that an expansion wave of unknown strength was influencing the response at both gage locations. Since the true projectile locus is not known in this case, the computation cannot be used to verify the reaction mechanism. Stated another way, any prediction for PDC-81 which demonstrates a match with the experimental gage records is based as much on an estimated projectile locus as it is on a reaction mechanism. This is not the conclusion this investigation sought, but anything else is a misrepresentation.

VII. SUMMARY COMMENTS AND CONCLUSIONS

(1) The equilibrium stress state (Section II) which is calibrated with data from the quasi-static compaction experiment appears to provide a reasonable description of the compacted granular aggregate. Comparison of model predictions (Section VI) to data from wall-mounted pressure transducers in the PDC experiment strongly suggests that the gages are responding to the radial component of this mixture stress tensor.

(2) The equilibrium shock wave theory (Section IV) predicts that the fundamental properties of a compaction wave (propagation speed, and downstream values of stress, density, and porosity) are functions of the equilibrium stress state. This straightforward computation provides an important base-line to assess the behavior seen in the PDC experiment. When the experimental value of wave speed exceeds this prediction, some mechanism is "driving" the wave.

(A) One possibility is wave-induced reaction which converts a small amount (order of 1 per cent) of solid material into gaseous combustion products. These gases become trapped in the porosity of the compressed aggregate, increasing its "stiffness" to support the higher wave speed.

(1) Available evidence from several materials would suggest that only a portion of the total heat of reaction is liberated in this wave-induced reaction, and hence the gaseous products are intermediate reactants which may be involved in a later gas-phase reaction.

(2) For several materials of interest, the percent of solid participating in the wave-induced reaction appears to decrease with increasing wave strength. This may imply that phase change or other nonlinear physics are participating in the wave-induced reaction.

(B) Another possibility is rate-dependent resistance to dynamic compaction. Modeling this effect (Section III) by assuming that the volume strain rate is linearly proportional to the disturbed force balance cannot explain the observations of the PDC experiment. More complicated constitutive behavior (such as dramatically different resistance forces to compression and expansion) were not investigated.

(C) It is also possible that both (A) and (B) occur simultaneously.

(3) Various laboratory experiments on SDT and DDT in granular energetic material have observed abrupt increases in the speed of propagation of compaction waves and the leading edge of luminosity. The DDT experiment, in at least one case, has evidence of a strong rearward propagating wave. Some insight is provided by a simple quasi-steady model (Section V) which envisions an increase in reactivity triggered by the collision of two reactive compaction/shock waves. Simulation of experimental data shows that:

(A) After a time delay, the onset of vigorous combustion of material adjacent to the piston face will drive a second compressive wave system into the aggregate which has been formed by the initial compaction wave. The leading edge of this second wave system propagates at a speed near the local sound velocity.

(B) The analysis predicts that the abrupt increases in propagation speed observed experimentally would require the collision to induce reaction in the range of 2% - 10%. Transient combustion (neglected in the model) behind the leading edge of the secondary wave system must play a role in the "trigger" mechanism.

(C) The wave pattern produced by the collision includes both a combined compaction/shock wave exhibiting an abrupt increase in speed, and a rearward wave which propagates back into material compressed by the first two waves. A simulated radiograph taken shortly after the collision predicts:

(1) The density behind the combined shock wave may appear nearly equal to the quiescent value. Wave-induced reaction generates enough gas pressure to counteract (resist) the normal occurrence of bed compaction caused by a large value of mixture stress.

(2) A high density ("plug") region is trapped behind the slow-moving contact discontinuity.

(3) The spatial distribution of the high density region will exhibit a "reverse step" as a direct result of the rearward propagating shock wave.

(D) The model suggests that the appearance of a rearward propagating wave may be a direct indicator that a "trigger" mechanism is responsible for the abrupt increase in wave speed. The lack of any rearward propagating wave may signify that the transition mechanism is controlled by nearly complete combustion which "drives" from behind until it catches the leading compaction front, as suggested fifteen years ago by Bernecker & Price [4] on the basis of their DDT experiments.

(4) The transient reactive shock wave model (Section VI) eliminates many restrictive assumptions adopted in the previous models, and accounts for transient combustion in both gas and solid phases. Application to the PDC experiment highlighted three important areas:

(A) Projectile Path. Some uncertainty associated with the experimental projectile face locus after impact was shown to have an important influence on the predicted response of the wall-mounted pressure transducers.

(1) The "linear decay" region in the gage records can be simulated with a slight curvature adjustment to the projectile face locus. Thus, deformation of the Lexan projectile face after impact may have played a larger role than originally thought.

(2) The lack of a precise projectile face boundary condition is a serious impediment to verification of possible reaction mechanisms.

(B) Simulation of the PDC Experiment Based on Inert Material.

(1) Comparison of data from recent PDC experiments with predictions from the equilibrium shock wave theory [34] suggests that granular melamine may have aged and/or absorbed moisture during a ten year storage, and hence recent compaction experiments have seen a "softer" material.

(2) In general, the model can closely simulate the PDC experiment when the model boundary condition is taken from the experimental locus of the (non-deforming) aluminum projectile. However, comparison of predictions for the response of the wall-mounted pressure transducers with the NSWC data suggests that a sliding aggregate composed of small-grain granular material can sometimes lead to anomalous readings from a wall-mounted transducer.

(C) Energy Release Mechanisms. Heat transfer from an inert hot gas trapped in the pores cannot be the sole source of ignition. At least for TS-3659 propellant, there must be some additional source of reaction which leads to ignition of the aggregate.

(1) The model simulations show that a delayed gas-phase reaction which converts the trapped reactive intermediate species into final combustion products could be the source of ignition of the aggregate. However, other reaction sources cannot be ruled out.

(2) Comparison of model predictions with pressure transducer data from the PDC experiments suggests that combustion of the solid begins with an incomplete reaction in the flame zone (as in Fig. 21) and then proceeds to complete combustion (full energy release) as the pressure field rises rapidly. The simulations also suggest that combustion of the exposed surface area of the compacted granular aggregate is controlling the pressure build-up. Further study will be required in this important area.

(5) Unresolved issues:

(A) The wave-induced reaction mechanism was not identified.

(B) Sandusky's [14] observation that " $\tau^2 \Delta t = \text{constant}$ " was not predicted.

(C) The reaction mechanism which controls ignition of the solid aggregate was not determined uniquely or calibrated.

Intentionally Left Blank

REFERENCES

1. Bernecker, R. R., Sandusky, H. W. and Clairmont, Jr., A. R., "Deflagration-to-Detonation Transition Studies of Porous Explosive Charges in Plastic Tubes", Seventh Symposium (International) on Detonation, NSWC MP 82-334, June 1981, pp. 119-138.
2. Bernecker, R. R., "The Deflagration-to-Detonation Transition for High Energy Propellants - A Review", AIAA Journal, Vol. 24, No. 1, 1986, pp. 82-91.
3. Bernecker, R. R. and Price, D., "Studies in the Transition from Deflagration to Detonation in Granular Explosives - I. Experimental Arrangement and Behavior of Explosives Which Fail to Exhibit Detonation", Combustion and Flame, Vol. 22, 1974, pp. 111-117.
4. Bernecker, R. R. and Price, D., "Studies in the Transition from Deflagration to Detonation in Granular Explosives - II. Transitional Characteristics and Mechanisms Observed in 91/9 RDX/Wax", Combustion and Flame, Vol. 22, 1974, pp. 119-129.
5. Bernecker, R. R. and Price, D., "Studies in the Transition from Deflagration to Detonation in Granular Explosives - III. Proposed Mechanisms for Transition and Comparison with Other Proposals in the Literature", Combustion and Flame, Vol. 22, 1974, pp. 161-170.
6. Price, D. and Bernecker, R. R., "DDT Behavior of Porous Columns of Simple Propellant Models and Commercial Propellants", Combustion and Flame, Vol. 42, 1981, pp. 307-319.
7. Bernecker, R. R., Sandusky, H. W. and Clairmont, Jr., A. R., "Deflagration-to-Detonation Transition (DDT) Studies of a Double-Base Propellant", Eighth Symposium (International) on Detonation, NSWC MP 86-194, July 1985, pp. 658-668.
8. Bernecker, R. R., "DDT Studies of a High Energy Spherical Ball Propellant", Ninth Symposium (International) on Detonation, 28 August - 1 September 1989, Portland, Oregon, Preprint Volume III, pp. 899-907. (see also 1987 JANNAF Propulsion Systems Hazards Meeting, CPIA Publication 464, Vol. I, March 1987, pp. 1-11.)
9. Campbell, A. W., "Deflagration-to-Detonation Transition in Granular HMX", 1980 JANNAF Propulsion Systems Hazards Meeting, CPIA Publication 330, 1980, pp. 105-130.
10. McAfee, J. M. and Campbell, A. W., "An Experimental Study of the Deflagration to Detonation Transition in Heavily Confined HMX", 1986 JANNAF Propulsion Systems Hazards Meeting, CPIA Publication 446, Vol. I, March 1986, pp. 163-186.
11. McAfee, J. M., Asay, B. W., Campbell, A. W., and Ramsay, J. B., "Deflagration to Detonation in Granular HMX", Ninth Symposium (International) on Detonation, 28 August - 1 September 1989, Portland, Oregon, Preprint Volume I, pp. 144-154.
12. Sandusky, H. W., "Compressive Ignition and Burning in Porous Beds of Energetic Materials", 1983 JANNAF Propulsion Systems Hazards Meeting, CPIA Publication 381, Vol. I, September 1983, pp. 249-258.

13. Sandusky, H. W. and Liddiard, T. P., Dynamic Compaction of Porous Beds, NSWC TR-83-246, 26 December 1985, Naval Surface Warfare Center/White Oak.
14. Sandusky, H. W. and Bernecker, R. R., "Compressive Reaction in Porous Beds of Energetic Materials", Eighth Symposium (International) on Detonation, NSWC MP 86-194, July 1985, pp. 881-891.
15. Glancy, B. C., Sandusky, H. W., Miller, P. J., and Krall, A. D., "Dynamic Compaction and Compressive Reaction Studies for Single and Double-Base Ball Propellants", Ninth Symposium (International) on Detonation, 28 August - 1 September 1989, Portland, Oregon, Preprint Volume III, pp. 889-898 (see also 1989 JANNAF Propulsion Systems Hazards Meeting, CPIA Publication 509, Vol. I, February 1989, pp. 37-46).
16. Green, L. G., James, E., Lee, E. L., Chambers, E. S., Tarver, C. M., Westmoreland, C., Weston, A. M. and Brown, B., "Delayed Detonation in Propellants From Low Velocity Impact", Seventh Symposium (International) on Detonation, NSWC MP 82-334, June 1981, pp. 256-264.
17. Dick, J. J., "Measurement of the Shock Initiation Sensitivity of Low Density HMX", Combustion and Flame, Vol. 54, 1983, pp. 121-129.
18. Dick, J. J., "Stress-Time Profiles in Low Density HMX", Combustion and Flame, Vol. 69, 1987, pp. 257-262.
19. Baer, M. R. and Nunziato, J. W., "A Two-Phase Mixture Theory for the Deflagration-to-Detonation Transition (DDT) in Reactive Granular Materials", International J. Multiphase Flow, Vol. 12, No. 6, 1986, pp. 861-889. [see also Sandia National Laboratory Reports, SAND82-0293, Dec 1983, and SAND83-1929, Feb 1984.]
20. Baer, M. R. and Nunziato, J. W., "Compressive Combustion of Granular Materials Induced by Low-Velocity Impact", Ninth Symposium (International) on Detonation, 28 August - 1 September 1989, Portland, Oregon, Preprint Volume II, pp. 744-754 (see also 1989 JANNAF Propulsion Systems Hazards Meeting, CPIA Publication 509, Vol. I, February 1989, pp. 95-104).
21. Weston, A. M. and Lee, E. L., "Modeling 1-D Deflagration to Detonation Transition (DDT) in Porous Explosives", Eighth Symposium (International) on Detonation, NSWC MP 86-194, July 1985, pp. 914-925.
22. Aldis, D. F., Lee, E. L., Simpson, R. L. and Weston, A. M., "Model Calculations and Experimental Measurements of the Response of HMX Porous Beds to Deflagration and Shock", Ninth Symposium (International) on Detonation, 28 August - 1 September 1989, Portland, Oregon.
23. Price, C. and Boggs, T. L., "Modeling the Deflagration to Detonation Transition in Porous Beds of Propellant", Eighth Symposium (International) on Detonation, NSWC MP 86-194, July 1985, pp. 934-942.
24. Price, C. F., Atwood, A. I. and Boggs, T. L., "An Improved Model of the Deflagration to Detonation Transition in Porous Beds", Ninth Symposium (International) on Detonation, 28 August - 1 September 1989, Portland, Oregon, Preprint Volume I, pp. 162-168 (see also 1989 JANNAF Propulsion Systems Hazards Meeting, CPIA Publication 509, Vol. I, February 1989, pp. 73-84).

25. Kim, K., "Numerical Simulation of Convective Combustion of Ball Powders in Strong Confinement", AIAA Journal, Vol. 22, No. 6, June 1984, pp. 793-796.
- 26.(a) Hsieh, T. and Kim, K., "Dynamic Compaction and Compressive Reaction Studies for Single and Double-Base Ball Propellants", Ninth Symposium (International) on Detonation, 28 August - 1 September 1989, Portland, Oregon, Preprint Volume III, pp. 877-888. Also (b) 1989 JANNAF Propulsion Systems Hazards Meeting, CPIA Publication 509, Vol. I, February 1989, pp. 85-94.
27. Butler, P. B. and Krier, H., "Analysis of Deflagration to Detonation Transition in High-Energy Propellants", Combustion and Flame, Vol. 63, 1986, pp. 31-48. See also Butler, P. B., Lembeck, M. F. and Krier, H., "Modeling of Shock Development and Transition to Detonation Initiated by Burning in Porous Propellant Beds", Combustion and Flame, Vol. 46, 1982, pp. 75-93.
28. Krier, H. and Kezerle, J. A., "A Separated Two-Phase Flow Analysis to Study Deflagration-to- Detonation Transition (DDT) in Granulated Propellant", Seventh (International) Symposium on Combustion, The Combustion Institute, 1978, pp. 23-33.
29. Akhatov, I. Sh. and Vainshtein, P. B., "Nonstationary Combustion Regimes in Porous Powders", Fizika Goreniya i Vzryva (Combustion, Explosion & Shock Waves), Vol. 19, No. 3, 1983, pp. 297-305 in translation volume.
30. Akhatov, I. Sh. and Vainshtein, P. B., "Transition of Porous Explosive Combustion into Detonation", Fizika Goreniya i Vzryva (Combustion, Explosion & Shock Waves), Vol. 20, No. 1, 1984, pp. 63-69 in translation volume.
31. Ermolaev, B. S., Novozhilov, B. V., Posvyanskii, V. S. and Sulimov, A. A., "Results of Numerical Modeling of the Convective Burning of Particulate Explosive Systems in the Presence of Increasing Pressure", Fizika Goreniya i Vzryva (Combustion, Explosion & Shock Waves), Vol. 21, No. 5, 1985, pp. 505-513 in translation volume.
32. Kooker, D. E., "A Workshop Summary of 'Model Predictions of the Piston-Driven-Compaction Experiment'", BRL-TR-3029, U. S. Army Ballistic Research Laboratory, August 1989 (see also 1989 JANNAF Propulsion Systems Hazards Meeting, CPIA Publication 509, Vol. I, February 1989, pp. 13-36).
33. Kooker, D. E., "A Numerical Study of Compaction Waves in Class D HMX", 1986 JANNAF Propulsion Systems Hazards Meeting, CPIA Publication 446, Vol. I, March 1986, pp. 213-238.
- 34.(a) Kooker, D. E., "A Reactive Shock Wave Model for Compaction Waves in Granular Energetic Material", BRL-TR-2945, U. S. Army Ballistic Research Laboratory, November 1988. Also (b) 1987 JANNAF Propulsion Systems Hazards Meeting, CPIA Publication 464, Vol. I, March 1987, pp. 39-59.
- 35.(a) Kooker, D. E., "Compaction Wave Acceleration in Granular Energetic Material: Simulation With a Reactive Shock Wave Model", Ninth Symposium (International) on Detonation, 28 August - 1 September 1989, Portland, Oregon, Preprint Volume III, pp. 801-811. Also (b) "Collision of Reactive Compaction/Shock Waves in Granular Energetic Material", BRL-TR-2949, U. S. Army Ballistic Research Laboratory, December 1988; and CPIA Publication 477, Vol. I, March 1988, pp. 17-36.

36. Kooker, D. E., "Predictions for the Piston-Driven-Compaction Experiment Based on A Transient Shock Wave Model", 1989 JANNAF Propulsion Systems Hazards Meeting, CPIA Publication 509, Vol. I, February 1989, pp. 47-72.
37. Elban, W. L., "Quasi-Static Compaction Studies for DDT Investigations. Ball Propellants", Propellants, Explosives, Pyrotechnics, Vol. 9, 1984, pp. 119-129.
38. Elban, W. L. and Chiarito, M. A., "Quasi-Static Compaction Study of Coarse HMX Explosive", Powder Technology, Vol. 46, 1986, pp. 181-193.
39. Campbell, R. L., Elban, W. L. and Coyne, P. F. Jr., "Side-Wall Pressure Measurements in Quasi-Static Compaction of Porous Beds of HMX Powders and ABL-2523 Casting Powders", 1988 JANNAF Propulsion Systems Hazards Meeting, CPIA Publication 477, Vol. I, March 1988, pp. 1-16.
40. Kooker, D. E. and Anderson, R. D., "A Mechanism for the Burning Rate of High Density, Porous, Energetic Materials", Seventh Symposium (International) on Detonation, NSWC MP 82-334, pp. 198-215, June 1981.
41. Olinger, B., Roof, B. and Cady, H., "The Linear and Volume Compression of Beta-HMX and RDX to 9 GPa", LA-UR-78-1424, Los Alamos National Laboratory, presented at Symposium (International) on High Dynamic Pressures, Paris, France, 1978.
42. Sandusky, H. W., Glancy, B. C., Campbell, R. L., Krall, A. D., Elban, W. L. and Coyne, P. J. Jr., "Compaction and Compressive Reaction Studies for a Spherical, Double-Base Ball Propellant", 25th JANNAF Combustion Meeting, CPIA Publication 498, Vol. I, October 1988, pp. 83-94.
43. Sandusky, H. W., "Tabulation of Quasi-Static Results from NSWC; Forwarding of", Internal Memorandum / Naval Surface Warfare Center, White Oak Laboratory, 12 June 1989.
44. Carroll, M. M. and Holt, A. C., "Static and Dynamic Pore-Collapse Relations for Ductile Porous Materials", Journal of Applied Physics, Vol. 43, No. 4, 1972, pp. 1627-1636.
45. Freedman, E., "BLAKE: A Thermochemical Program Based on TIGER", U. S. Army Ballistic Research Laboratory, BRL Report ARBRL-TR-02411, July 1982.
46. Jones, D. P. and Krier, H., "Gas Flow Resistance Measurements Through Packed Beds at High Reynolds Numbers", ASME Paper No. 83-FE-8, June 1983.
47. Gough, P. S., "The NOVA Code: A User's Manual", IHCR 80-8, Naval Ordnance Station, Indian Head, MD, 30 December 1980.
48. Baer, M. R., "A Model for Interface Temperatures Induced by Convection Heat Transfer in Porous Materials", SAND88-1073/UC-45, Sandia National Laboratory, Albuquerque, February 1989.
49. Jacobs, S. J. and Sandusky, H. W., "Modeling of Porous Bed Compaction with Deformed Spheres in a Regular Lattice", 1986 JANNAF Propulsion Systems Hazards Meeting, CPIA Publication 446, Vol. I, pp. 149-162, March 1986.

50. Williams, F. A., Combustion Theory, Addison-Wesley, 1965 (see Chapter 4, Section 3d, pp. 84-92).
51. Chang, L. M. and Rocchio, J. J., "Simulator Diagnostics of the Early Phase Ignition Phenomena in a 105-mm Tank Gun Chamber", BRL-TR-2890, U. S. Army Ballistic Research Laboratory, Aberdeen Proving Ground, MD, March 1988 [see also BRL-TR-2838, September 1987].
52. Elban, W. L., Gross, S. B., Kim, K. and Bernecker, R., "Quasi-Static Compaction Studies for DDT Investigations: Inert Materials", Naval Surface Warfare Center, White Oak Laboratory, NSWC TR-81-113, December 1982.
53. Sandusky, H. W. and Glancy, B. C., Naval Surface Warfare Center, White Oak Laboratory, Private Communication of Data for Runs PDC-M34 and PDC-74, Jan - Feb 1990.

Intentionally Left Blank

LIST OF SYMBOLS

- a_g = wave propagation speed in gas phase {see definition above Eq. 24}
 a_{ls} = longitudinal wave speed in solid phase {see definition above Eq. 24}
 a_p = distance between deformed particle centers {see Eq. 14}
 a_{sh} = intercept value in linear Hugoniot representing TMD material {see Eq. 1}
 A_{gr} = pre-exponential factor in gas-phase reaction production term
 {see Eq. 16}
 A_{ls} = modified longitudinal wave speed in solid phase
 {see definition above Eq. 24}
 A_{sh} = slope of linear Hugoniot representing TMD Material {see Eq. 1}
 b = co-volume {see Eq. 10}
 B_2 = coefficient in $\beta_s(\epsilon_s)$, the strength of the granular aggregate {see Eq. 9}
 c_v = specific heat at constant volume
 $C_{\tilde{x}}$ = coefficient used in characteristic theory {defined above Eq. 24}
 $C_{\tilde{y}}$ = coefficient used in characteristic theory {defined above Eq. 24}
 $C_{\tilde{z}}$ = coefficient used in characteristic theory {defined above Eq. 24}
 d_p = particle diameter {used in Eqs. 12 and 13}
 e_g = specific internal energy of the gas phase { /gas volume }
 e_g^0 = reference value of specific internal energy of the gas phase
 { /gas volume }
 Δe_{gr}^0 = relative value {above e_g^0 } of specific internal energy
 of reactive intermediate species, R_1 .
 e_s = specific internal energy of the solid phase { /solid volume }
 E_{gr} = activation temperature in gas-phase production rate term {see Eq. 16}
 $f(R_p/a_p)$ = function defined after Eq. 14
 f_d = interphase drag force per unit total volume [positive when $u_g > u_s$]
 {see Eq. 12}
 f_w = wall friction force per unit total volume
 F_g = term defined after Eq. 25
 F_s = term defined after Eq. 25

$g(R_p/a_p)$ = function defined after Eq. 14

h_g = gas-phase convective heat transfer coefficient {defined in Eq. 13}

H_{ug} = collection of non-homogeneous terms, primarily from the balance of gas-phase momentum {appears only in Eq. 25}

H_{us} = collection of non-homogeneous terms, primarily from the balance of solid-phase momentum {appears only in Eq. 25}

H_{es} = collection of non-homogeneous terms, primarily from the derivative of the equilibrium stress state {appears only in Eq. 25}

H_{os} = collection of non-homogeneous terms, primarily from both energy equations {appears only in Eq. 25}

k_g = gas-phase thermal conductivity

\dot{m} = mass generation rate {due to pyrolysis or combustion of solid} per unit total volume $\{\rho_s \times$ regression rate \times surface area; positive when solid \rightarrow gas}

\dot{m}_{gr} = mass removal rate of gas species R_1 per unit total volume {defined in Eq. 16}

M = molecular weight {see Eq. 11}

n_c = number of contact points in compacted lattice {used in Eq. 14}

p_1 = coefficient in $\beta_s(\epsilon_s)$, the strength of the granular aggregate {see Eq. 9}

p_2 = coefficient in $\beta_s(\epsilon_s)$, the strength of the granular aggregate {see Eq. 9}

$P_g = P_g(\rho_g, e_g)$ = static pressure in gas phase

P_m = mixture pressure {given in Eq. 7}

Pr = Prandtl number in gas-phase

$P_s = P_s(\rho_s, e_s)$ = spherical stress {pressure} in solid phase

P_{tr} = transition pressure: when $P_g < P_{tr}$, combustion of solid produces R_1 ,
when $P_g > P_{tr}$, combustion of solid produces R_2

q = heat transfer rate {from gas to solid} per unit total volume

R = defined in Eq. 2 {related to volume strain}

R_o = universal gas constant {used in Eq. 10}

R_1 = denotes reactive intermediate gas-phase species {see Fig. 6}

R_2 = denotes final gas-phase combustion product species {see Fig. 6}

R_p = radius of deformed particle {see Eq. 14}

R_e, \tilde{R}_e = Reynolds numbers defined in Eq. 12

S_{tv} = exposed surface area of the deformed lattice per unit total volume
{see Eq. 14}

t_{del} = "delay" time before onset of gas-phase reaction {computed in Eq. 15}

T_g = static temperature of the gas-phase mixture

u = "particle" velocity in linear Hugoniot representation {see Eq. 1}

u_g = velocity of the gas phase

u_s = velocity of the solid phase

$U_g = u_g - V_c$ = gas-phase velocity relative to the moving coordinate system

$U_s = u_s - V_c$ = solid-phase velocity relative to the moving coordinate system

V_c = local velocity of the moving coordinate system

V_p = projectile velocity {usually in reference to the NSWC PDC experiment}

V_s = shock wave velocity

$W_g = dz/dt - U_g$ {used in formulation of characteristic equation system}

$W_s = dz/dt - U_s$ {used in formulation of characteristic equation system}

Y_1 = mass fraction of reactive intermediate species, R_1

Y_2 = mass fraction of final combustion product species, R_2

α_g = coefficient used in characteristic theory {defined above Eq. 24}

α_{ls} = coefficient used in characteristic theory {defined above Eq. 24}

α_A = coefficient used in characteristic theory {defined above Eq. 24}

$\beta_s = \beta_s(\epsilon_s) = \sigma_s - P_g$ = strength of compressed aggregate {see Eqs. 8 and 9}

γ = ratio of specific heats {gas phase}

Γ_o = Mie Gruneisen coefficient {assumed constant here}

ϵ_s = solid volume fraction = solid volume / total volume

$\epsilon_g = 1 - \epsilon_s$ = gas porosity = gas volume / total volume

ζ = defined {and used only} in Eq. 9

η = fraction of incoming solid-phase mass flux converted to gas phase
{accounts for wave-induced reaction in reactive shock wave solution}

μ_c = compaction viscosity {see Eq. 10}

$\xi = \xi(\epsilon_s)$ = ratio of σ_r to σ_s {see Eq. 4}

ρ_g = gas-phase density = mass of gas / gas volume

$\hat{\rho}_g = \epsilon_g \rho_g$ = mass of gas / total volume

$\rho_m = \epsilon_s \rho_s + \epsilon_g \rho_g$ = mixture density

ρ_s = solid-phase density = mass of solid / solid volume

$\hat{\rho}_s = \epsilon_s \rho_s$ = mass of solid / total volume

σ_{mr} = radial component of mixture stress {see Eq. 3}

σ_{mx} = axial component of mixture stress {see Eq. 3}

σ_r = radial stress component in solid phase {positive in compression}

σ_s = axial stress component in solid phase {positive in compression}

τ_1 = coefficient in $\beta_s(\epsilon_s)$, the strength of the granular aggregate {see Eq. 9}

$\psi(\epsilon_s)$ = defined in Eq. 6

abbreviations:

DDT = deflagration-to-detonation transition

HMX = cyclotetramethylenetetranitramine

LANL = Los Alamos National Laboratory

NSWC = Naval Surface Warfare Center / White Oak Laboratory

PDC = piston-driven-compaction experiment (NSWC)

SDT = shock-to-detonation transition

SNLA = Sandia National Laboratory / Albuquerque NM

TMD = theoretical maximum density

No of Copies	Organization
1	Office of the Secretary of Defense OUSD(A) Director, Live Fire Testing ATTN: James F. O'Bryon Washington, DC 20301-3110
2	Administrator Defense Technical Info Center ATTN: DTIC-DDA Cameron Station Alexandria, VA 22304-6145
1	HQDA (SARD-TR) WASH DC 20310-0001
1	Commander US Army Materiel Command ATTN: AMCDRA-ST 5001 Eisenhower Avenue Alexandria, VA 22333-0001
1	Commander US Army Laboratory Command ATTN: AMSLC-DL Adelphi, MD 20783-1145
2	Commander US Army, ARDEC ATTN: SMCAR-IMI-I Picatinny Arsenal, NJ 07806-5000
2	Commander US Army, ARDEC ATTN: SMCAR-TDC Picatinny Arsenal, NJ 07806-5000
1	Director Benet Weapons Laboratory US Army, ARDEC ATTN: SMCAR-CCB-TL Watervliet, NY 12189-4050
1	Commander US Army Armament, Munitions and Chemical Command ATTN: SMCAR-ESP-L Rock Island, IL 61299-5000
1	Commander US Army Aviation Systems Command ATTN: AMSAV-DACL 4300 Goodfellow Blvd. St. Louis, MO 63120-1798

No of Copies	Organization
1	Director US Army Aviation Research and Technology Activity ATTN: SAVRT-R (Library) M/S 219-3 Ames Research Center Moffett Field, CA 94035-1000
1	Commander US Army Missile Command ATTN: AMSMI-RD-CS-R (DOC) Redstone Arsenal, AL 35898-5010
1	Commander US Army Tank-Automotive Command ATTN: AMSTA-TSL (Technical Library) Warren, MI 48397-5000
1	Director US Army TRADOC Analysis Command ATTN: ATAA-SL White Sands Missile Range, NM 88002-5502
(Class. only) 1	Commandant US Army Infantry School ATTN: ATSH-CD (Security Mgr.) Fort Benning, GA 31905-5660
(Unclass. only) 1	Commandant US Army Infantry School ATTN: ATSH-CD-CSO-OR Fort Benning, GA 31905-5660
1	Air Force Armament Laboratory ATTN: AFATL/DLODL Eglin AFB, FL 32542-5000
	<u>Aberdeen Proving Ground</u>
2	Dir, USAMSAA ATTN: AMXSY-D AMXSY-MP, H. Cohen
1	Cdr, USATECOM ATTN: AMsTE-TD
3	Cdr, CRDEC, AMCCOM ATTN: SMCCR-RSP-A SMCCR-MU SMCCR-MSI
1	Dir, VLAMO ATTN: AMSLC-VL-D

<u>No. of Copies</u>	<u>Organization</u>
4	<p>Commander US Army Research Office ATTN: R. Ghirardelli D. Mann R. Singleton R. Shaw P.O. Box 12211 Research Triangle Park, NC 27709-2211</p>
2	<p>Commander Armament RD&E Center US Army AMCCOM ATTN: SMCAR-AEE-B, D.S. Downs SMCAR-AEE, J.A. Lannon Picatinny Arsenal, NJ 07806-5000</p>
1	<p>Commander Armament RD&E Center US Army AMCCOM ATTN: SMCAR-AEE-BR, L. Harris Picatinny Arsenal, NJ 07806-5000</p>
2	<p>Commander US Army Missile Command ATTN: AMSMI-RK, D.J. Ifshin W. Wharton Redstone Arsenal, AL 35898</p>
1	<p>Commander US Army Missile Command ATTN: AMSMI-RKA, A.R. Maykut Redstone Arsenal, AL 35898-5249</p>
1	<p>Office of Naval Research Department of the Navy ATTN: R.S. Miller, Code 432 800 N. Quincy Street Arlington, VA 22217</p>
1	<p>Commander Naval Air Systems Command ATTN: J. Ramnarace, AIR-54111C Washington, DC 20360</p>
1	<p>Commander Naval Surface Warfare Center ATTN: J.L. East, Jr., G-23 Dahlgren, VA 22448-5000</p>

<u>No. of Copies</u>	<u>Organization</u>
4	<p>Commander Naval Surface Warfare Center ATTN: R. Bernecker, R-13 B. Glancy, R13 H.W. Sandusky, R13 G.B. Wilmot, R-16 Silver Spring, MD 20903-5000</p>
5	<p>Commander Naval Research Laboratory ATTN: M.C. Lin J. McDonald E. Oran J. Shnur R.J. Doyle, Code 6110 Washington, DC 20375</p>
1	<p>Commanding Officer Naval Underwater Systems Center Weapons Dept. ATTN: R.S. Lazar/Code 36301 Newport, RI 02840</p>
5	<p>Commander Naval Weapons Center ATTN: A. Atwood, Code 3891 T. Boggs, Code 388 E. Lundstrom T. Parr, Code 3895 C. Price, Code 3891 China Lake, CA 93555-6001</p>
1	<p>Superintendent Naval Postgraduate School Dept. of Aeronautics ATTN: D.W. Netzer Monterey, CA 93940</p>
3	<p>AL/LSCF ATTN: R. Corley R. Geisler J. Levine Edwards AFB, CA 93523-5000</p>
1	<p>AL/MKPB ATTN: B. Goshgarian Edwards AFB, CA 93523-5000</p>
1	<p>AFOSR ATTN: J.M. Tishkoff Bolling Air Force Base Washington, DC 20332</p>

<u>No. of Copies</u>	<u>Organization</u>	<u>No. of Copies</u>	<u>Organization</u>
1	OSD/SDIO/UST ATTN: L. Caveny Pentagon Washington, DC 20301-7100	1	Atlantic Research Corp. ATTN: R.H.W. Waesche 7511 Wellington Road Gainesville, VA 22065
1	Commandant USAFAS ATTN: ATSF-TSM-CN Fort Sill, OK 73503-5600	1	AVCO Everett Research Laboratory Division ATTN: D. Stickler 2385 Revere Beach Parkway Everett, MA 02149
1	F.J. Seiler ATTN: S.A. Shackelford USAF Academy, CO 80840-6528	1	Battelle Memorial Institute Tactical Technology Center ATTN: J. Huggins 505 King Avenue Columbus, OH 43201
1	University of Dayton Research Institute ATTN: D. Campbell AL/PAP Edwards AFB, CA 93523	1	Cohen Professional Services ATTN: N.S. Cohen 141 Channing Street Redlands, CA 92373
1	NASA Langley Research Center Langley Station ATTN: G.B. Northam/MS 168 Hampton, VA 23365	1	Exxon Research & Eng. Co. ATTN: A. Dean Route 22E Annandale, NJ 08801
4	National Bureau of Standards ATTN: J. Hastie M. Jacob T. Kashiwagi H. Semerjian US Department of Commerce Washington, DC 20234	1	Ford Aerospace and Communications Corp. DIVAD Division Div. Hq., Irvine ATTN: D. Williams Main Street & Ford Road Newport Beach, CA 92663
1	Aerojet Solid Propulsion Co. ATTN: P. Micheli Sacramento, GA 95813	1	General Applied Science Laboratories, Inc. 77 Raynor Avenue Ronkonkama, NY 11779-6649
1	Applied Combustion Technology, Inc. ATTN: A.M. Varney P.O. Box 17885 Orlando, FL 32860	1	General Electric Armament & Electrical Systems ATTN: M.J. Bulman Lakeside Avenue Burlington, VT 05401
2	Applied Mechanics Reviews The American Society of Mechanical Engineers ATTN: R.E. White A.B. Wenzel 345 E. 47th Street New York, NY 10017	1	General Electric Ordnance Systems ATTN: J. Mandzy 100 Plastics Avenue Pittsfield, MA 01203
1	Atlantic Research Corp. ATTN: M.K. King 5390 Cherokee Avenue Alexandria, VA 22314		

<u>No. of Copies</u>	<u>Organization</u>
2	General Motors Rsch Labs Physics Department ATTN: T. Sloan R. Teets Warren, MI 48090
2	Hercules, Inc. Allegheny Ballistics Lab. ATTN: W.B. Walkup E.A. Yount P.O. Box 210 Rocket Center, WV 26726
1	Honeywell, Inc. Government and Aerospace Products ATTN: D.E. Broden/ MS MN50-2000 600 2nd Street NE Hopkins, MN 55343
1	Honeywell, Inc. ATTN: R.E. Tompkins MN38-3300 10400 Yellow Circle Drive Minnetonka, MN 55343
1	IBM Corporation ATTN: A.C. Tam Research Division 5600 Cottle Road San Jose, CA 95193
1	IIT Research Institute ATTN: R.F. Remaly 10 West 35th Street Chicago, IL 60616
4	Director Lawrence Livermore National Laboratory ATTN: D. Aldis, L282 E. Lee, L282 C. Westbrook A. Weston, L282 P.O. Box 808 Livermore, CA 94550
1	Lockheed Missiles & Space Co. ATTN: George Lo 3251 Hanover Street Dept. 52-35/B204/2 Palo Alto, CA 94304

<u>No. of Copies</u>	<u>Organization</u>
5	Los Alamos National Lab ATTN: B. Asay, J960 J. Dick, P952 J. McAfee, J960 B. Nichols, T7, MS-B284 J. Ramsay, J960 P.O. Box 1663 Los Alamos, NM 87545
1	National Science Foundation ATTN: A.B. Harvey Washington, DC 20550
1	Olin Corporation Smokeless Powder Operations ATTN: V. McDonald P.O. Box 222 St. Marks, FL 32355
1	Paul Gough Associates, Inc. ATTN: P.S. Gough 1048 South Street Portsmouth, NH 03801-5423
2	Princeton Combustion Research Laboratories, Inc. ATTN: M. Summerfield N.A. Messina 475 US Highway One Monmouth Junction, NJ 08852
1	Hughes Aircraft Company ATTN: T.E. Ward 8433 Fallbrook Avenue Canoga Park, CA 91303
1	Rockwell International Corp. Rocketdyne Division ATTN: J.E. Flanagan/HB02 6633 Canoga Avenue Canoga Park, CA 91304
4	Sandia National Laboratories Division 8354 ATTN: R. Cattolica S. Johnston P. Mattern D. Stephenson Livermore, CA 94550
1	Sandia National Laboratory ATTN: M.R. Baer, 1512 P.O. Box 5800 Albuquerque, NM 87185

<u>No. of Copies</u>	<u>Organization</u>	<u>No. of Copies</u>	<u>Organization</u>
1	Science Applications, Inc. ATTN: R.B. Edelman 23146 Cumorah Crest Woodland Hills, CA 91364	1	Veritay Technology, Inc. ATTN: E.B. Fisher 4845 Millersport Highway P.O. Box 305 East Amherst, NY 14051-0305
3	SRI International ATTN: G. Smith D. Crosley D. Golden 333 Ravenswood Avenue Menlo Park, CA 94025	1	Brigham Young University Dept. of Chemical Engineering ATTN: M.W. Beckstead Provo, UT 84601
1	Stevens Institute of Tech. Davidson Laboratory ATTN: R. McAlevy, III Hoboken, NJ 07030	1	California Institute of Tech. Jet Propulsion Laboratory ATTN: L. Strand/MS 512/102 4800 Oak Grove Drive Pasadena, CA 91009
1	Thiokol Corporation Elkton Division ATTN: S.F. Palopoli P.O. Box 241 Elkton, MD 21921	1	California Institute of Technology ATTN: F.E.C. Culick/ MC 301-46 204 Karman Lab. Pasadena, CA 91125
1	Morton Thiokol, Inc. Huntsville Division ATTN: J. Deur Huntsville, AL 35807-7501	1	University of California Los Alamos Scientific Lab. P.O. Box 1663, Mail Stop B216 Los Alamos, NM 87545
3	Thiokol Corporation Wasatch Division ATTN: S.J. Bennett P.O. Box 524 Brigham City, UT 84302	1	University of California, San Diego ATTN: F.A. Williams AMES, B010 La Jolla, CA 92093
1	United Technologies ATTN: A.C. Eckbreth East Hartford, CT 06108	2	University of California, Santa Barbara Quantum Institute ATTN: K. Schofield M. Steinberg Santa Barbara, CA 93106
3	United Technologies Corp. Chemical Systems Division ATTN: R.S. Brown T.D. Myers (2 copies) P.O. Box 49028 San Jose, CA 95151-9028	1	University of Colorado at Boulder Engineering Center ATTN: J. Daily Campus Box 427 Boulder, CO 80309-0427
1	Universal Propulsion Company ATTN: H.J. McSpadden Black Canyon Stage 1 Box 1140 Phoenix, AZ 85029	2	University of Southern California Dept. of Chemistry ATTN: S. Benson C. Wittig Los Angeles, CA 90007

<u>No. of Copies</u>	<u>Organization</u>	<u>No. of Copies</u>	<u>Organization</u>
1	Case Western Reserve Univ. Div. of Aerospace Sciences ATTN: J. Tien Cleveland, OH 44135	3	Pennsylvania State University Applied Research Laboratory ATTN: K.K. Kuo H. Palmer M. Micci University Park, PA 16802
1	Cornell University Department of Chemistry ATTN: T.A. Cool Baker Laboratory Ithaca, NY 14853	1	Pennsylvania State University Dept. of Mechanical Engineering ATTN: V. Yang University Park, PA 16802
1	University of Delaware ATTN: T. Brill Chemistry Department Newark, DE 19711	1	Polytechnic Institute of NY Graduate Center ATTN: S. Lederman Route 110 Farmingdale, NY 11735
1	University of Florida Dept. of Chemistry ATTN: J. Winefordner Gainesville, FL 32611	2	Princeton University Forrestal Campus Library ATTN: K. Brezinsky I. Glassman P.O. Box 710 Princeton, NJ 08540
3	Georgia Institute of Technology School of Aerospace Engineering ATTN: E. Price W.C. Strahle B.T. Zinn Atlanta, GA 30332	1	Purdue University School of Aeronautics and Astronautics ATTN: J.R. Osborn Grissom Hall West Lafayette, IN 47906
1	University of Illinois Dept. of Mech. Eng. ATTN: H. Krier 144MEB, 1206 W. Green St. Urbana, IL 61801	1	Purdue University Department of Chemistry ATTN: E. Grant West Lafayette, IN 47906
1	Johns Hopkins University/APL Chemical Propulsion Information Agency ATTN: T.W. Christian Johns Hopkins Road Laurel, MD 20707	2	Purdue University School of Mechanical Engineering ATTN: N.M. Laurendeau S.N.B. Murthy TSPC Chaffee Hall West Lafayette, IN 47906
1	University of Michigan Gas Dynamics Lab Aerospace Engineering Bldg. ATTN: G.M. Faeth Ann Arbor, MI 48109-2140	1	Rensselaer Polytechnic Inst. Dept. of Chemical Engineering ATTN: A. Fontijn Troy, NY 12181
1	University of Minnesota Dept. of Mechanical Engineering ATTN: E. Fletcher Minneapolis, MN 55455	1	Stanford University Dept. of Mechanical Engineering ATTN: R. Hanson Stanford, CA 94305

<u>No. of Copies</u>	<u>Organization</u>	<u>No. of Copies</u>	<u>Organization</u>
1	University of Texas Dept. of Chemistry ATTN: W. Gardiner Austin, TX 78712		
1	University of Utah Dept. of Chemical Engineering ATTN: G. Flandro Salt Lake City, UT 84112		
1	Virginia Polytechnic Institute and State University ATTN: J.A. Schetz Blacksburg, VA 24061		
1	Freedman Associates ATTN: E. Freedman 2411 Diana Road Baltimore, MD 21209-1525		

INTENTIONALLY LEFT BLANK.

USER EVALUATION SHEET/CHANGE OF ADDRESS

This Laboratory undertakes a continuing effort to improve the quality of the reports it publishes. Your comments/answers to the items/questions below will aid us in our efforts.

1. BRL Report Number BRL-TR-3138 Date of Report AUGUST 1990
2. Date Report Received _____
3. Does this report satisfy a need? (Comment on purpose, related project, or other area of interest for which the report will be used.) _____

4. Specifically, how is the report being used? (Information source, design data, procedure, source of ideas, etc.) _____

5. Has the information in this report led to any quantitative savings as far as man-hours or dollars saved, operating costs avoided, or efficiencies achieved, etc? If so, please elaborate. _____

6. ~~General~~ Comments. What do you think should be changed to improve future reports? (Indicate changes to organization, technical content, format, etc.) _____

CURRENT ADDRESS

Name _____

Organization _____

Address _____

City, State, Zip Code _____

7. If indicating a Change of Address or Address Correction, please provide the New or Correct Address in Block 6 above and the Old or Incorrect address below.

OLD ADDRESS

Name _____

Organization _____

Address _____

City, State, Zip Code _____

(Remove this sheet, fold as indicated, staple or tape closed, and mail.)

-----FOLD HERE-----

DEPARTMENT OF THE ARMY

Director
U.S. Army Ballistic Research Laboratory
ATTN: SLCBR-DD-T
Aberdeen Proving Ground, MD 21007-5066
OFFICIAL BUSINESS

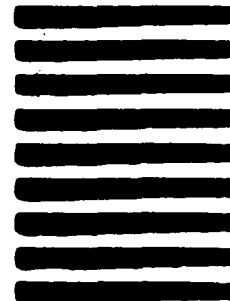


**NO POSTAGE
NECESSARY
IF MAILED
IN THE
UNITED STATES**

BUSINESS REPLY MAIL
FIRST CLASS PERMIT No 0001, APG, MD

POSTAGE WILL BE PAID BY ADDRESSEE

Director
U.S. Army Ballistic Research Laboratory
ATTN: SLCBR-DD-T
Aberdeen Proving Ground, MD 21005-9989



-----FOLD HERE-----